Al-Farabi Kazakh National University

UDC 620.3:543.272.62   On manuscript rights

ZHUMAGALIYEVA ASSEM NURBERGENOVNA

Production and testing of carbonized rice husk-based nanocomposites for capturing of carbon dioxide

6D074000 – Nanomaterials and nanotechnologies

Dissertation submitted in partial fulfillment of the requirements
for the degree of Doctor of Philosophy (Ph.D.)

Scientific Supervisors:
Ph.D.
Doszhanov Yerlan O.;

Ph.D., Researcher,
Institute for Research on Combustion of the University of Naples, Italy Alfe Michela

Republic of Kazakhstan
Almaty, 2023

CONTENTS

NORMATIVE REFERENCES

In the present, the following references for standards have been used:

State Standard 7.1-2003. Bibliographic record. Bibliographic description. General requirements and rules.

State Standard 7.32-2001. Report on scientific – research work. Structure and rules for formulation.

State Standard 1770-74. Laboratory glassware measuring. Cylinders, beakers, flasks, test tubes. General technical conditions.

State Standard 23932-90. Laboratory ware and equipment made of glass.

State Standard 1504-2006. Resource-saving. Waste management. Documentation and regulation of production and consumption waste management

State Standard ISO 14065-2016. Greenhouse gases. Greenhouse gas validation and verification requirements for accreditation or other forms of recognition.

State Standard ISO 17.2.6.02-85. Protection of Nature. Atmosphere. Automatic gas analyzers for monitoring atmospheric pollution. General technical requirements.

State Standard ISO 14067-2019. Greenhouse gases. The carbon footprint of products. Quantification requirements and guidelines.

State Standard 50431-92. Thermocouples. Nominal static conversion characteristic.

State Standard 8.417-2002. State system for ensuring the measurements uniformity. Units of physical quantities.

State Standard 3885-73. Reagents and highly pure substances. Sampling, packing, packaging, and labeling.

NOTATIONS AND ABBREVIATIONS

AC	Activated carbon
AFM	Atomic force microscopy
ATR	Attenuated total reflectance
BET	Brunauer–Emmett–Teller
BJH	Barret-Joyner-Halenda
CB	Carbon black
CB-FM	Carbon black–magnetite composites
CB-NaOH	Carbon black treated by sodium hydroxide
CB-nFM	Carbon black–nanoparticulate composites
CCS	Carbon Capture and Storage/Sequestration
CMNC	Ceramic-matrix nanocomposites
CMS	Carbon molecular sieves
CNT	Carbon nanotubes
cRH	Carbonized rice husk
cRH-FM	Carbonized rice husk –magnetite composites
cRH-NaOH	Carbonized rice husk treated by sodium hydroxide
cRH-nFM	Carbonized rice husk–nanoparticulate composites
cRH-NH$_4$OH	Carbonized rice husk treated by ammonium hydroxide
CVD	Chemical vapor deposition
EA	Elemental analysis
EDAX	Energy dispersive spectroscopy
FM	Magnetite fine particles/Magnetite
FTIR	Fourier transform infrared spectroscopy
GHG	Greenhouses gases
ICP-MS	Inductively coupled plasma–mass spectrometry
IL	Ionic liquid
IPCC	Intergovernmental Panel on Climate Change
IRC-CNR	Institute for Research on Combustion of the National Research Council
IUPAC	International Union of Pure and Applied Chemistry
m$_{ads}$	Mass of adsorbed CO_2
MMNC	Metal-matrix nanocomposites
MOF	Metal-organic frameworks
nFM	Nanoparticulate magnetite
PAC	Physically activated carbon
PNC	Polymer-matrix nanocomposites
PSD	Pore size distribution
RF coil	Radiofrequency coil
RFL	Resorcinol-formaldehyde- lysine
RH	Rice husk
SEM	Scanning electron microscopy

SPIN-CNR	SuPerconducting and other INnovative materials and devices institute of the National Research Council
SSA or SA	Specific surface area or surface area
t_b	Breakthrough time, time of saturation
TG curve	Thermogravimetric curve
TGA	Thermogravimetric analysis
TRL	Technology readiness levels
XRD	X-ray diffraction

INTRODUCTION

General description of the work. The thesis is devoted to production and testing of carbon-based nanocomposites containing iron-oxide nanoparticles for carbon dioxide adsorption in post-combustion flue gas conditions. The experiments were carried out by using the carbon-iron oxide materials derived from the carbonized rice husk (CRH) as support. The influence of leaching on the properties of CRH was also investigated.

This PhD thesis consists of 3 chapters. The first chapter is devoted to the literature survey and describes CO_2 emission and capture, paying particular attention to previous works on composite materials for gas adsorption applications. The second part is devoted to the description of the experiments related to preparation of materials based on carbonaceous matrix-supported magnetic nanoparticles (iron oxides) as well as materials obtained by alkaline treatment of CRH. The physicochemical characterization methods of obtained materials are also included in the second chapter. The third chapter presents the results of the analysis of prepared materials and their adsorption properties evaluated on a laboratory scale static fixed-bed reactor. This chapter is divided into three parts: the first part describes the structural characterization of cRH-FMs, cRH-nFMs composites, the second part describes CO_2 adsorption tests of prepared materials measured at typical post-combustion flue-gas condition (at ambient atmospheric pressure), and the third part reports the comparative analyses of the carbon-based composites.

Actuality of the work. Carbon dioxide (CO_2) emissions are main factors that impact on the global warming. To reduce the greenhouse effect a various gas capture technologies have already been proposed and implemented. Generally, CO_2 capture and sequestration (CCS) can be solved by three major approaches: pre-combustion capture, oxy-fuel combustion and post-combustion capture. Post-combustion on the solid sorbents is one of the advantages of CO_2 capture strategy. Effectiveness of this process primarily driven by economical benefits, because it does not imply significant modifications to currently used combustion technologies. The use of solid sorbents offers remarkable advantages over the other separation methods, since it offers great capacity, selectivity, easy handling and reduced energy for regeneration. The use of solid sorbents towards CO_2 absorption is often studied at high pressure. It was established that materials with a large capacity for CO_2 uptake at high pressure often do not operate well at low pressure. In particular, it was established that CO_2 uptake is influenced primarily by the chemistry of sorbent surface (chemical functional groups) and specific pore metrics at low pressure as in post-combustion conditions (1 bar and 10-15% volume of CO_2).

Materials with a distinctive surface chemistry could find a large application in adsorption technologies. Recent studies of CO_2 adsorption by low-cost hydroxylated metal oxide surfaces strongly encourage the possible use of metal oxides as sorbents. Magnetite (Fe_3O_4) a low cost iron metal oxide, biocompatible and non-toxic for human body was applied in a variety of fields including gas sorption. Magnetite, like other metal oxides exhibits active sites exposed at the surface which can interact with

gaseous molecules. The problem of predisposition to agglomeration process of the particles is solved by using carbonaceous matrix which helps eliminate this disadvantage. In this work CRH was used as carbon matrix or as a support for the preparation of composite materials containing iron oxide particles as active nanomaterials to adsorb CO_2. This material has a great potential for technological applications since it can be converted into different types of fuels and chemicals through a variety of thermochemical conversion processes. The production of sorbent materials starting from RH can mitigate the following environmental impacts: 1) use of agricultural wastes to reduce the disposal issues and 2) the valorization of end-of-life materials as sorbent.

The specific feature of this study is to carry out laboratory experiments in breakthrough microreactor with a fixed bed; the conditions for all experiments are typical for flue gases at room temperature and normal atmospheric pressure.

Purpose and objectives of the work. Production of carbon-based nanostructured composite materials containing iron oxide particles and composites obtained by base-leaching process, study of structural and morphological characteristics of the produced materials and evaluation of adsorption properties (CO_2 capture) in post-combustion flue gas conditions.

It is necessary to solve the following **tasks** in order to achieve the goal:

1. Investigation of carbonized rice husk structure used as carbonaceous matrix in nanocomposites;

2. Synthesis of composite materials based on carbonized rice husk coated with magnetite particles (CRH-FMs), magnetite nanoparticles (CRH-nFM) and carbon black-based composites coated with magnetite nanoparticles (CB-nFM);

3. Evaluation of optimal parameters for alkaline treatment of CRH and study of CO_2 adsorption capacity depending on surface and structural characteristics;

4. Evaluation of CO_2 adsorption properties of fabricated materials by breakthrough experiments on a laboratory-scale fixed-bed micro-reactor under post-combustion flue gas conditions.

The main provisions of the thesis submitted for defense:

1. Carbonized rice husk has high CO_2 uptake up to 11.26 mg/g under post-combustion flue-gas conditions. The sorption capacity of cRH significantly increases to 29.2 mg/g by leaching with an increase in the concentration of the base NH_4OH to 28% in the aqueous solution.

2. Prevention of agglomeration of iron oxide particles in a composite material based on cRH and nanoporous magnetite nFM, in a ratio of 67:33 co-precipitated with TMAOH, effectively increased the sorption capacity to 15.6 mg/g, which exceeds individual indicators of the components by 38% and 13%, respectively. This effect is due to an increase in the volume of microspores up to $3.81*10^{-2}$ cm^3/g and a good synergism between the chemisorption of iron oxide nanoparticles and the physical adsorption of carbon in cRH.

3. cRH treated with NaOH solution increases the carbon content up to 80% and the specific surface area of the material up to 431 m^2/g, which enhance physical sorption and increase the sorption capacity up to 21.9 mg/g.

4. The sorption capacity cRH of the treated NH_4OH increases to 29.2 mg/g due to chemisorption. This effect refines the saturation time of the sorbent up to 25 s with partial removal of silica, which shows an increase in the saturation time of the sorbent up to 25 s with partial removal of silica.

Research object: carbonized rice husk-based nanocomposites contented magnetite particles and nanoporous materials obtained by base-leaching process.

Research subject: investigation of nanocomposite materials structure and physicochemical properties based on carbonized rice husk and study of the influence of material synthesis parameters on the CO_2 adsorption performances.

Methods of research: To reach the established purposes and solve the above mentioned objectives, wet-chemistry approaches have been selected for syntheses of the materials and the following instrumental methods for their structural characterization have been used: elemental analysis (EA), thermogravimetric analysis (TGA), Fourier-transform infrared spectroscopy (FTIR), inductively coupled plasma-mass spectrometry (ICP-MS), Brunauer-Emmett-Teller analysis (BET), scanning electron microscopy (SEM), energy dispersive analysis (EDAX), x-ray diffraction (XRD), atomic force microscopy (AFM). A laboratory-scale fixed-bed micro-reactor was used to estimate materials adsorption capacity.

Scientific novelty of the work lies in the fact that for the first time nanostructured composite materials based on cRH supported with iron oxide were obtained by co-precipitation method investigated in typical post-combustion flue gas conditions for determination of CO_2 adsorption capacity:

1. First ever nanostructured composite materials were synthetized by coating cRH with magnetite particles (cRH-FMs) and magnetite nanoparticles (cRH-nFM) and explored its CO_2 adsorption capacity in typical post-combustion flue-gas conditions;

2. Systematic investigation on the effect of different alkaline treatments for removal of cRH inorganic components was carried out, also CO_2 capture performances were evaluated;

3. The influence content of magnetite particles in carbonized rice husk composites on CO_2 adsorption capacity was established. It was found out that an increase of CO_2 sorption capacity is associated with a certain presence of both micro and mesopores in composites;

4. It was assessed that the CO_2 capture sorption mechanism of the produced composites is intermediate between chemisorption and physisorption interaction.

Theoretical significance

The theoretical significance of the investigation relies upon determination of optimal parameters for the production of alkali treated cRH sorbents and composite materials based on cRH and magnetite with CO_2 capture performances suitable for practical application in post-combustion conditions.

Obtained results were discussed taking into account the influence of the specific surface area, pore size distribution and other structural characteristics affecting CO_2 adsorption by a solid sorbent.

Practical application

The practical significance lies in the fact that the developed composite materials based on carbonized rice husk have the prospect of being used in practical applications as adsorbent for carbon dioxide capture and sequestration technology as low-cost solid sorbents in post-combustion conditions. Moreover, the production of low-cost CO_2 solid sorbents starting from cRH represents an encouraging possibility to face environmental problems related to the disposal of rice husk as it is a very abundant and available agricultural waste.

Approbation of the work. Results of the dissertational work were reported and discussed at the following international and regional scientific and technical venues: XXXIX Meeting of the Italian Section of the Combustion Institute, Naples, Italy, 2016; International Conference on Applied Mechanics, Mechanical and Materials Engineering, Xiamen, China, 2016; Joint IX International Symposium «Physics and Chemistry of Carbon Materials/Nanoengineering» and International Conference «Nanoenergetic Materials and Nanoenergetics», Almaty, Kazakhstan, 2016; International Scientific-Practical Conference "Modern problems of biotechnology: from laboratory research to production", Almaty, Kazakhstan, 2016; III International Farabi Readings, Almaty, Kazakhstan, 2016; V International Student Forum "Green bridge through generations", Almaty, Kazakhstan, 2016; Tenth Mediterranean Combustion Symposium, Napoli, Italy, 2017; X International Symposium "The physics and chemistry of carbon and nanoenergetic materials" Almaty, Kazakhstan, 2018.

Part of the experimental work was carried out at Institute for Research on Combustion and University of Naples Federico II, Naples, Italy under the supervision and support of the foreign scientific consultant.

The Author's personal contribution consisted in: execution of experimental activities devoted to the synthesis and characterization of the materials object of the dissertation work; interpretation and discussion of the results; preparation of articles, thesis and reports. Purposes and objectives, experimental work planning, interpretation of the results and general provisions for the defense were discussed with both scientific consultants.

Publications. The general results of the thesis were published in 12 printed works, one of which is included in the Scopus database (published in Combustion Science and Technology journal with 1.73 impact factor), 1 patent for a utility model, 3 are published in journals recommended by the Committee for Control in Education, Science of the Ministry of Education and Science of the Republic of Kazakhstan and 7 publications in international and regional conferences bulletins.

Scope and structure of the work. The thesis is represented in 106 pages of printed text and contains 62 figures and 26 tables. The work consists of introduction, a review of the literature, description of objects and methods of the research, results and their discussion, conclusion, appendix, a list of used 163 references.

1 LITERATURE REVIEW

Details about the impact of greenhouse gases on the atmosphere will be discussed in this chapter as well as ways to control and reduce carbon dioxide emissions. Information about the use of solid sorbents in post-combustion strategies to mitigate CO_2 emissions in the environment will also be provided. A proper literature review will be performed and information about nanostructured composite materials for gas adsorption, their application and classification will be provided. Particular attention will be paid to magnetic composites and carbon-based composites.

1.1 Global warming and greenhouses gases

Year by year the climate on the Earth considerably changes. Global warming represents the average temperature increase in the Earth's climate system. First of all, these changes are related to greenhouses gases (GHG) emissions, especially carbon dioxide (CO_2) [1]. GHG concentrations have risen with the development of industrialization after second half of the 20th century.

Christophe McGlade and Paul Ekins [2] announce a brief overview of the main assumptions within the four scenarios for the future in 2015. Politicians have entirely established that the average global temperature enhance caused by GHG emissions should not exceed 2 ℃ above the average global temperature of pre-industrial times. The concentration of atmospheric carbon dioxide has multiplied by nearly 40% since the blast-off of the industrial era, while methane and nitrous oxide concentrations have increased by 150% and 20%, respectively [3].

Tian H. et al. [3] noted that a greater influence of GHG emissions is observed also in Southern Asia, a region with about 90% of the global rice fields and more than 60% of the world's nitrogen fertilizer consumption (64%-81% of CH_4 and 36%-52% of N_2O emissions derive from the agriculture and waste sectors). Moreover, in that region, huge contributions to CO_2 emissions derive from Chinese industrial production sectors [3, 4].

In [5] the authors provide a comprehensive probabilistic analysis aimed at quantifying GHG emission budgets for the 2000-2050 periods that would limit warming throughout the twenty-first century to below 2 ℃, based on a combination of published distributions of climate system properties and observational constraints. It has been calculated that to have at least a 50 % chance of keeping warming below 2 ℃ throughout the 21st century, carbon emissions accumulated between 2011 and 2050 must be limited to around 1,100 gigatonnes of CO_2 [5].

Scientists, policymakers and then the general public opinion pay attention to the relationship between CO_2 emissions and climate warming, via the well-known "greenhouse effect". The greenhouse effect is a natural process that warms the Earth's surface. When the Sun's energy reaches the Earth's atmosphere, some of it is reflected back to space and the rest is absorbed and re-radiated by greenhouse gases (Figure 1). The absorbed energy warms the atmosphere and the surface of the Earth. This process maintains the Earth's temperature at around 33°C warmer than it would otherwise be, allowing life on Earth to exist [6]. Human activities such as burning fossil fuels,

agriculture, and land clearing are increasing the number of greenhouse gases released into the atmosphere trapping extra heat and causing of the rising Earth's temperature.
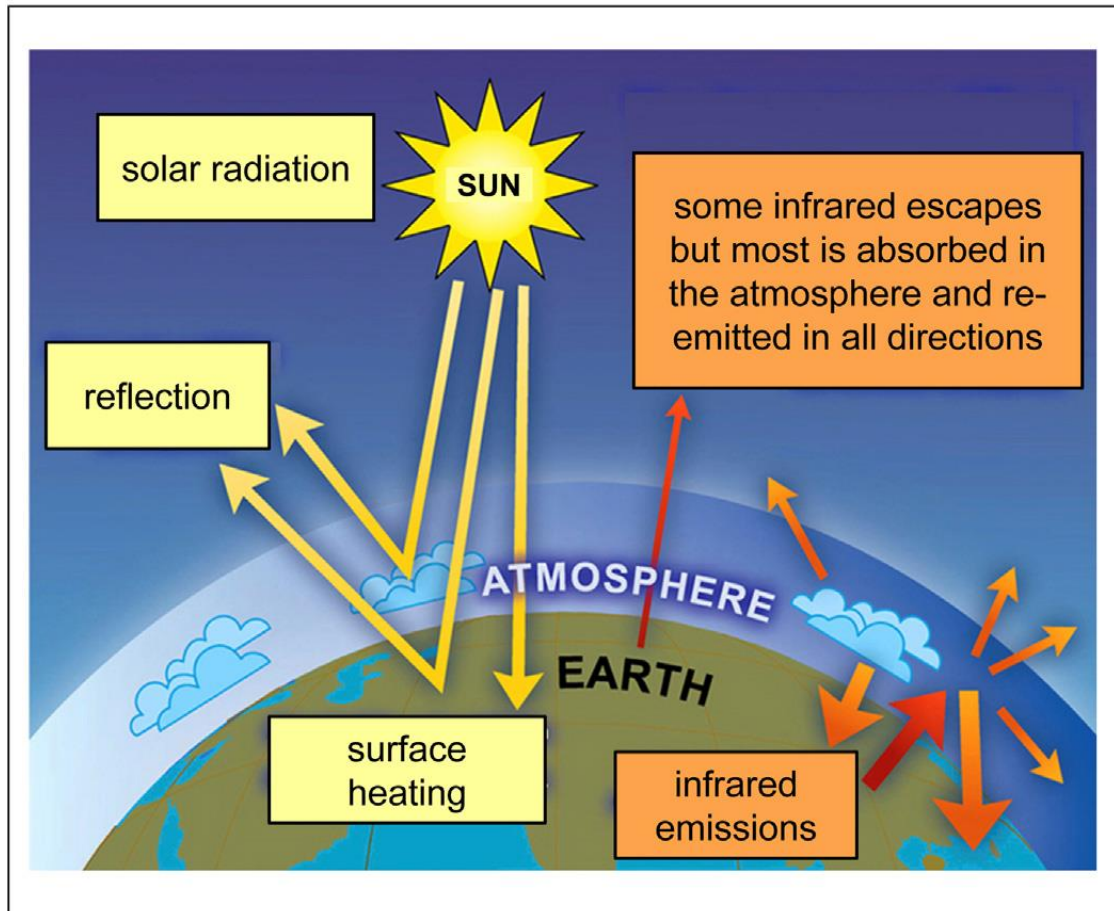
Figure 1 – The "greenhouse effect". The radiative balance between incoming solar radiation (yellow arrows) and the absorption of re-emitted infrared radiation by the atmosphere (orange arrows) drive surface heating. Adapted from [6, 7]

The danger aspect related to uncontrolled CO_2 emissions threatens not only humans but the ecosystems including the oceans [8]. The oceans have a strong impact on the climate system and supply important services to humans. The effect of anthropogenic CO_2 emissions on ocean ecosystems, key marine, and coastal organisms, and services are already detectable. The analysis reported in [8] shows that the prevention of massive and actually,irreversible impacts on ocean ecosystems and their services requires an immediate and significant reduction in CO_2 emissions. Gattuso J.-P et al. in [8] concluded that any new global climate agreement that did not minimize ocean impacts would be incomplete and inadequate.

There are several ways to decrease CO_2 emissions. First of all, the development of alternative energy forms including renewable sources and energy vectors. In conformity with the International Energy Agency (2006, page 66), renewable energy is projected to be the fastest-growing energy source between now and 2030. Second, a deeper understanding of renewable energy consumption is important within the context of the recent literature studying the relationship between technical efficiency and

renewable energy, for example, increasing the share of renewable energy among total energy supply will significantly improve technical efficiency [9]. It is worth noting, although this is a controversial issue. That Mohammad Jaforullah and Alan King from the University of Otago, New Zealand [10] indicate that the increase of nuclear energy consumption could mitigate the GHG emissions in a better way than the increasing use of renewable energy sources.

It is unclear whether CO_2 emissions will continue to increase in 2019 and beyond. However, there is a positive trend of increasing the number of countries where emissions are reduced. Over the past 10 years, 22 countries have experienced an increment in Gross Domestic Product, and CO_2 emissions from fossil fuels and industry significantly decreased. These countries account for 20% of such emissions worldwide [11]. Our country is included in the top 40 CO_2 emitting countries in the world in 1990 and 2012 [12]. Moreover, in Kazakhstan, per-capita energy consumption exceeds 15 tons per person. Therefore, the relevance of studying this topic is clear.

1.2 CO_2 capture technology

The rapid increase of CO_2 concentration in the atmosphere worries scientists long before the global warming alert occurs. U. Siegenthaler and H. Oeshger from Switzerland in 1987 [13] already noted that presumably large quantity of non-fossil CO_2 was released to the atmosphere in the past two centuries, caused by deforestation, extensive methods of land use and decomposition (which results from microbe activity). Alternative near-carbon-neutral energy sources such as ocean tides, waves and currents, hydro energy, wind energy, biomass and geothermal energy, solar and nuclear energy give positive dynamics. But the most CO_2 release is undoubtedly given by the fossil-fuel power plants. In 2005, after the Special Report of Working Group III of the Intergovernmental Panel on Climate Change (IPCC), the global community has begun to take drastic measures to control emissions of CO_2 [14, p. 4]. Since then, widespread Carbon Capture and Storage (CCS) program aimed to prevent the effects of carbon dioxide on our planet.

1.2.1 Carbon capture and storage technology

Carbon capture and storage or carbon control and sequestration (CCS) is a geoengineering proposal based on a collection of CO_2 emission abatement strategies and it embodies a group of multi-step technologies aiming to directly catch CO_2 at the source of emission before it can be released into the atmosphere. The CCS steps basically are: 1) CO_2 separation from other gases contained in industrial emissions (for instance (power plants working on fossil fuels or biomasses); 2) CO_2 compression; i3) CO_2 safe transportation to a location that is isolated from the atmosphere for long-term storage (for instance suitable geologic sites such as deep saline formations) [15, 16].

Currently, three options for capture CO_2 directly at the source are known: post-combustion capture, pre-combustion capture, and combustion of fossil fuels in a pure oxygen environment (oxyfuel combustion) [17]. A detailed diagram of the three options is given below in Figure 2.

Overview of CO$_2$ capture processes and systems
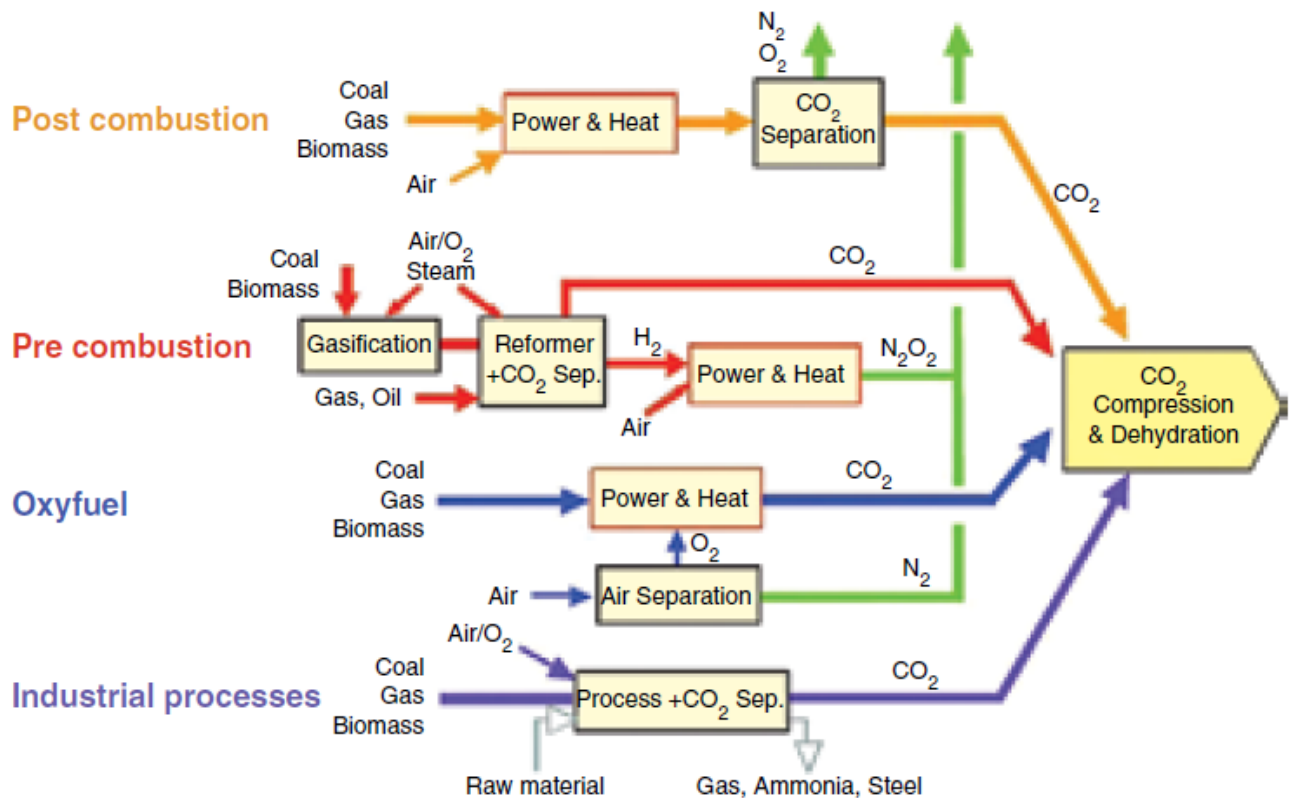
Figure 2 – Outline of different approaches for CO$_2$ capture from industrial sources [17]

1.2.1.1 Post-combustion option

Post-combustion option implies the separation of CO$_2$ from flue gas, typically a mixture of CO$_2$, N$_2$, CO, H$_2$O, NH$_3$, light hydrocarbons, NO$_x$, SO$_x$, and alogen-containing species. This option is particularly suitable for the removal of CO$_2$ from large-scale flue gas flows such as those that arise from coal-fired power plants. Post-combustion capture is advantageous over the other two CCS approaches because its application does not require substantial modifications to the combustion process and the related technologies usually used. This means that a possibility for near-term CO$_2$ capture from new and existing stationary fossil fuel-fired power plants is feasible [18].

Paul A. Webley highlighted that this approach has the advantage of integration with the power plant in which steam from the low-pressure turbine is used for regeneration of the solvent and recovery of the carbon dioxide [19].

Arunkumar Samanta et al. confirmed that capture of CO$_2$ by post-combustion option from flue gas is one of the key technological options to reduce greenhouse gases because it can be potentially integrated into the existing fleet of coal-fired power plants [20].

Up to now, a number of separation technologies useful for post-combustion strategies were proposed: physical absorption, chemical absorption, adsorption, cryogenic separation and membranes [21-24]. These technologies are at different

development progress states, as reported by Bui et al. [25] and summarized in the following Table 1.

Table 1 – Post-combustion options in terms of Technology Readiness Levels (TRL)

Development progress state	Technology
TRL 1 – Basic principles observed	Basic research
TRL 2 – Technology concept formulated	Cryogenic separation
TRL 3 – Experimental proof of concept	Ionic liquids; Inorganic membranes; Supported amines
TRL 4 – Technology validated in the lab (prototype)	Integrating components
TRL 5 – Technology validated in relevant environment (lab scale)	Biphasic solvents; Precipitation solvents;
TRL 6 – Technology demonstrated in a relevant environment (pilot)	Direct air capture; Polymeric membranes; Chemical looping; Calcium carbonate looping
TRL 7 – System prototype demonstration in operational environment	Adsorption on solids
TRL 8 – System complete and qualified	Full-rate production decision
TRL 9 – Actual system is proven in operational environment (commercial)	Amine-based solvents

Solid sorbents applied to adsorption processes of capturing CO_2 from flue gas flows have pointed out a lot of potential benefits in comparison with other conventional CO_2 capture using aqueous amine solvents [20]. Merkel T. C. et al. observed that CO_2 capture through amine absorption is going to be expensive and energy-intensive when applied to flue gas. Gas separation by the membrane is also an attractive option since it can be operated in continuous systems (feeding of mixed gas and exiting of purified gas can happen at the same time) [26].

Post-combustion processes based on CO_2 adsorption on solids or membrane separation are up to now at the earlier stage of development with respect to the well-established absorption on amine, but they have the potential of decreasing the costs associated with CCS [27]. This is true for CO_2 adsorption on solid sorbents due to the remarkable advantages as reduced energy for regeneration, great capacity, selectivity, and ease of handling exhibited by solid sorbents. In particular, even if the chemical absorption with amines is undeniably the most commercially mature capture process, remarkable drawbacks for post-combustion applications arise: high corrosion, thermal and chemical degradations of the amines in the presence of oxygen, high energy penalty associated with the solvent regeneration (25-40% for a coal-fired power station [28], both water and amines can falling on the gas flow thereby causing the outlet of amines emissions (as liquid or gaseous forms) to air and the production of toxic oxidized nitrogen compounds by photo-oxidation [28]. On the contrary, adsorption on

solid sorbents presents some advantages such as low energy requirement and ease of applicability over a relatively wide range of temperatures and pressures [29].

1.2.1.2 Pre-combustion option

Pre-combustion capture approach claims lower costs and higher performances. In this method the fossil fuel is gasified leading to a dry mixture (syngas) consisting principally of $CO + H_2$, then converted to a mixture of $CO_2 + H_2$ by water-gas shift reaction involving CO. After that CO_2 is sent to the compression unit while hydrogen is used as energy vector to a combined cycle to produce electricity [17, 30]. Carbon dioxide can then be set apart using a physical absorbent. This approach is less expensive as an investment and less penalizing for the entire process efficiency compared to the treatment of the exhaust gases, because the produced mixture of gases is under pressure and does not contain nitrogen. Benson S. M. et al. ascertains that gasification process is a settle option to control CO_2 emissions in the chemical and refining manufacturing, anyway the study on gasification connected with power generation is at the early stage [17] of development.

1.2.1.3 Oxy-combustion option

The third method of CO_2 capture is oxy-combustion or oxyfuel combustion. It consists of fossil fuels burning in the pure oxygen environment instead of air. In this way, exhaust gas is a mixture of CO_2 and water without any N_2. Oxy-fuel combustion is characterized by an internal recycle stream induced by the high momentum oxygen jets in place of external recycle. This technology is now spread in the glass industry and still rare in the steel industry. Oxy-combustion can be in principle adopted to any type of fuel utilized for thermal power production. The research interests have mainly been focused on coal and natural gas since these are the most available fuels. For these particular fuels, the technology is typically termed oxy-coal and oxy-natural gas combustion, accordingly. Application of oxy-combustion to biomass or coal derivatives will result in a feasible means of extracting CO_2 from the atmosphere and thereby mitigate the climate changes.

1.2.2 CO_2 adsorption based on solid sorbents

The way to reduce GHG emissions based on the adsorption over solid sorbents is an option under the post-combustion methods. It is well known that solid sorbents can also be used in a temperature swing process, but they have the potential to drastically reduce the energy required to release the CO_2 due to higher CO_2 loading, lower material heat capacity and lower heat of reaction. The use of solid sorbents for CO_2 capture have also cost benefits over solvent-based processes [31]. Overall benefits in the use of solid sorbents for CO_2 capture include as follows: low producing costs, reduced energy for regeneration, great equilibrium adsorption capacity, selectivity, ease of handling, regeneration, multicycle durability, and adsorption/ desorption kinetics [20, 31].

A variety of promising sorbents including activated carbons (AC), microporous/mesoporous silica or zeolites, carbonates, polymeric resins nitrogen-functionalized, metal-organic frameworks (MOF), metal oxides, supported Ionic

Liquids (IL) phases, supported amines carbon-based sorbents, supported carbonates and zeolites, etc. were proposed [20, 22, 31, 32].

An ideal CO_2 adsorbent: 1) should exhibit high selectivity toward CO_2 over N_2 and other exhaust components (CO, NH_3 and light hydrocarbons (i.e. CH_4)); 2) should be produced via inexpensive and low-energy consumption methods and by using renewable resources as precursors; 3) should exhibit flexible morphologies, pore structures and functionalities; and 4) should exhibit good mechanical properties to undergo repeated adsorption-desorption cycles [32, 33].

Sorbent selection is a key point because the materials are required to be both low-cost and versatile in typical post-combustion conditions in order to guarantee an economically advantageous overall process. Materials with distinctive surface chemistry and morphology find large applications and perspectives in post-combustion technology [20].

Solid sorbents are conventionally classified on the basis of interaction types between molecules of CO_2 and the material: physical interaction (physisorption) and chemical interaction (chemisorption). Materials acting as physisorbent are silica gels, zeolites, MOF, porous carbonaceous materials, alumina and etc. Chemisorbents are usually porous surface-modified materials incorporating basic sites (carbonates and amino groups) capable of strong interactions with acidic CO_2. Typical amine-functionalized sorbents are amine-impregnated or grafted silica and amine-functionalized polymers [33-35]. Different ways of introducing functional groups, including methods of grafting and modification of the materials substrate provide the changes in sorbent properties.

Structural features (microtexture, pore metrics, surface chemistry) are relevant in view of the adsorbent selection and optimization since the main parameters for carbon-based adsorbent governing both the CO_2 uptake capacity and selectivity at low CO_2 partial pressure and room temperature are micropore volume and size and chemical functionalization of the pores [33, 36]. Some authors suggested that high CO_2 uptakes correspond to samples with high micropore volumes and pore diameters below 0.8 nm, but as reported in [37] some discrepancies in literature can be found with regard to this point.

1.2.2.1 Chemisorbents for CO_2 capture technology

Modifications in the surface chemistry of the sorbent by incorporating basic sites capable to strongly interact with acidic carbon dioxide giving rising to chemisorption phenomena (chemisorbents) are investigated. In this case, chemisorbents that also have the benefit to retain high selectivity for molecules of CO_2 are considered very perspective.

Functional groups commonly presented on the chemisorbent surface are: alkaline carbonates and amine groups.

The family of regenerable alkali-metal carbonate-based sorbents is one of the most interesting chemisorbents subspecies for carbon dioxide capture technology. Hoffman et al. [37] describe the chemical reactions for CO_2 capture as in the following example:

$$K_2CO_3 + CO_2 + H_2O \Leftrightarrow 2KHCO_3 \qquad (1)$$

$$CaO + CO_2 \Leftrightarrow CaCO_3 \qquad (2)$$

where reactions (1) describe the adsorption of CO_2 and (2) describe sorbent regeneration.

Use of alkali- or alkaline-earth metals carbonates for CO_2 capture was previously reported in the literature [38]. Work by Japanese researchers [37-40] encompassed the potential use of potassium, sodium, and lithium compounds as CO_2 sorbents. Reactions 1 and 2 are also valid for these metal elements. Potassium carbonate was exhibited such a great applicant while using an AC as material support. Previous investigations by the above mentioned researchers explored the use of other materials as a support including alumina and silica gel.

Space Agency investigated potassium carbonate, moreover to other alkali-metal materials, as a regenerative instrument which can adsorb molecules of CO_2 and H_2O. The aim of the study was to develop a mobile system for cleaning inhaled air during an astronaut indwelling in the space. The Japanese together with other countries developing the space station used solid amines as solid sorbents during their staying in space [20, 37]. At present day amino groups are great interested in the processes of sorption of greenhouses gases, including carbon dioxide.

To meet such parameters as durability and requirement for high kinetics, also for improving both, alumina is selected as the ceramic substrate dispersed with the active sodium compound, this fact is reported by [41]. In [41] the authors also identified that dense-phase fluidized-beds and static fixed-beds were not optimum reactor schematics for the pure and dry carbonate operation by the reason of the exothermic nature of the chemical reaction.

After studying regenerable alkali-metal carbonate-based sorbents, Samanta et al. [20] conclude that Na_2CO_3 and K_2CO_3 exhibit the highest CO_2 capture capacities and favorable carbonation and regeneration temperatures (60-200 ºC). Moreover, alkali-metal-based sorbents carry on the additional benefit of being low-cost. These features make them promising sorbents for post-combustion CO_2 capture applications. Though, to be economically profitable, the persistence and long-term stability of exhibited above sorbents in post-combustion facilities under specific real flue-gas conditions have not been yet completely studied. Review of the gas adsorption efficiencies of alkali-metal carbonate-based sorbents (with adsorption (Ads) and regeneration (Reg) temperature) on the basis of previous research findings is reported in Table 2.

The second group of chemisorbents is amine-functionalized solid sorbents. A variety of microporous or mesoporous materials loaded with organic amine functionality have been synthesized and characterized as carbon dioxide capture sorbents. Amine-functionalized solid sorbents include amine-functionalized activated carbonaceous materials, amine-functionalized AC sorbents, impregnated silica-supported sorbents amine-functionalized carbon nanotube sorbents, amine-functionalized solid resin sorbents, functionalized zeolite-based sorbents, functionalized polymer-based sorbents, functionalized silica-supported sorbents,

grafted silica-supported sorbents and impregnated alumina-supported sorbents [20]. In the process of absorption in chemisorbents with amino-groups penetrate throughout chemical reaction.

Table 2 – Data about high performances of alkali carbonate sorbents for CO_2 Capture [20]

Adsorbent (supporting with)	Operational temperatures (°C)	Gas composition	Approximately capacity (mmol/g)	Testing method
K_2CO_3 (activated carbon and coke, silica)	100 (Ads) 150 (Reg)	simulated flue gas and actual flue gas in slip stream	2.1 (Ads. efficiency about 80%)	lab-scale and bench-scale fixed-beds [38]
Na_2CO_3 (ceramic support)	50-70 (Ads) 120 (Reg)	simulated flue gas (14.4% CO_2, 5.4% O_2, 10% H_2O, and 70.2% N_2)	2.3 (>80% efficiency with a 30% active phase)	TGA [42]
Na_2CO_3 (ceramic support)	50-70 (Ads) >135 (Reg in N_2)	10% CO_2, 12.2% H_2O, and 77.8% N_2	2.6 (about 80% efficiency with a 35% active phase)	bubbling bed [43]
K_2CO_3 ("Sorb KX35")	Ads:60-100 Reg:120-220 (in N2)	simulated flue gas: dry basis-12% CO_2 and 88% N_2; 7-30% moisture	2.1 (about 96% efficiency)	coupled fluidized bed reactors: adsorber- fast fluidized bed and regenerator-bubbling fluidized bed, multiple cycles [44]
K_2CO_3 (modified Al_2O_3, support-$KAl(CO_3)(OH)_2$)	70-90 (Ads) 130 (Reg in N_2)	1% CO_2, 9% H_2O, and N_2 balance	2.9 (about 48 wt% K_2CO_3 loading)	TGA and fixed-bed, multiple cycles [45]

Supported amine sorbents can be classified into three classes [20]:

1) Sorbents obtained by method of physical insertion of monomeric or polymeric amine species (into or onto) to the porous substrate as the last material usually use the porous silica by impregnation technique;

2) Sorbents in which the amine (primarily amine-containing silane) is covalently bound to a solid substrate, such as porous silicon oxide. This process occurs due to the connection of amines with oxides using silane chemistry or applying preparation of polymeric substrates with amine supporting side chains. This ensures covalently tethered amine adsorbents with the feasibly entirely renewable through multicycle adsorption/desorption processes;

3) Sorbents which characterized by polymerize "in situ" of amino-polymers on porous supports. This class of supported sorbents may be considered as a hybrid of the other two classes, described above [20].

1.2.2.2 Physisorbents for CO_2 capture technology

In physisorbents CO_2 capture occurs through physical adsorption (physisorption), a process characterized by practically unchanged electronic structure of the atom or molecule upon adsorption in comparison with chemisorption phenomena. The fundamental interacting forces of physisorption are the weak van der Waals forces (~10–100 meV).

The physisorbents can be gathered into two subclasses: micro/mesoporous inorganic and organic adsorbents.

Carbon nanotubes, carbon molecular sieves fall in the organic sorbents subclass while zeolites, MOF, silica gels, aluminas in another one.

Commercial ACs are frequently used for separation of bulk CO_2 from a gas mixture and removal of trace CO_2 from polluted gas [20, 46]. Lee et al. [46] ascertains that selective adsorption of CO_2 over gases like CO, CH_4, N_2, O_2, and H_2 by these materials is caused by van der Waals forces between CO_2 molecule and adsorbent surface as well as by the pole-pole and pole-ion interactions between the permanent quadrupole of the CO_2 molecule and the polar and ionic sites of the adsorbent surface [47]. Varied surface and morphology chemistry of these materials give rise to strikingly different characteristics for physisorption of CO_2 as a pure gas, sometimes as a component of a gas mixture [46].

Ruthven, D.M. in his book "Principle of Adsorption and Adsorption Processes" (1984) describes the CO_2 physisorption, such as adsorption of CO_2 by AC or zeolite with the following mechanism [47]:

$$CO_2 + surface \Leftrightarrow (CO_2) \cdot (surface) \tag{3}$$

Cazarola-Amoros et al. [48] confirmed the positive application of ACs and carbon molecular sieves (CMS) in CO_2 capture by tests at 273 K up to 4 MPa and related adsorption capacities to their porous texture (different origins and pore size distribution). Physisorbents selected in [48] include CMS with a pore size and width between 0.3-0.5 nm, AC with supermicroporosity showed pore distribution 0.7-2 nm, and mesoporous and macroporous of AC. The results obtained show that CO_2 adsorbs at 273 K in the different ranges of porosity following a mechanism similar to process of adsorption N_2 at 77 K. It turned out that CO_2 is more sensitive to a micropore which is not reachable to N_2 at 77 K, and therefore, it is an appropriate probe molecule similar to N_2. The authors indicate such an important trend that carbon dioxide adsorbs in mesopores according to the capillary condensation mechanism.

Wahby et al. [49] prepared CMS from the mesophase pitch utilizing KOH for the activation process. The structural characterization of the produced samples was estimated by N_2 adsorption at 77 K and CO_2 adsorption at 273 K as in [48]. Obtained materials showed an excellent CO_2 adsorption capability; with values of approximately 380 mg adsorbed CO_2 per gram of sorbent at 1 bar and 273 K. These sorbents,

depending on the applicable stage of correspondence and the type of oil residue were characterized primarily by a large surface area up to 3100 m^2/g and, accordingly, determined pore size metrics in the range of 0.35–0.7 nm. In comparison with references such as traditional 13X and 5A zeolites the CO_2 adsorbed in the same condition with these materials is significantly higher [49]. In addition, in [49], these CMS are able to establish CO_2 molecules from typical dimensions molecules, such as methane and nitrogen, selectivity achieved practically 100% for CO_2/CH_4 separation and less effective separation for CO_2/N_2 (about 14%). The presence of large voids together with the availability of a highly developed microporosity, acquired as a result of removal process of the activating agent, attaches these materials to ponderable from point of view adsorption ability, selectivity for the selective adsorption of GHG such as CO_2 from fuel gas and landfill, adsorption/desorption kinetics, and for enhancement natural gas under dry conditions. This CMS also can be used for gas purification processes.

Zeolites are physisorbents with a microporous crystalline framework. Both synthetic and natural zeolites find application in the fields of gas purification, also gas separation. Many zeolites are presented such a silicate frameworks in which several substitution of the silicon/aluminum (or both metals) drives to a negative charge of the framework, with cations within the pore structure - alkaline-earth metals. The cations of metals can be replaced and controlled for changing the pore size or the adsorption characteristics [20]. These materials have unique ion-exchange capabilities, so they can hold various substances on their porous mesh; this feature determines that the interest to zeolites grows each time. Scope of application of zeolites is wide: they can be used for separation, water softening, and removal of gases and solvents, molecular sieving, fuel refining, petrochemical cracking and purification [50]. Table 3 presents CO_2 adsorption capacity of zeolites in different conditions selected by Kelut et al. [51].

Table 3 – CO_2 adsorption properties of selective zeolites. References in [51]

Zeolites	T(K)	Pressure	CO_2 Ads. Capacity(mmol/g)	Year
1	2	3	4	5
NaX/1	298	0.1-0.4 bar	2.8-3.9	2004
NaX/1	323	0.1-0.4 bar	1.43-2.49	2004
LiX/1	303	0.1-0.4 bar	3.1-4.6	2006
NaY/2.4	323	0.1-0.4 bar	0.45-1.17	2007
CsY/2.4	333	0.1-0.4 bar	0.86-1.2	2010
KY/2.4	333	0.1-0.4 bar	0.75-1.6	2010
Silicalite	334	0.1-0.4 bar	0.16-0.45	1996
H-ZSM-5/30	313	0.1-0.4 bar	0.7-1.5	2002
Li-MCM-22/15	333	0.1-0.4 bar	0.68-1	2009
Zeolite 13X	295	100 KPa	4.5	2004
Zeolite 13X	298	1000 KPa	6.52	2004
NaX	298	100 KPa	4.98	2006
NaY	295	100 KPa	4.00	1995

Table continuation 3

1	2	3	4	5
Zeolite 5A	298	100 KPa	4.73	2010
ZSM-5	313	100 KPa	2.59	2004
Chabazite	304	100 KPa	3.27	2012
Chabazite	304	1200 KPa	4.32	2012
H-SSZ-13	298	100 KPa	3.98	2012
Beta	303	100 KPa	1.75	2009
Beta	308	1100 KPa	3.27	2010
T-type	288	100 KPa	4.81	2013
T-type	298	100 KPa	3.94	2013
Zeolite NaKA	273	101 KPa	3.36	2013

The zeolites CO_2 adsorption capacity at ambient temperature was in the range of 2.5 to 3.0 moles/kg. Among zeolites, 13X is the most investigated material for the purpose of CO_2 capture [52]. The carbon dioxide capture properties of acidic zeolites are well-known [53, 54] and good selectivity towards CO_2 over N_2 which is the dominant species in flue gas makes acidic zeolites very promising as a material for carbon dioxide separation.

Zeolites reach equilibrium capacity in a few minutes and from adsorption kinetics of CO_2 point of view they can be called as the fastest adsorbents. The main condition for improved zeolite adsorption and lossless performance is the maximum achievement of feed stream dry flow. This is due to the fact that the low content of silica, although it is a guarantee of high adsorption ability and selectivity at low pressure with favorable isotherms, at the same time makes materials susceptible to moisture which strongly inhibits uptake of CO_2. Indeed, the flue gas needs extensive drying prior to CO_2 capture [55] because of its highly hydrophilic character.

Metal-organic frameworks also known as coordination polymers are crystalline materials that have attracted intense research interest as novel functional materials for the last 20 years.

The MOF structure represents compounding organic linking groups bridged with metal-based centers - single ions or clusters - by to generate one-dimensional (1D), two-dimensional (2D) or three-dimensional (3D) coordination network [56]. MOFs are typically synthesized, often under mild conditions, by a self-assembly reaction between metal ions (nodes) and organic ligands (linkers) [57]. Among thousands of MOF structures reported in the pertinent literature, the majority is built up from divalent cations (Zn^{2+}, Cu^{2+}, Co^{2+}, Ni^{2+}, Cd^{2+}, etc) and typically based on carboxylates, phosphonates or N donating linkers or their combination [57]. This leads to MOFs with a wide range of structure types and pore sizes from the micro to the meso domain and with or without functional groups on the organic spacer. Their large compositional and structural diversity allowing for numerous potential applications such as gas storage, separation of fluids, catalysis, sensing, inclusion, biomedicine, etc. [58]

In particular, the MOF family prepared with use of divalent cations and benzene carboxylate linkers have attracted more attention since they are solids with extra-large pore and high thermal stability [59]. The combined favorable properties of large

surface area, permanent porosity and tunable pore size/functionality have enabled MOFs as ideal candidates for CO_2 capture in post-combustion configuration and for selective removal of CO_2 to upgrade the natural gas [60]. Table 4 shows a variety of MOFs CO_2 uptake capacity in different conditions from the overview in [51].

Table 4 – CO_2 adsorption properties of selective MOFs. References in [52]

Name of MOFs	T (K)	Pressure	CO_2 uptake capacity (mmol/g)	Year
MOF-508	323	0.1-0.4 bar	0.1-0.7	2008
Cu-BTC	298	0.1-0.4 bar	0.5-2	2007
MIL-53	303	0.1-0.4 bar	0.5-1.15	2009
Ni/DOBDC	296	0.1-0.4 bar	2.7-4.01	2008
Co/DOBDC	296	0.1-0.4 bar	2.8-5.36	2008
Mg/DOBDC	296	0.1-0.4 bar	5.36-6.8	2009
ZIF-78	298	0.1-0.4 bar	0.77-1.36	2010
MOF-177	298	100 KPa	1.73	2010
MOF-177	298	1400 KPa	9.02	2010
CD-MOF-2	298	100 KPa	2.68	2011
MOF-74	298	110 KPa	4.86	2005
MOF-177	298	4250 KPa	33.93	2005

1.3   Carbon-based adsorbents and their performance in CO_2 capture

Carbon-based adsorbents are offered as one of the perspective materials for CO_2 capture and storage due to their high surface area, possibility to easy pore structure modification as well as surface functionalization, relative regeneration at low energy consumption and low-cost. Until the present time, some types of carbon materials have been reviewed for this specific use, these are commercial carbon, activated carbons (AC), porous carbon, carbon nanotubes (CNTs), carbon fibers, graphite and graphene-related materials [61].

The production of adsorbents from carbon-rich materials is up-and-coming direction for improving the performance CO_2 capture and storage. Promising carbon-based materials for CO_2 sorption are commercial activated carbons [62]. CO_2 adsorption on activated carbons has been studied experimentally and theoretically for a long time and has found commercial applications.

Plaza M.G. et al. investigated commercial AC as CO_2 adsorbent under post-combustion conditions [63]. Commercial AC presented adequate CO_2/N_2 selectivity and reversible adsorption capacity. Commercial AC also showed excellent cycleability and durability upon several (more than ten) successful adsorption/desorption cycles.

Garcia S. et al. [64] used commercial carbon such as Norit R2030CO2, which has 3.96 mol/kg adsorbent as the maximum value of CO_2 capture capacity (at 25 °C and 3 bar of CO_2 partial pressure, total pressure 15 bar). This adsorbent showed breakthrough time about 10.5 min – time for saturation of surface.

Less favorable adsorption isotherms of AC are the main reason of lower adsorption capacity and selectivity than zeolites exhibited at low CO_2 partial pressure. Absorption of CO_2 at low pressure is the most significant for an adsorption-driven CO_2

capture from flue gas stream at large point power stations due to complexity to arrange the pressurization of flue gas.

Physically activated carbons (PAC) exhibited larger adsorption of CO_2 at a small partial pressure of CO_2. PACs are traditionally prepared by activation in a flow of CO_2 and have significant amounts of ultra micropores (below 0.8 nm). PACs are interesting sorbents because they have high capabilities for adsorption of molecules CO_2, tolerable to water in the flue gas stream and can perform under both equilibrium or kinetic conditions [65].

Performance of some carbon-based adsorbents in CO_2 capture are presented in Table 5 selected by Kelut et al. [51].

Table 5 – Literature data of CO_2 adsorption capacity by Activated Carbon. References in [51]

Carbon material	T (K)	Pressure	Capacity of CO_2 (mmol/g)	Year
AC	298	0.1-0.4 bar	0.6-1.5	2001
AC	328	0.1-0.4 bar	0.25-0.8	2001
SWCNT	308	0.1-0.4 bar	0.5-1.25	2003
MWCNT	333	0.1-0.4 bar	0.34-0.9	2009
Mesoporous carbon	298	100 KPa	1.5	2010
Mesoporous carbon	298	1000 KPa	3.0	2011
AC	298	100 KPa	2.27	2010
AC	298	3000 KPa	21.29	2010
Microporous carbon	298	100 KPa	4.0	2012
PAC (grass utility)	273	10 KPa	1.45	2013
PAC (horse manure)	273	10 KPa	1.36	2013
PAC (beer waste)	273	10 KPa	1.31	2013

1.4 Nanocomposite materials

Nanotechnology is rapidly taking a leading position as a research field in the global scientific community. Widespread nanomaterials are already used in many different fields: electronic devices, optoelectronic devices, bio-sensors, photodetectors, aerospace devices, solar cells, nanodevices, plasmonic structures, etc. Nanomaterials are often combined in nanocomposites. Nanocomposite materials are composites in which at least one of the side exhibits dimensions in the nanometer range ($1 \text{ nm} = 10^{-9} \text{ m}$). In other words: nanoparticles are disseminated in a matrix [66-70]. First studies about them were presented about 70 years ago, reaching high-quality development and mass production from the early 1990s [71]. Balwinder Singh et al. cited the words of O. Kamigaito in the article "What can be improved by nanometer composites?" [72] where they presented some relations between the size of nanocomposite particles and the manifestation of properties: for catalytic purposes the values of the particle size may be approximately 2-5 nm, for making soft magnetic materials and to get the properties changes, the particle size should be around 20nm, near 50 nm for refractive index change, about 100 nm for mechanical properties and superparamagnetism [73].

Nanocomposites can be described as a whole matrix structure, with periodic inclusions or phases – following Gleiter's classification on the structure of nanocomposite materials. Most often, nanocomposites are a combination of an inorganic solid (called the host) and an organic component, although a reverse version is possible. There are also materials consisting more than two components, the main thing is that one of the phases has a nanometric size. These examples of nanocomposites include gels, porous media, colloids, and copolymers. Nanostructured phases present in nanocomposites can be zero-dimensional – embedded clusters, 1D – nanotubes, 2D – nanoscale coatings, and 3D – embedded networks. Thereby, nanocomposite materials can demonstrate different mechanical, catalytic, electrical, optical, electrochemical, and structural properties than those of each original component. It is also well known that any specific property of the obtained material is often more than the sum of individual components of the nanocomposite [71]. Some classes of nanocomposite materials will be reported more deeply in the following subparagraphs focusing the attention on their application in gas adsorption.

1.4.1 Classification of nanocomposite materials

The classification of nanocomposite materials is ambiguous and depends on the characteristic by which they are classified.

Camarata et al. in [74] distinguish three types of nanocomposite materials classified microstructurally. First type - nanolayered composites, materials containing layers of nanosize dimensions, second type - nanofibrous nanocomposites, namely materials made by a matrix with embedded nanofilaments, third type is nanoparticulate composites, a matrix with nanoparticles.

C. Okpala et al. in [75] classified nanocomposites by dimension and isolated 0D and 1D materials (chains, $(Mo_3Se_3-)n$ and clusters), two-dimensional layered (clay materials, metal oxides, metal phosphates, chalcogenides) and 3D framework systems, for example, zeolites. New improved properties of almost all types of nanocomposites compared with macrocomposite analogues have been experimentally proven. So future of nanocomposites application is promising in many fields such as battery cathodes and ionics, sensors, mechanically-reinforced lightweight components, non-linear optics, nanowires and other systems.

In Figure 3 simplified classification of nanocomposite materials by structure is presented. In [76] nanocomposites are divided into three categories: matrix nanocomposites, intercalated and membranous nanocomposites.

S. Kumar et al. classified all nanocomposite materials by reinforcement and divided them into: polymer nanocomposites/polymer-matrix nanocomposites (PNC), ceramic-matrix nanocomposites (CMNC) and metal-matrix nanocomposites (MMNC) [77]. PNC is a material where a polymer contains dispersed nanoparticles in it. PNCs represent a new class of materials alternative to the traditionally filled polymers. Specific properties of the material are reached by nanosized inorganic filler dispersed in an organic matrix [78].
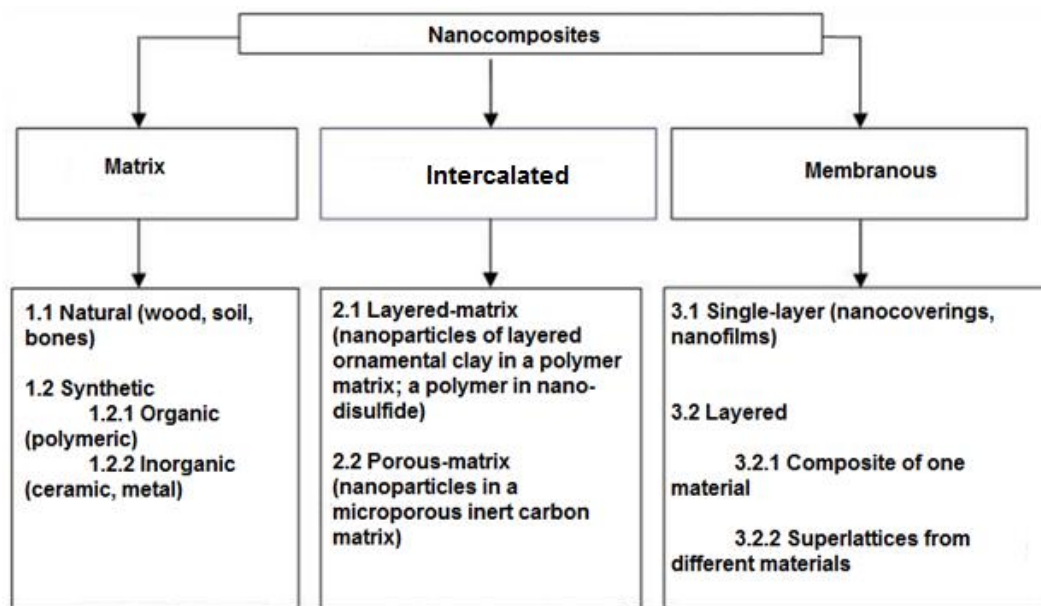
Figure 3 – Simplified classification of nanocomp. materials by structure [76]

Ganguly et al. underlined their advantages like lightweight, flexible, corrosion-resistant and cost-effective and they offer easy fabrication. Moreover, PNCs have an unprecedented combination of dielectric, magnetic, electrical, thermal and physicomechanical properties which make them suitable for the reduction of the electromagnetic noises [79]. Silicon nanospheres are an example of PNC. They show peculiar characteristics: when their size is 40–100 nm they are much harder than silicon, in particular their hardness results between sapphire and diamond. Frequently nanoparticles included in PNCs are carbon nanotubes, montmorillonite organoclays, polyhedral oligomeric silsesquioxane, carbon nanofibers, nanosilica, nanoaluminum oxide, molybdenum disulfide and tungsten disulfide, nanotitanium oxide and so on [77, 80, 81]. PNC for biomedical applications potentially have a huge future, such as bone implants, actuators, tissue engineering, drug delivery, cellular therapies, sensors, stem cell engineering, regenerative medicine, etc. [82, 83].

CMNCs are described by the authors in [78] as a ceramic matrix with reinforcing nanoparticles as carbon, glasses, glass-ceramics, oxides or non-oxides. This aspect gives the possibility to change the properties of the resulting CMNC: electrical conductivity, thermal conductivity, thermal expansion and hardness.

Zhang et al [84] reported on the methods to obtain CMNCs: thermal evaporation, laser ablation, ion beam deposition, ion implantation, magnetron sputtering and chemical vapor deposition (CVD). CVD is the more suitable method because it allows high deposition rate and uniform depositions for complicated geometries. Birkholz et al. [85] used gas flow sputtering to prepare CMNC reinforced with Al_2O_3/TiO_2 in combination with Cu/W; these new materials show high resistance to corrosion, high mechanical hardness and small coefficients of friction.

A.R. Boccaccini et al. [86] reported about the combination of CNTs and ceramic system (nanocrystalline particles) leading to functional heterostructures for applications in field emission displays, electrochemical supercapacitors,

nanoelectronic devices, photocatalytic devices, gas sensors, drug delivery systems, antibacterial films, biomedical scaffolds, biosensors and so on.

Overall, the main disadvantage of CMNCs is their synthesis: it is complicated and costly, it requires high temperature and brittle in nature [77].

MMNCs consist of a metal matrix filled with nanoparticles. Metals like Al, Mg and Cu, have been applied for the making MMNCs as well as nanoceramic particles such as carbides, nitrides, oxides or carbon nanotubes [87]. MMNCs such as Mg/CNT, Fe-Cr/Al_2O_3, Ni/Al_2O_3, Fe/MgO and Al/CNT are investigated. Filament reinforcements comprise SiC/magnesium, carbon graphite/copper, graphite/aluminum, and SiC/aluminum.

Production methods can be briefly categorized into two groups: the first "ex situ" synthesis route consists of adding nano-reinforcements to the liquid or powdered metal, while "in situ" processes refer to those methods leading to generation of ceramic nano-compounds by reaction during processing, for example, by using reactive gases. Several methods have been developed for "ex situ" synthesis of MMNCs. Different powder metallurgy techniques were successfully employed. MMNCs ensure excellent wear resistance in dry sliding wear, especially intermetallic compounds like $NiAl_3$ and NiAl [77, 87].

1.4.2 Carbon-based nanocomposites for gas adsorption

Carbon-based materials are widely used for gas sorption, including carbon-based nanocomposites. Xiang et al. described a nanocomposite material for CCS based on MOF with incorporated CNTs and lithium ions [88]. The authors proposed a composite, in which the CNTs bearing carboxylic groups provide homogeneous nucleation sites to support a continuous copper framework growth ($Cu_3(btc)_2$), and the Li^+ ions were subsequently introduced into the frameworks by simple doping. This nanocomposite indicated as Li@CNT@[$Cu_3(btc)_2$ shows CO_2 uptakes per effective surface area that are increased approximately by 3 times compared to the unmodified MOF [88]. Alhwaige et al. in [89] used chitosan-polybenzoxazine as a precursor for high CO_2 adsorbing carbon aerogels. Carbon aerogels are mesoporous materials with pore size in the range of 2-7 nm, and high BET surface area. Carbon aerogels produced by Alhwaige et al. in [89] were characterized by a BET surface area of 710 m^2/g and a total pore volume of 0.296 cm^3/g. Breakthrough curves of CO_2 adsorption show high adsorption capacity at ambient conditions and excellent CO_2 adsorption-desorption reversible performance with maximum 5.72 mmolg^{-1}. This excellent characteristic of carbon aerogels synthesized from clay-reinforced biobased chitosan-polybenzoxazine nanocomposites opens the possibility for the rapid and large-scale industrial preparation of novel biobased porous carbons with high adsorption capacities for CO_2 capture at various operating temperatures and multicyclic adsorption-desorption stability.

Chowdhury et al. in [90] synthesized a series of mesoporous titanium dioxide/graphene oxide (TiO_2/GO) nanocomposites using a simple colloidal blending process and they systematically investigated such materials as potential CO_2 adsorbent materials. TiO_2/GO exhibited CO_2 adsorption capacity about 1.88 mmol g^{-1} at ambient

conditions. Moreover, TiO_2/GO nanocomposites demonstrated a low heat of adsorption and excellent high CO_2/N_2 selectivity and hence merits further consideration for capturing CO_2 from dry flue gas.

H. An et al. in [91] fabricated AC fiber-phenolic resin composites and they investigated the linear relationship between material textural properties and CO_2 adsorption capacity (Figure 4). Carbon fibres mixed with powdered phenolic resin in water at a determined mass ratio after vacuum pumped prepared suspension is dried and pressed. Subsequently, the samples were carbonized at 650 °C in nitrogen stream. Activation procedure occurs at range of temperature of 800-920 °C. The resulting sorbents present as a 3.2 cm dia. and 10cm long cylinder approximately. This work demonstrated that ACs derived from powdered phenolic resin have the capability to capture CO_2 with a maximum sorption capacity of 2.9 mmol/g. The research concluded that at lower relative pressures, samples obtained at lower burn-off are able to capture larger amount of CO_2 than those with higher activation degrees. It was rated that the micropore volume contributed mostly in the CO_2 uptake at low relative pressures. According to Figure 4a, adsorption capacity at 25 °C is increased in direct proportion to the increasing in volume of CO_2 with the exception of three marked points which are not taken into account on the linear regression. The optimal pore size of CO_2 adsorbents at this temperature lies in the range of 1.45-1.55 nm. The authors conclude that sorption capacity of the modified AC under post-combustion conditions can be achieved by receiving narrow microporosity with enhance volume of micropore coming from able micropores in material. The linear relationship between burn-off and increasing sorption capacity is not established. In this work it was noticed that lower burn-off sorbents have higher adsorption capacity of CO_2 at ambient conditions.
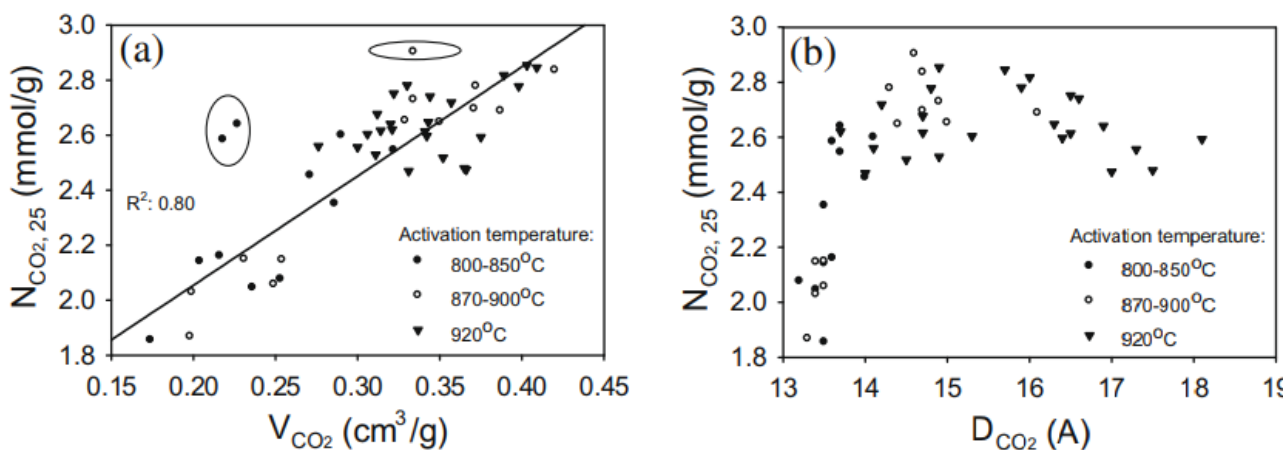

Figure 4 – The relations between adsorption capacity of AC fiber-penolic resin composite at 25 °C and micropore volume (a) and micropore size (b). Adapted from [91]

Bhagiyalakshmi et al. in [92] designed Polythiophene–mesoporous carbon composite materials for CO_2 adsorption tests. The material exhibits pore diameter in

the range of 3.35-5.84 nm, and showed 120 mg/g as maximum adsorption capacity at ambient conditions that assumes possible use of such materials in energy application.

Wang et al. found out that modification of carbon framework with impregnation of additives such as 3-chloropropylamine-hydrochloride and polyethylene glycol, or by incorporation of basic nitrogen groups increases the efficiency of the carbon-based sorbents in CO_2 adsorption [93].

V. Gargiulo et al. in [94] synthesized Ionic liquid (IL) supported on a nanostructured commercial carbon black (CB) and they used such material as CO_2 sorbent under dynamic conditions. IL is a salt that consists of ions and short-lived ion pairs, and it has a melting points lower than 100 ºC [61]. Peculiar properties of IL are: high solvent capacity, high thermal stability, tunable properties and negligible vapor pressure [95]. The first discovery of adsorption properties of IL was performed by Blanchard et al. [96] who observed the fact that a major amount of CO_2 can be dissolved in imidazolium-based ILs.

Sorbents based on CB modified by IL, as expected, make it possible to obtain materials with high CO_2 sorption capacity: 27.3 $mgCO_2$/g. But IL-based materials have some disadvantages such as high viscosity, mass transfer limitations and higher cost [61, 94].

Recently, Hao et al. in [97] synthesized a new nitrogen-doped porous carbon monolith obtained from the pyrolysis of the copolymer obtained by resorcinol-formaldehyde-lysine (RFL). They determined CO_2 adsorption capacity from carbon dioxide -sorption isotherms (Figure 5) of RFL carbonized at different temperatures (400 °C, 500 °C, 600 °C, 700 °C, 800 °C).

The maximum CO_2 sorption capacity was determined for RFL-500 (3.13 mmol/g at room temperature and 1 atm).
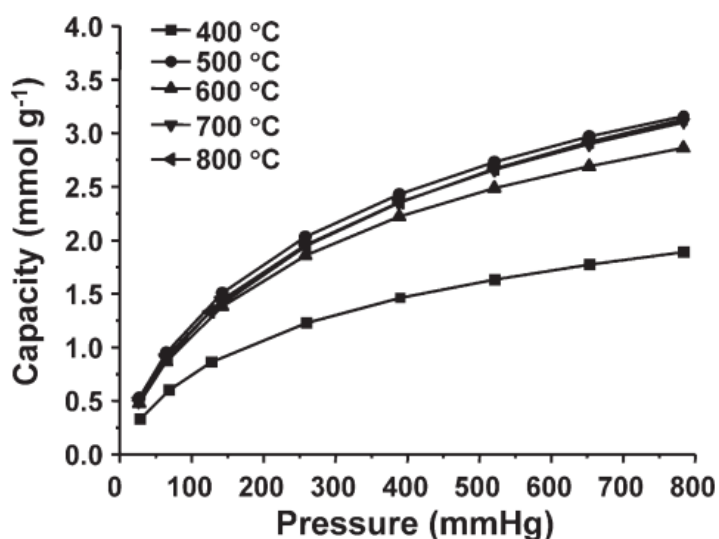

Figure 5 – CO_2 adsorption isotherms of nitrogen-doped porous carbon monolith RFL synthesized by Huo et al [97]

Graphite and graphene-related materials (graphene, graphite oxide, graphene oxide), which are synthetic carbon allotropies, have been also investigated as CO_2 sorbent. Reasons for their application in CO_2 capture applications are basically: high specific surface area and low production cost.

To enhance the sorption ability their surface can be also modified with oxide as iron oxides or silica, or metals as palladium, etc. Some results on modified graphite and graphene modifications for CO_2 sorption applications are shown in table 6.

Table 6 – CO_2 capture performance of some graphite/graphene-based adsorbents. Adapted from [61]

Schemes	Materials	CO_2 Ads capacity, conditions of the process	Reference
Exfoliation or new structures	Graphene nanoplate	56.36 mmol/g at 25 °C, 30 bar	L. Y. Meng et al. [98]
Hybrid materials	Palladium-graphite nanoplatelets	5.10 mmol/g at 25 °C, 11 bar	A. K. Mishra et al. [99]
Hybrid materials	Graphene-based mesoporous silica	4.32 mmol/g at 75 °C, 1 bar	S. Yang et al. [100]
Hybrid materials	Chitosan-graphene oxide	4.15 mmol/g at 25 °C, 1 bar	A. A. Alhwaige et al. [101]
Hybrid materials	Polyindole-reduced GO	3 mmol/g at 25 °C,1 bar	M. Saleh et al. [102]
Hybrid materials	Graphene -Mn_3O_4	2.50 mmol/g at 25 °C, 0.8 bar	D. Zhou et al. [103]
Surface or edge functionalisation	Graphite	1.16 mmol/g at 30 °C, 1 bar	S.-M. Hong et al[104]
Surface or edge functionalisation	Graphitic nanoribbons	0.26 mmol/g at 30 °C, 1 bar	M. Asai et al. [105]

Chitosan-graphene oxide obtained by [101] showed 4.15 mmol/g as sorption capacity in standard conditions (ambient air) and for now it is one of the promising sorbents for gas sorption within the class of graphite/graphene-based adsorbents.

L. She et al. in [106] synthesized mesoporous MgO/carbon nanocomposites via the simple one-pot assembly of triblock copolymer F127, resol, and magnesium nitrate, followed by thermal curing and carbonization. In [106] the synthesis of ordered mesoporous MgO/carbon nanocomposites with cubic symmetry has been reported. The obtained material exhibiting strong basic superficial properties can be a candidate for selective adsorption and catalysis. The method of synthesis reported in [106] can be a valuable way for the design and synthesis of other types of mesoporous nanocomposite materials.

Nitrogen-doped polypyrrole-based porous carbons obtained in [107] exhibited good CO_2 uptake capacity in standard conditions (1bar, 25 °C): 2.7-3.9 mmol/g. The presence of a narrow microporosity together with a high density of N-containing basic groups are responsible for this high sorption ability. These nitrogen-doped polypyrrole-based porous carbons also show a high CO_2 adsorption rate, a good selectivity for CO_2 -N_2 separation and they can be easily regenerated.

Rich nitrogen-doped ordered mesoporous carbon for CO_2 adsorption was obtained by [108] in accordance with the synthetic process reported in Figure 6. Process of sorbent synthesis presented formation of bridge between resol molecules and commercial F127 due to electrostatic interactions during evaporation-induced self-assembly process- EISA process. Pyrolysis provided at 600 °C in nitrogen atmosphere for carbonization, dicyandiamide assure closed N species, whereas resol formed a stable framework, which guarantees ordered synthesis N-doped mesoporous carbons. This material exhibited unique structural features as high specific surface area and N-content, and high CO_2 uptakes (2.8-3.2 mmol/g) at standart ambient conditions (air, 25 °C and 1.0 bar). This material is effective in adsorption of gases in comparison with commercial activated carbons (with surface area of more than 2000 m^2/g) and specific surface area for N-doped mesoporous carbons is approximately 537 m^2/g. Prepared materials indicated higher selectivity in CO_2/N_2, moreover the following activation of material shows increasing of CO_2 uptake capacity up to 4.2 mmol/g at 10 °C. It was noticed that further growth of temperature leads to lower CO_2 adsorption capacity.
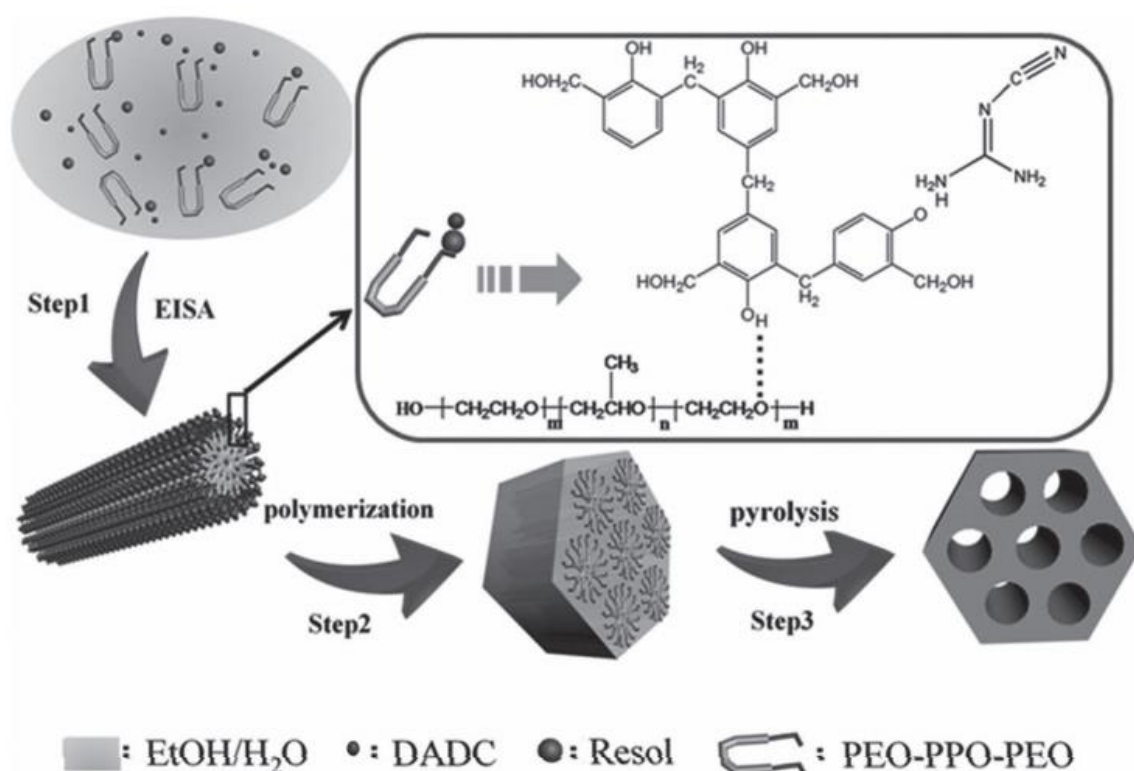

Figure 6 – The synthetic approach used for the production of ordered nitrogen-doped mesoporous carbon based on a one-pot assembly method using dicyandiamide. Adapted from [108]

The study of nanocomposite materials based on carbon modified by amino groups has become widespread in the global scientific community. The effectiveness of these sorbents for CO_2 sorption is known from the beginning of the search about possible solutions to prevent the increasing influence of carbon dioxide to the atmosphere.

Qing et al. [109] developed a solid amine adsorbent based on commercially available multi-walled CNTs (the length of CNTs was in the range of 10-20 μm, and the content of amorphous carbon in CNTs was less than 1.5 wt %) impregnated with tetraethylenepentamine by wet impregnation. The CO_2 uptake capacity was measured by monitoring online the concentration of CO_2 through a gas chromatograph connected directly to the adsorption column outlet. The surface area of the obtained samples after impregnating with tetraethylenepentamine decreased from 87.03 m^2/g to 34.31 m^2/g and lower [109]. The same happens for pore volume and average pore diameter. The CO_2 uptake ability of CNTs−tetraethylenepentamine composites could be elevated from 2.97 mmol/g up to 3.56 mmol/g by increasing the amine loading to 30 wt %. Moreover, the adsorption capacity can grow up to 3.87 mmol/g by using moisture (2.0% H_2O). But the further increase of the water vapor led to decreasing in the adsorption capacity.

Graphene oxide chemically modified by ethylenediamine, was crumpled using an aerosol process and encapsulated in TiO_2 nanoparticles to form core-shell nanostructures [110]. Ethylenediamine played an important role in CO_2 adsorption and further in enhancing the overall CO_2 photoreduction. The mechanism was described as follows: ethylenediamine reinforced the uptake capacity by forming alkylammonium carbamate species, the carbamate species were then photoreduced by irradiated TiO_2, generating CO and regenerating the amine groups [110].

The use of shungite as CO_2 adsorbent has also been investigated [111]. Shungite is a natural carbonaceous mineral; the main deposits are located in Karelia (Russia) and Koksu (named "Taurit", Kazakhstan) regions. This mineral is similar to elementary amorphous carbon with fragments of graphitic structures with an interlayer distance of 3.4 and 3.5 Å. It is also known that Shungite contains important amounts of fullerenes, mainly C_{60}. Shungite exhibits a mesoporous character with a narrow porous radius distribution and a small porous volume; its surface area is relatively low (approximately 22.54 m^2/g) and can reach 144.2 m^2/g after modifications. This material is widespread studied for adsorption processes appropriately water adsorption from different pollutants [111-113].

1.4.3 Biomass-derived carbons for gas adsorption applications

Biomass-derived materials have been also investigated as a cheap carbonaceous material for gas adsorption. Different kinds of biomass for production of carbon-based materials can be used: olive stones, sludge, bagasse, bamboo, wood, leaf, apricot stones, rice husk, nutshell, pine cones, coconut and so on. In addition, their widespread use can solve the problem of bio-waste disposal. Carbonization, coking and other pyrogenic processes (processes to convert the biomass organic fraction into carbon enriched materials by heating without oxygen) are considered to obtain the desired low-cost pyrogenic carbon material also called biochar.

It is important to consider pore characteristics of biomass-derived carbon materials: a pore diameter of 0.5-0.8 nm is optimal for CO_2 sorption at ambient temperature and pressure [114]. Usually, the biomass precursor is carbonized firstly and then it undergoes through activation process (physical or chemical activation); this

procedure allows the surface grow up. Notwithstanding, if the pore size becomes larger, decrease of interactions between the walls of the pores and carbon dioxide molecules can occur. In such case, increase in surface area may correspond less with increases in CO_2 uptake.

In general, textural characteristics of pyrogenic biomass-derived carbons (increased pore volume, high surface area and appropriate pore size) make them very suited for gas adsorption applications. The textural characteristics of pyrogenic biomass-derived carbon could be tuned by certain conditions of carbonization/pyrolysis [61].

Performances of a selection of biomass-derived materials in CO_2 adsorption along with some textural details are reported in Table 7. Data in Table 7 evidences a large variability of CO_2 uptake for biomass-derived carbons (biochars and biomass-derived activated carbons), likely due to the differences in the material's properties associated with nature of the starting feedstock and synthesis conditions.

Adsorption capacities of biochars, generally, are lower than activated carbons prepared by physical and/or chemical activation of biomass. This aspect can be interpreted considering that usually the porosity of biochars is much lower than activated carbons since they are materials obtained without activation processes.

Table 7 – CO_2 uptake at room temperature of selective biomass-derived materials. Adapted from Gargiulo et al. 2018 [115]

Feedstock	Type	Synthesis	S_{BET} (m^2/g)	V_{micro} (cm^3/g)	CO_2 Ads (mmol/g)	Ref.
1	2	3	4	5	6	7
Cellulose fibres	biochar	slow pyrolysis at 650°C	473	0.220	1.72	[115]
Cellulose fibres	biochar	slow pyrolysis at 700°C	593	0.250	2.33	[115]
P.nigra wood	biochar	slow pyrolysis at 600°C	217	0.140	1.12	[115]
Hickory wood	biochar	slow pyrolysis at 600 °C	401	n.a.[*]	0.92	[116]
Sugarcane bagasse	biochar	slow pyrolysis at 600 °C	388.3	n.a.	0.99	[116]
Sawdust	biochar	gasification at 850 °C	182	n.a.	1.5	[117]
Almond shell	biochar	single-step oxidation (3% O_2)	557	0.21	2.11	[118]
Olive stone	biochar	single-step oxidation (3% O_2)	697	0.27	2.02	[118]
Cellulose fibers	activated carbon	carbonization at 700 °C	499	0.193	2.2	[119]
Cellulose fibers	activated carbon	carbonization at 700 °C and physical activation	599	0.229	2.6	[119]

Table cantinuation 7

1	2	3	4	5	6	7
Cellulose fibers	activated carbon	carbonization at 800 °C and physical activation	863	0.334	3.77	[119]
Pine nut-shell	activated carbon	carbonization and chemical activation	1486	n.a.	5.0	[114]
Olive stone	activated carbon	physical activation	1479	0.348	3.05	[36]
Lignin	activated carbon	chemical activation	2246	0.271	2.38	[36]
Lignin	activated carbon	carbonization	71	0.235	2.20	[36]
Eucalyptus wood	activated carbon	chemical activation	1889	1.063	2.98	[120]
Bamboo	activated carbon	chemical activation	2332	0.37	4.5	[121]
African palm hells	activated carbon	chemical activation	1250	0.29	4.4	[122]
African palm hells	activated carbon	carbonization	365	0.05	1.9	[122]
Coconut shell	activated carbon	carbonization and physical activation	1327	0.55	3.9	[122]
Black locus	activated carbon	carbonization and physical activation	2511	1.16	4.92	[123]
Rice husk	activated carbon	carbonization and physical activation	927	n.a.	1.3	[124]
Rice husk	activated carbon	carbonization and physical activation	774	0.3	1.24	[125]
[*]n.a. – not analized.						

In some cases, low-cost biomass-derived sorbents exhibit higher CO_2 uptake capacities than commercial activated carbons (Table 7, lines 1 and 3).

Starting from biomass-derived materials, nanocomposites for CO_2 capture applications have also been proposed. Nanocomposites were synthesized by combining Pine cone-based AC and polyaniline [126]. The CO_2 uptake at ambient conditions was significantly increased from 1.91 mmol/g for raw AC up to 3.16 mmol/g for the synthesized nanocomposite.

Nowrouzi et al. developed biomass-derived AC/metal activated by phosphoric acid oxides composites with the highest sorption capacity (6.78 mmol/g at 30 °C) [127]. Activated carbon one of promises materials for preventing influence of greenhouses gase, including carbon dioxide, especially received by biomasses, this way get double eco-environmental reasons.

1.4.4   Iron oxide-carbon hybrids for CO_2 adsorption

Different papers are available in the open literature report on the performances of carbon/magnetite composites in CO_2 adsorption. Iron oxides are widely distributed in nature, either in rocks and stones, especially iron ore, or in soils. Iron oxides, also

synthetic ones, have a huge advantage in safety for life with comparison other nanomaterials. That's materials serve either as pigments or for their magnetic properties.

Magnetite (or ferromagnetite, FM) is one of the most popular iron oxides. Its chemical formula is Fe_3O_4 (it can also be written as $FeO \cdot Fe_2O_3$; iron oxide II, III) and its distinctive feature is the strong magnetism which is not available in other iron oxides [128].

Mishra et al. synthesized multiwalled carbon nanotubes [129] decorated with magnetite particles and Fe_3O_4-graphene nanocomposites [130] for carbon dioxide capture by physicochemical adsorption. The maximum adsorption capacity does not jump over 0.3 mmol/g at ambient conditions.

Following the same approach Alfe et al. in [131] investigated the CO_2 adsorption behavior of materials prepared by coating a low-cost commercial carbon black with magnetite fine particles (FM). Carbon black content more than 99 percent of pure carbon.

In [131] five different CB loads were considered for preparation of the sorbents. Composite materials were synthesized in one-pot synthetic approach by exploiting a co-precipitation strategy allowing the iron oxide particles to form in presence of CB. The one-pot strategy was proved to allow homogeneous incorporation as the carbonaceous material such as magnetite particles into the composites. CO_2 uptakes were evaluated on the basis of breakthrough curves measured at ambient air condition in the laboratory scale fixed bed micro-reactor (Adsorption tests with CO_2 $C_0 = 3\%$ vol.; inlet flow rate of CO_2/N_2 gas mixture = 15 Nl/h).
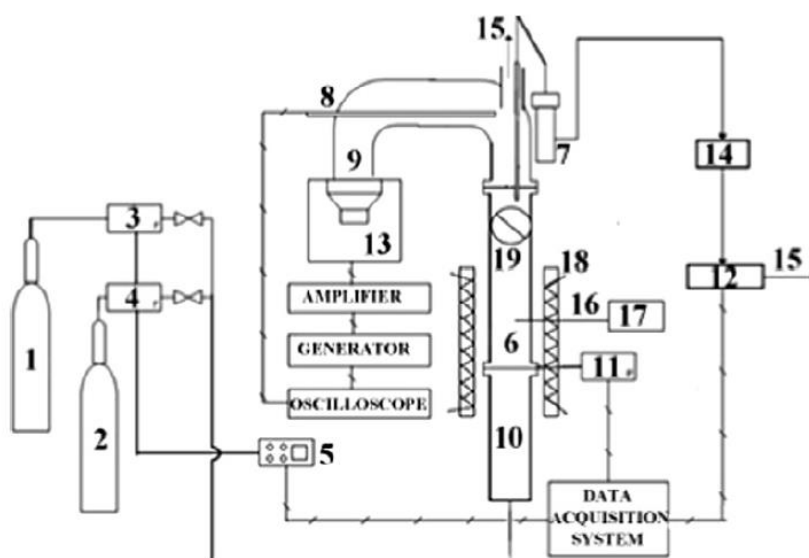
1 – nitrogen gas cylinder; 2 – carbon dioxide gas cylinder; 3 – N_2 flow meter; 4 – CO_2 flow meter; 5 – controller; 6 – fluidization column; 7 – filter; 8 – microphone; 9 – sound guide; 10 – wind-box; 11 – pressure transducer; 12 – CO_2 analyzer; 13 – loudspeaker; 14 – pump; 15 – stack; 16 – thermocouple; 17 – t° controller; 18 – heating jacket; 19 – two-way valve.

Figure 7 – Sound assisted fluidized bed for adsorption tests

After work on laboratory scale static fixed bed the best adsorbing composite (50 wt.% of CB load, 16.5 mg CO_2/g) of five's previous analyzing was then produced on a larger scale and tested in the prototypal sound assisted fluidization apparatus. The schematic figure with detailed explanations of sound assisted fluidization bed was presented below (Figure 7).

Under the sound assisted fluidization conditions the CO_2 uptake was considerably increased to about 20 mg CO_2/g.

Due to the encouraging performances in both fixed and fluidized bed reactors, a characterization of the high adsorbed CO_2 CB-FM composite by both kinetic and thermodynamic points of view was performed under dynamic conditions [132].

2 EXPERIMENTAL SECTION

2.1 Method of preparation carbonized rice husk

Rice husk (RH) has been used as the starting material for the development of CO_2 sorbents because of its wide availability as waste material in all rice producing countries. This material has wide perspectives for technological application since it can be transformed to different type of fuels and chemicals through different thermochemical conversion methods [133]. Kazakhstan is a big rice producing country: according to the Statistics Committee of the Ministry of National Economy of the Republic of Kazakhstan there are more than 274 tons of unmanufactured rice vegetates in our region as of 1 January, 2019 and 20 % of this amount consists of RH [134].

Production of sorbent materials starting from RH can mitigate different environmental issues: use of agricultural wastes reduces disposal issues and the valorization of end-of-life materials as sorbents materials (carbon dioxide or heavy metals from wastewater) faces remediation issues.

Raw material used in this project was received from a deposit located in the Bakanas Village, Balkhash District of Almaty Region [135-137].

Carbonization process of raw RH (cRH) was carried out in an auger furnace (Figure 8) operated in argon atmosphere at 500-800 $^{\circ}$C degree for 3 hours in Institute of Combustion Problems, Almaty, Kazakhstan. The level of processing of the carbonaceous raw material approximately achieves 80 % of yield. The consumption of blow water (running or reverse) is 5 L per hour and a stream activator (air) makes up 0,005m^3 per kg in the auger furnace demonstrated below.

Figure 8 – Rice husk carbonization in auger furnace

cRH was washed and dried before further processing and application. The carbonized sample was characterized by different physicochemical methods such as: thermogravimetry, proximate analysis, scanning electron microscopy equipped with X-ray source for elemental analysis, bulk elemental analysis, infrared spectroscopy, x-ray diffraction, etc.

Details about the different instrumental techniques are reported in the following sections.

2.2 Methods of preparation carbon-based nanocomposite materials for CO_2 adsorption

2.2.1 Methods of alkali treatments of carbonized rice husk

Alkali treated sorbents based on cRH were produced by a base-leaching procedure. A samples series was obtained by treating different amount of cRH (from 1 to 10 g) with two strong bases: NH_4OH (28% water solution) and NaOH (5M) [135]. The obtained samples were labeled as cRH-NH_4OH and cRH-NaOH, respectively. cRH in an amount ranging between 1 and 10 g was suspended into 200 mL of deionized water by treatment in ultrasound bath for 20 min. The mixture was kept at 30° C for 30 min under stirring. After that, 10 mL 28% NH_4OH or 100 mL of 5M solution of NaOH was added. The mixture was kept for 1/2/4/6 h at 90° C under stirring. The suspension then was reached ambient room temperature and the solid was recovered by filtration and washed with distilled water until neutrality. The solid was dried up in oven at 100 °C.

Different starting amounts of cRH and different reaction times were explored to evaluate the effect of both parameters on the reaction yield.

The scheme of the reaction workup and the yields of the produced sorbents are reported below in Figure 9.
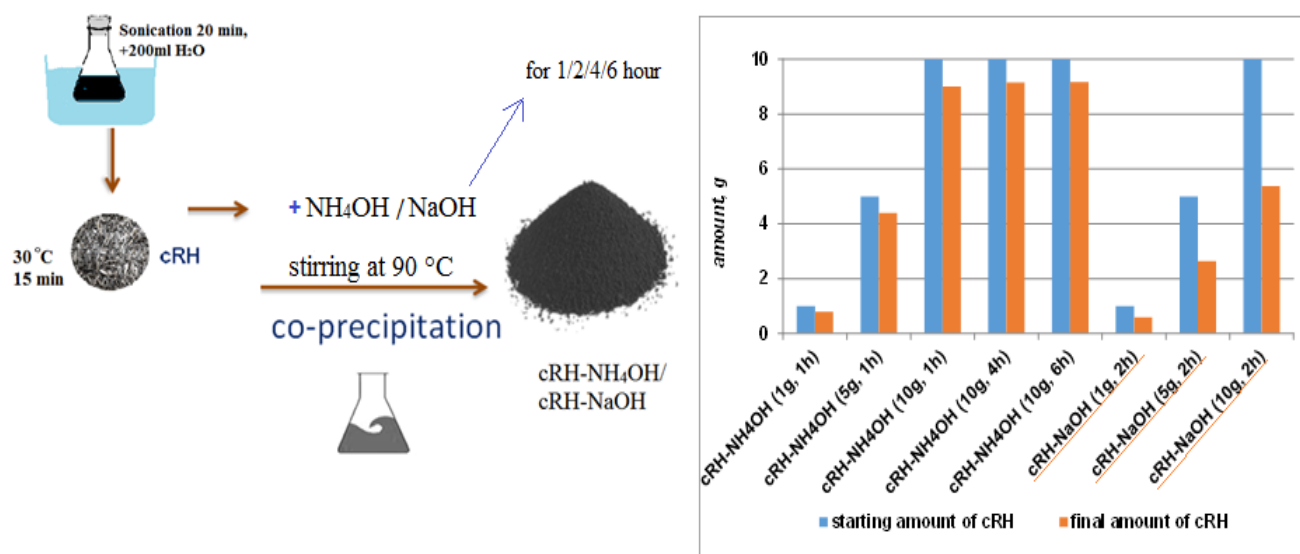

Figure 9 – The reaction scheme and the yields of the cRH-based sorbents produced by alkaline treatments

According to Figure 9, the yields of sorbents belonging to cRH-NH_4OH series ranging between 85-86 % with respect the starting cRH amount and those sorbents belonging to cRH-NaOH series are between 52-59%. The reason of such difference between the yields of the two treatments is due to incomplete removal of silica in case of the cRH-NH_4OH, as it will be explained later on in the result and discussion section.

2.2.2 Method of carbonized rice husk-magnetite composites fabrication

Seven different composites based on cRH and magnetite (FM) were produced by varying the starting amount of cRH (0.10 g for cRH-FM-1; 0.35 g for cRH-FM-2; 0.60 g for cRH-FM-3; 0.90 g for cRH-FM-4; 1.20 g for cRH-FM-5, 3.00 g for cRH-FM-6 and 6.00 g for cRH-FM-7) while the amount of magnetite precursors ($FeCl_3 \cdot 6H_2O$, 1.4 g and $FeSO_4 \cdot 7H_2O$, 0.70 g) is kept constant. These composites were produced by adapting the synthetic strategy proposed in Alfe et al. based on the precipitation of iron oxide in presence of carbonaceous particles (nanostructured carbon black) acting as support (co-precipitation strategy) [131]. Selected amount of cRH was suspended into 200 mL of de-ionized water by sonication in ultrasonic bath for 20 minutes, then 50 mL aqueous solution of two magnetite precursors $FeCl_3 \cdot 6H_2O$ (accounted amount 1.4 g) and $FeSO_4 \cdot 7H_2O$, (amount 0.70 g) was added. This mixture was kept in the magnetic stirrer at 30 °C for 30 min. Onwards, 10 mL of 28% NH_4OH solution was added in until pH at 10 degrees, allowing the magnetite precipitate over the cRH. This mixture was kept under stirring for 1 h at 90 °C. After that, the solid was recovered by filtration and washed until neutral pH was reached, dried in a muffle furnace at 100 °C [131, 138].

The amount of cRH and FM precursors used for production of each composite of cRH-FMs series and corresponding yields is reported in Table 8 together with the data on synthesis of pure magnetite (FM). For sake of completeness, the data about the cRH treated with ammonia solution in absence of magnetite precursors is also reported.

A visual representation of the mass percentages of cRH and FM which was counted using yield data is reported in Figure 10. The values were calculated on the basis of the amount of composite recovered at the end of reaction and keeping constant amount of FM in each material.

Table 8 – Amount of cRH and FM precursors used for the synthesis of cRH-FM series composites and relative yields

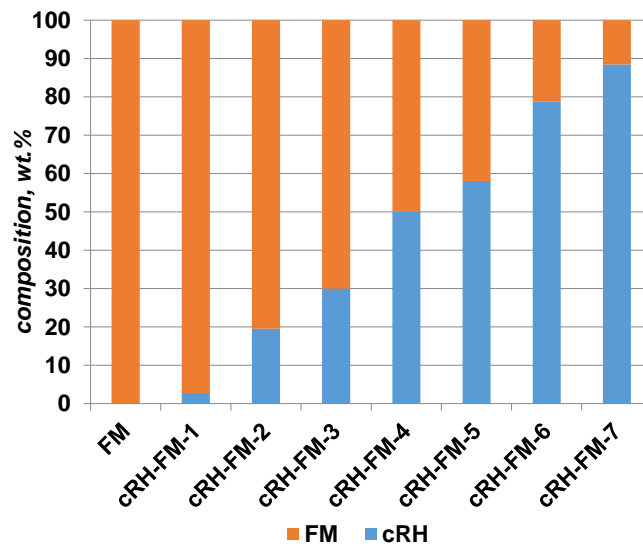| Composite material	Theoretical cRH amount (%)	Theoretical FM amount (%)	Starting amount of cRH (g)	Starting amount of $FeCl_3 \cdot 6H_2O$ (g)	Starting amount of $FeSO_4 \cdot 7H_2O$ (g)	Yield (g)
FM	0	100	0	1.4	0.70	0.70
cRH-FM-1	12	88	0.10	1.40	0.70	0.72
cRH-FM-2	33	67	0.35	1.40	0.70	0.87
cRH-FM-3	50	50	0.60	1.40	0.70	1.00
cRH-FM-4	56	44	0.90	1.40	0.70	1.40
cRH-FM-5	63	37	1.20	1.40	0.70	1.67
cRH-FM-6	81	19	3.00	1.40	0.70	3.30
cRH-FM-7	90	10	6.00	1.40	0.70	6.07

Figure 10 – Contents of FM and cRH in cRH-FM series composite

2.2.3 Method of carbonized rice husk-nanoparticulate magnetite composites fabrication

Starting from the procedure reported in [139] for the preparation of magnetite nanoparticles (nanoparticulate magnetite, nFM) in presence of tetramethylammonium hydroxide (TMAOH) surfactant, a new approach for the production of 5 different cRH-nFM composites was proposed.

nFM nanoparticles were produced as follows: 60 mL of an aqueous solution of $FeCl_3 \cdot 6H_2O$ (5.4 g) and $FeSO_4 \cdot 7H_2O$ (5.3 g) and 60 mL of 5 M NaOH solution were mixed together into a reactor containing 80 mL of distilled water at 90 °C. The mixture was then kept under N_2 atmosphere and under vigorous mixing for 2 h at 90 °C. A black nFM precipitate was early formed. After the reaction time, magnetite nanoparticles were stabilized by the slow addition of 10 mL of TMAOH 25% water solution. The suspension was kept at 90 °C for further 30 min. After that, the solid was recovered by filtration and washed with de-ionized water until the neutral pH was reached. The final suspension is dried overnight in a muffle furnace at 100 °C.

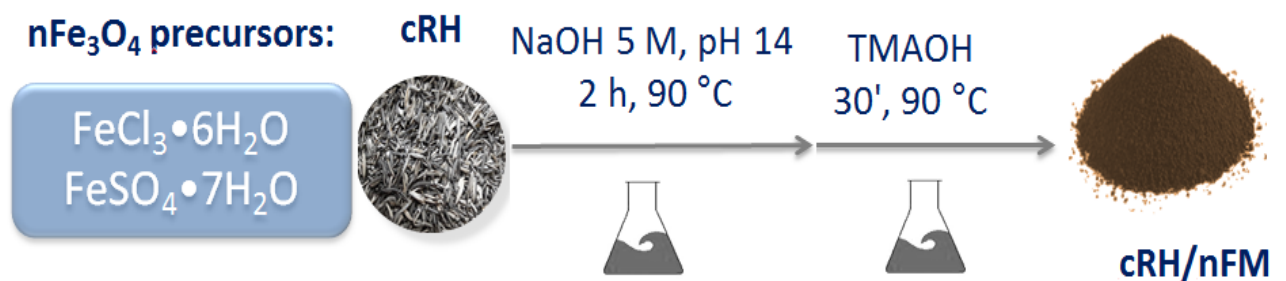A scheme of the synthetic approach is shown in Figure 11.

Figure 11 – Schematic description of the synthesis of the composite materials based on cRH and nFM (cRH-nFM-a – e series)

Four composite materials (cRH-nFM-a – d) were produced according to the above reported procedure by varying the amount of cRH while the nFM precursors were kept constant (Table 9, looking to Starting amount of $FeCl_3 \cdot 6H_2O$ and $FeSO_4 \cdot 7H_2O$). cRH-nFM-e was obtained by using half of nFM precursors with respect to the cRH-nFM-a – d composites.

The amount of cRH and nFM precursors used for production of each composite of cRH-nFM series and corresponding yields are reported in Table 9 together with the data on synthesis of nFM.

A visual representation of the mass percentages of cRH and nFM in each composite is proposed in Figure 12 [140].

Table 9 – Amount of cRH and nFM precursors ($FeCl_3 \cdot 6H_2O$ and $FeSO_4 \cdot 7H_2O$) used for synthesis of cRH-nFM series and relative yields

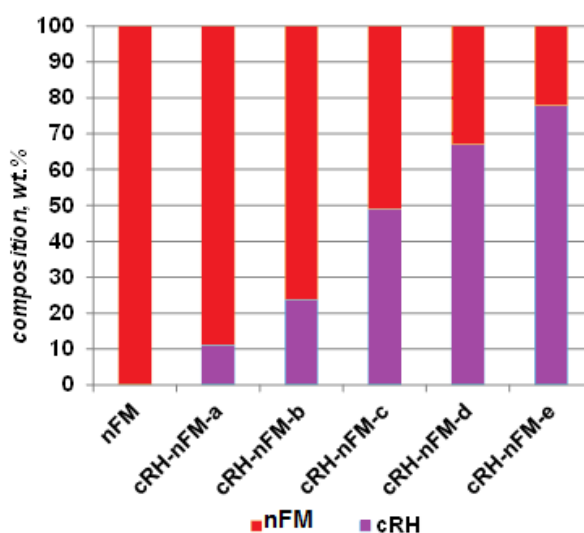| Composite material	Theoretical cRH amount (%)	Theoretical nFM amount (%)	Starting amount of cRH (g)	Starting amount of $FeCl_3 \cdot 6H_2O$ (g)	Starting amount of $FeSO_4 \cdot 7H_2O$ (g)	Yield (g)
nFM	0	100	0	5.4	5.3	3.2
cRH-nFM-a	11	89	0.35	5.4	5.3	3.6
cRH-nFM-b	24	76	1.2	5.4	5.3	4.2
cRH-nFM-c	49	51	5.0	5.4	5.3	6.0
cRH-nFM-d	67	33	10	5.4	5.3	9.7
cRH-nFM-e	78	22	10	2.7	2.6	7.2

Figure 12 – Theoretical contents of nFM and cRH in samples belonging to cRH-nFM series

2.2.4 Method of obtaining composites based on carbon black and nanoparticulate magnetite

Another set of nFM-based composites was produced by using a commercial carbon black (CB). This set of materials was prepared in order to compare data collected on cRH-nFM series with the data collected on composite materials containing a model carbonaceous support instead of a biomass-derived one. A furnace black, N110 type (ASTM classification) was provided by Sid Richardson Carbon Co and used as received. The density of this carbon material at 25 °C is 1.8 g mL^{-1}, the specific surface area of this chemical material is 143 m^2/g. CB presents as a narrow monodispersion (around 160 nm) of chain-like aggregates of coarse spherical elementary particles. Average diameters of CB particles about 15–20 nm [131].

The composites of the CB-nFM series were produced accordingly to the synthetic procedure used for the preparation of the materials belonging to the cRH-nFM series, by simply changing the carbonaceous materials acting as support for nFM.

The amount of CB and nFM precursors used for production of each composite of CB-nFM series and corresponding yields are reported in Table 10 along with the data on synthesis of pure nFM. For sake of completeness, the data referred to the CB treated with NaOH solution in absence of nFM precursors is also reported.

Table 10 – Amount of CB and nFM precursors (FeCl$_3$·6H$_2$O and FeSO$_4$·7H$_2$O) used for the synthesis of CB-nFM series and relative yields

Composite material	Theoretical CB amount (%)	Theoretical nFM amount (%)	Starting amount of CB (g)	Starting amount of FeCl$_3$·6H$_2$O (g)	Starting amount of FeSO$_4$·7H$_2$O (g)	Yield (g)
nFM	0	100	0	5.4	5.3	3.2
CB-nFM-a	9	91	0.35	5.4	5.3	3.5
CB-nFM-b	39	61	1.2	5.4	5.3	5.2
CB-nFM-c	61	39	5.0	5.4	5.3	8.2
CB-nFM-d	76	24	10	5.4	5.3	13.2
CB-nFM-e	86.5	13.5	10	2.7	2.6	11.8
CB-NaOH	100	0	10	0	0	9.8

2.3 Methods of characterization of carbon-based nanocomposite materials for CO$_2$ adsorption

2.3.1   Elemental analysis

Carbon, hydrogen and nitrogen contents in the samples were measured with LECO CHN 628 elemental analyzer (Figure 13) according to ASTM E870 procedure and using ethylenediaminetetraacetic acid (EDTA) as standard one. For each sample, at least two replicates were performed and average values are reported. For LECO CHN 628 elemental analyzer the maximum relative error was approximately 0.7 %.

This instrumental technique is ideal for determining carbon, hydrogen, and nitrogen contents from a wide variety of sample types (from food to fuels) including

solids, liquids, volatile and viscous samples. The CHN operating mode is the most widely used. A range of reagents and ability to optimize the combustion parameters offer flexibility for virtual analysis of any sample types. Interfering elements such as halogens and sulfur should be removed before detection [141].

Figure 13 – Elemental analyzer CHN 628 manufactured by LECO in operation (instrument is used at the Institute for Research on Combustion in Napoli, Italy)

CHN mode is based on the classical Pregl-Dumas method where samples are combusted in the pure oxygen environment and the resultant combustion gases are measured in an automated fashion (Figure 14).

Samples were encapsulated in tin or aluminum vials and inserted in the combustion zone where in presence of excess oxygen and combustion reagents at 950 °C, the samples are combusted and completely oxidized. After oxidation, the gas mixture passes through the reduction section where it was reduced to elemental gases (CO_2, H_2O, N_2 and SO_2). Finally, gases are separated in the separation zone and

quantified by a chromatograph coupled with a thermal conductivity detector and the results converted in N, C, H wt. % in our used case (and S in CHNS configuration).
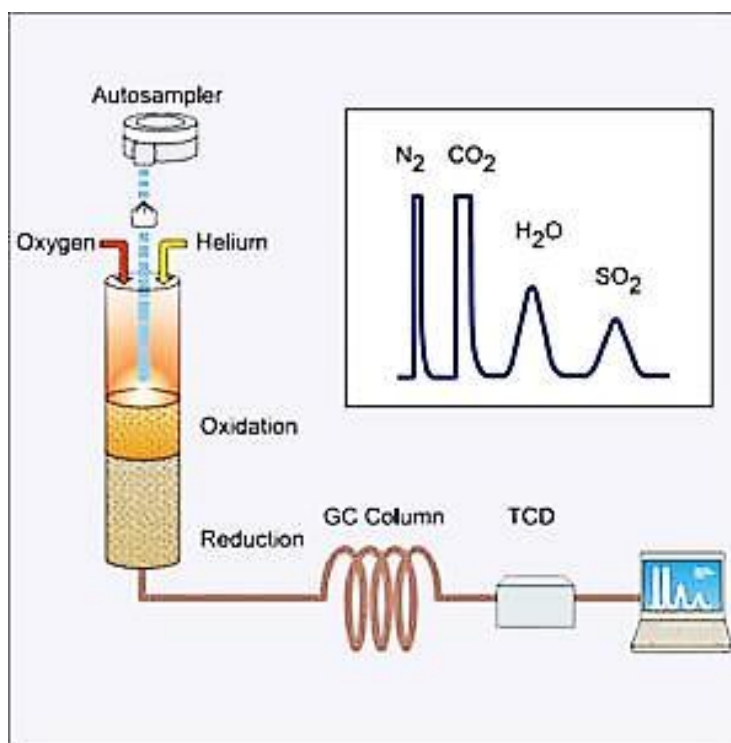

Figure 14 – Schematic diagram for an elemental analyzer

2.3.2 Thermogravimetry

Thermogravimetric analysis (TGA) is the most widely used thermal method for characterization of solid samples. It is based on the measurement of mass loss of a material as a function of the heating temperature.

During the analysis, the sample mass loss was continuously measured against the heating temperature (temperature gradients or uniform temperature or a combination of both can be applied). The thermogravimetric curve (TG curve) is a plot of the sample mass change versus temperature (or time) and a fundamental tool to describe transformations undergone by the sample upon progressive heating including the stability range [142].

The first main application of TGA is evaluation of material purity and thermal stability. The second application is the determination of characteristic de-solvation, sublimation, vaporization temperatures of a material; the third one is study of sorption, desorption, chemisorptions phenomena [143].

The thermal stability of the samples was evaluated on a TGA 701 LECO analyzer. Samples were heated in the oxidative environment (air) from 50 °C up to 800 °C at a rate of 10 °C per min^{-1}.

Proximate analysis of raw and carbonized rice husk samples was also performed using the same instrument by changing the temperature ramp according to ASTM 5712 method. Proximate analysis ensures the determination of: moisture, volatiles, fixed carbon and ashes content. The following temperature scheme was applied:

44

1) heating up to 110°C at 5 °C min^{-1}, under N_2 atmosphere, holding at 110°C up to constant mass (moisture content evaluation);

2) heating up to 950°C at 10 °C min^{-1}, under N_2 atmosphere, holding at 110 °C for 10 minutes (volatiles content evaluation);

3) cooling down to 600 °C under N_2 atmosphere, then switching to O_2 and heating up to 800 °C and then holding at 800°C to constant mass (ashes content evaluation).

4) The content of fixed carbon is evaluated by difference.

A typical scheme of a TG instrument is reported in Figure 15 along with description of different components.
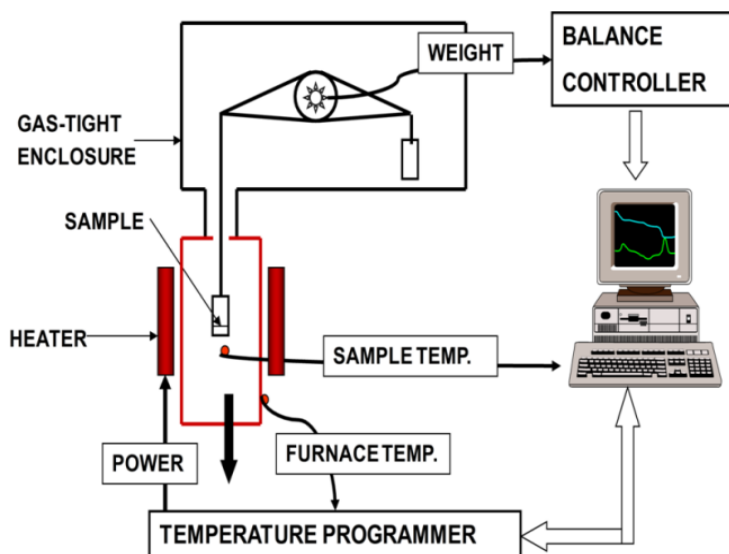

Figure 15 – Schematic diagram of thermogravimetric analyzer

The measurements were performed at IRC-CNR of Naples.

2.3.3 Fourier-transform infrared spectroscopy

Infrared spectroscopy is one of the most useful and widely used methods to perform structural analysis of solid materials. As the other techniques classified as spectroscopies, IR spectroscopy is based on the interaction between matter and light. In particular, IR uses electromagnetic radiation in the wavelength region between 1000 μm-800 nm (wavenumber 10-12500 cm^{-1}).

There are three well defined IR regions (near, mid and far):

1) Near infrared (12820-4000 cm^{-1});

2) Mid-infrared (4000-400 cm^{-1});

3) Far Infrared (400-33 cm^{-1}).

The low energies encountered within the entire infrared region are not sufficient to cause electronic transitions but they are large enough to cause changes in the frequency and amplitude of molecular vibrations. This allows the determination and the identification of molecular structure.

Each of the three above defined infrared regions potentially provides different structural information:

- Far-Infrared (400-33 cm^{-1}): vibrations of molecules containing heavy atoms, molecular skeleton vibrations and crystal lattice vibrations;
- Mid-Infrared (4000-400 cm^{-1}): useful for organic analysis;
- Near Infrared (12820-4000 cm^{-1}): overtones; very useful for quantitative analysis;

IR spectroscopy has a very well gained reputation for its power, flexibility, and reliability. Information achievable with IR spectroscopy for organic analysis includes:

1) The type of atoms within the molecule;

2) The type of bonds between atoms;

3) The molecular structure.

Most IR spectrometers can be categorized into two classes: dispersive and Fourier Transform instruments (FTIR). FTIR spectrometers consist of an IR source, interferometer, sample cell or chamber, detector and a laser (infrared source). A schematic diagram of a typical FTIR spectrophotometer is reported in Figure 16.
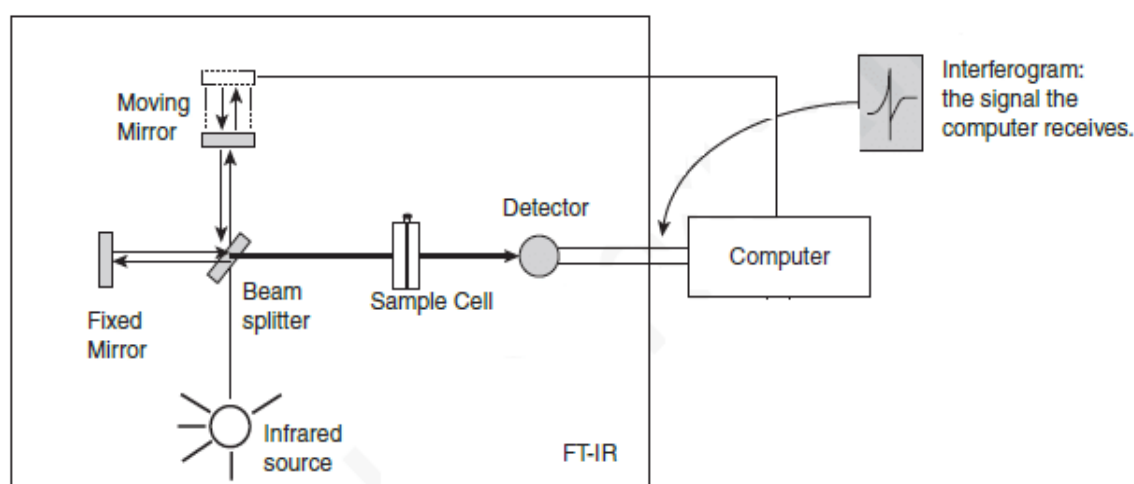

Figure 16 – Schematic diagram of a typical FTIR spectrophotometer

IR radiation from the source strikes the beam splitter and is separated into two beams. One beam is transmitted through the beam splitter to the fixed mirror while the other beam is reflected from the beam splitter to the moving mirror. Both mirrors reflect the radiation back to the beam splitter where the two beams interfere to produce an interferogram. Some of the wavelengths of IR radiation will be absorbed by the sample and some of them will pass through (they are transmitted). Transmitted IR radiation is measured by the detector resulting in a unique IR spectrum for the sample of interest. The IR spectrum of a given molecule is its unique fingerprint.

Historically, infrared spectra have been represented as percentage of transmittance versus either the wavenumber or the wavelength. By convention, the wavenumbers are plotted in decreasing of order from left to right.

Vibrational frequencies of certain functional groups will correspond to the adsorption of certain wavelengths of IR energy. Adsorption of these wavelengths by sample can therefore act as a diagnostic or fingerprint to indicate possible presence of

these groups within analysis. Some typical vibrational frequencies of carbon-based materials are shown in the Figure 17.
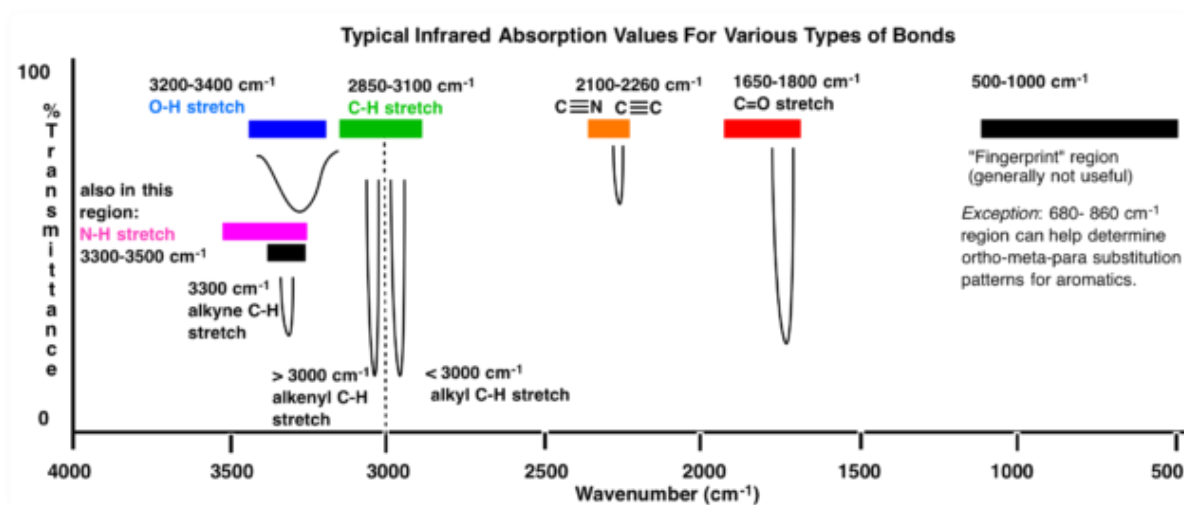

Figure 17 – Some typical vibrational frequencies of carbon-based materials

FTIR spectra were acquired on a Nicolet 5700 spectrophotometer using both the attenuated total reflectance (ATR) or transmittance methods.

In case of transmittance methods, solid sample dispersions were prepared as pellets by mixing and grinding powdered materials (0.5-0.8 wt.%) with KBr. Pellets of solid mixtures were obtained upon compression at 10 Ton for 10 minutes. In case of ATR method, the spectra were acquired directly on the powdered samples without KBr addition by using a germanium crystal.

In both configurations, the spectra were recorded in the 650-4000 cm^{-1} wavenumber range by collecting 32 scans and correcting the background noise.

2.3.4 Inductively coupled plasma-mass spectrometry

Inductively coupled plasma-mass spectrometry (ICP-MS) widely used for trace metal analysis. The reasons for increasing of ICP-MS popularity can be resumed in the following circumstances:

- The detection limits of ICP-MS devices do not exceed one part per trillion (ppt) level for a lot of elements in the periodic system;
- The analytical working range is nine orders of magnitude;
- High performance among all methods;
- Easy accessibility of isotopic analysis.

ICP-MS technique lets obtain the measurement of general part of chemical elements in the periodic system both in a quantitative or semi-quantitative way. This method allows simultaneously determine trace amounts of elements against the background of others which are in macroconcentrations. Also analyzing is very reliable and at the same time extremely sensitive, therefore, it finds application in inorganic elemental analysis – mainly applied for detection of heavy metals traces. Samples are injected into argon plasma as aerosol droplets. Before entering the mass spectrometer (mass filtration device), singly charged ions are formed from an aerosol. To obtain

these ions, the sample (in the form of aerosol drops) is dried by plasma, the molecules in the atoms dissociate and then remove the electron from atoms (Figure 18).
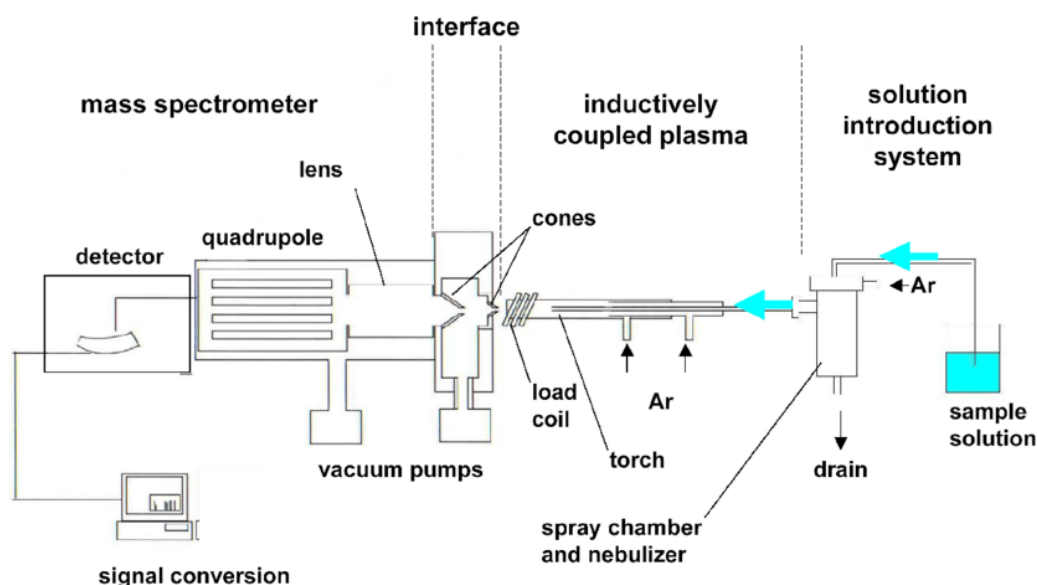

Figure 18 – Schematic major components of ICP-MS

An ICP-MS instrument consists of the following components (according to Figure 18) [144]:

- Sample introduction system. Consists of spray chamber and a nebulizer. Procure the means for introducing samples into the apparatus;

- RF coil and ICP torch. It's a form of argon plasma which is responsible for ion source of the ICP-MS;

- Interface. It connects the atmospheric pressure of inductively coupled plasma ion source with the high vacuum MS;

- Vacuum system. Serves as a guarantee of high vacuum for quadrupole, detector and ion optics;

- Collision (reaction cell). Previous of the mass spectrometer and it is applied for removal of interferences which can worsen detection limits reached. There is also a universal cell that can be used both in the collision cell and in the reaction cell mode;

- Ion optics. It directs the desired ions to the quadrupole, ensuring that neutral species and photons are emitted from the ion beam;

- Mass spectrometer. Operate as a mass filter for sorting ions (by their mass-to-charge ratio (m/z);

- Detector. For counting single ions leaving the quadrupole;

- Data handling and system controller. Controllers of all aspects of instrument control, data processing for reception of final assembly results.

The quantitative determination of iron in the composite material was performed on Agilent ICP-MS 7500ce spectrometer. Each sample was prepared as follow: 50 mg of powder was suspended with deionized water and digested with HNO_3 (65%) and H_2O_2 (30%) for 30 minutes by microwave heating. The digested sample after filtration was diluted with deionized water and analyzed. Each measurement was repeated twice

and the metal content was established by extrapolating from a four-point calibration curve.

2.3.5 Specific surface area measurements

The measurement of the specific surface area and the other textural properties (i.e. pore size distribution) is founded on the physisorption of gases or vapors over a solid (Figure 19).
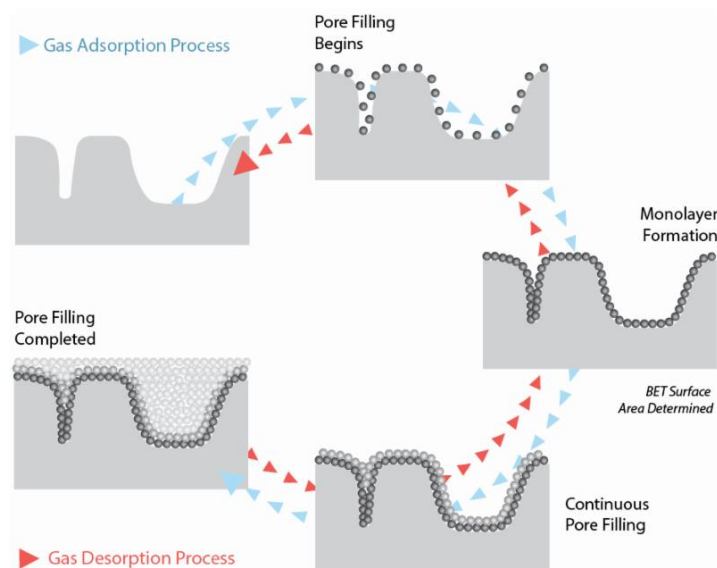

Figure 19 – Gas adsorption/desorption process

The quantity of adsorbed gas relies on the nature of the solid-gas system, as well as from such parameters as temperature, pressure, porosimetry and specific surface area of the adsorbent. For an adsorbed gas in the determined solid sorbents at a fixed temperature, the adsorbed amount is a function of the relational pressure of the adsorbate, P/P_0, where P - partial pressure of the adsorbate in the gas phase, P_0 -the pressure of the adsorbate saturation at the adsorption temperature [145]. The adsorption isotherm can be obtained by representing the adsorbed amount versus P/P_0.

The frequently applied standard procedure for definition of the specific surface area from the adsorption isotherm is the Brunauer-Emmett-Teller gas adsorption method (BET) [145].

BET specific surface areas of the obtained samples in framework of this dissertation were measured by Ar adsorption at 87 K using Quantachrome Autosorb 1 apparatus. The samples were outgassed under vacuum at 120 °C for 3 h before each analysis.

The adsorption/desorption isotherms were also processed in accordance with the Barrett-Joyner-Halenda (BJH) model to evaluate the pore size distribution and the pore volume [146].

2.3.6 Scanning electron microscopy

The electron microscopy makes receive information about structure of micro- or nanoobjects. Microscopy techniques are applied for investigation of the structure and

morphology of carbonaceous materials such as size, distribution of the particles and shape, also at a higher magnification - graphene layer orientation. Scanning electron microscopy (SEM) is a microscopy technique able to produce images with high resolution and depth of field and provides useful tools for probing structural and surface characteristics of materials.

SEM used with primary beam of electrons that operating with the studied sample in a vacuum environment. Further it leads to the emission of secondary electrons, photons, X-rays, backscattered electrons, also to excitation of phonons and diffraction in specific certain conditions. From the investigated specimen surface the secondary electrons are emitted, then collected and displayed to provide a high resolution of the micrography. Variety of factors affected to the depth of field and resolution of the image such as interaction volume, beam energy, beam current and the final spot size, which can be controlled as illustrated in Figure 20 [147].
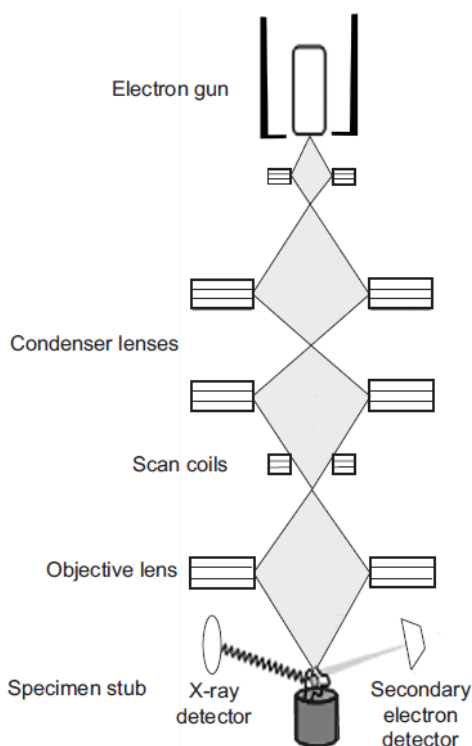
Figure 20 – Schematic view of SEM [147]

SEM imaging was performed at al-Farabi KazNU in National Nanotechnology Open Laboratory by using FEI Quanta 3D 200i with support of Guseinov Nazim. Also SEM images of several materials were presented with supporting of IRC-CNR of Naples, research was done using FEI Inspect TMS50 Scanning Electron Microscope. Scanning was conducted on the powdered sorbents; preliminary dried and coated spraying with a negligible slim-layer gold to escape charging.

2.3.7 Atomic force microscopy

Atomic Force Microscope (AFM) was presented by Binnig and Quate in 1986 to avoid the confines of other microscopy technologies.

AFM elaborates images approximately at the atomic resolution level by exploring the surface of the specimen. Quantitative determination of forces between the cantilever tip and the specimen surface recreates the image. Ultra-small cantilever tip at the end of the AFM probe gives extremely maximum resolution of obtained images. AFM was primarily developed to investigate material surfaces; later it was modified to analyze biological samples.

AFM trace a three-dimensional 3D image of the surface topography of the analyzed probe under invariable applied force which provides a high resolution image.

AFM is being widely used as an imaging tool for the following reasons:

1) Maximum resolution 3D x, y and z can be received. The resolution in the x–y plane ranges from 0.1-1.0 nm, in the z direction it is 0.001 nm (atomic level);

2) AFM images provided principle free of artifacts;

3) AFM did not require any special specimen preparation or vacuum environment. Imaging can also be prepared in a liquid medium which allows to analyze the specimen in the almost native condition (for example, biological samples);

4) Preparation of the samples for AFM analysis is comparatively easy and requires less time.

Cantilever (probe) of AFM made from silicon or silicon nitride such as having a very low spring constant to image the specimen. At one end the cantilever has very sharp tip, approximately 100-200 nm long and 20-60 nm rad. curvature which is fabricated using semiconductor producing technologies. The cantilever investigates the surface of the specimen by gradually shifting backward and forward throughout the surface. Piezoelectric crystal lifts up or moves down the cantilever for encouragement of cantilever permanent bending (Figure 21).
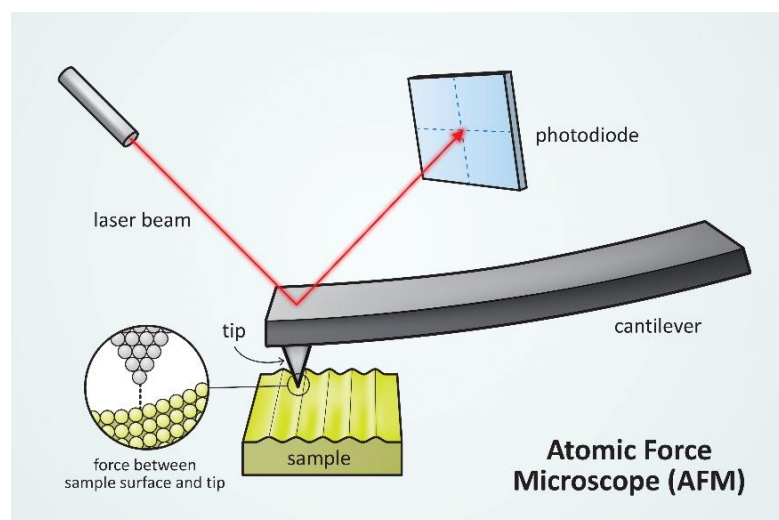

Figure 21 –AFM operation mode

The force actuating the sharp tip depends on the difference in the surface height of the sample and consequently provides bending of the probe. A laser beam is permanently reflected from the probe in the direction to a position-sensitive photo detector which consists of four side by-side photodiodes. Further actual probe position is calculated based on laser beam detection which shows the bending. Accordingly, AFM records a 3D image of the specimen's surface topography at the permanent attached force (in each point of nanonewton range) which provides for high resolution image with absent of any impairment of the specimen surface as the tip is not contacted with sample surface.

When the cantilever tip explores the surface of the specimen, the force between the tip and the sample is changed. This variation in force is sensed by the sharp tip applied to the flexible cantilever. The amount of force between the cantilever and the specimen depends on the spring constant of the probe as well as the distance between the cantilever and the specimen surface too. This force is reported in accordance with Hooke's Law:

$$F = -k \times \Delta x \qquad (4)$$

where is: F – force;

k - spring constant;

x - probe deflection.

Different types of forces such as double layer forces, capillary forces, adhesive forces and van der Waals forces adjusted the interactions between the specimen surfaces and the tip of the probe. Among them, van der Waals force is most often associated with atomic force microscopy. In the interaction region, the distance space between the specimen surface and the tip of the probe is under than a several angstroms (Å). In this case, the tip of cantilever experiences renouncing van der Waals force. The tip of probe is several tens to hundreds Å away from the specimen surface in the contactless region, hence sensed an attractive van der Waals force. Variety of the scanning regimes act in different regions of van der Waals force versus distance curve is presented in Figure 22.
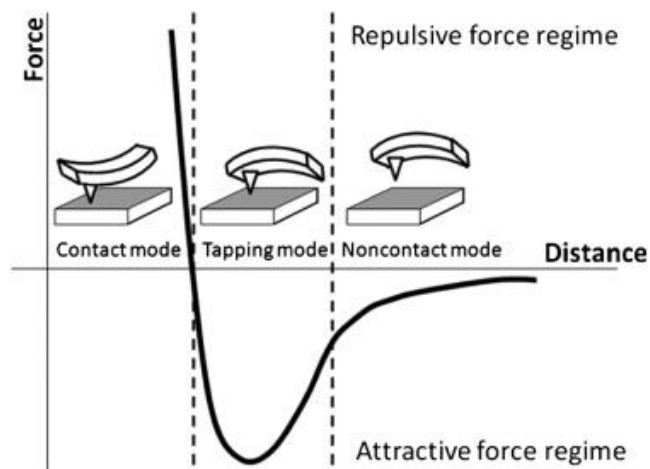

Figure 22 – Graphical presentation of force-distance interaction: the X-axis shows the distance between the probe and the specimen surface; the Y-axis of the curve presents the interatomic force operating between the probe and the specimen surface

The contact mode regulates in the renouncing area of the curve, contactless regime acting in the non-repulsive region, while between these two tapping regimes or the intermittent fluctuates is localized.

AFM measurements were performed at SPIN-CNR of Naples in collaboration with Dr. Roberto Di Capua by means of XE100 Park instrument operating in noncontact mode (amplitude modulation, silicon nitride cantilever from Nanosensor) at room temperature and in ambient conditions. Samples for AFM imaging were prepared by drop-casting sample suspensions onto freshly cleaved mica substrates (grade V-1, Electron Microscopy Sciences) which were then allowed drying up in air.

2.3.8 X-Ray Diffraction

X-ray diffraction (XRD) is a high-speed analytical method basically applied for investigation of solid materials. This technique provides information on phases, texture, structures, preferred crystal orientations. Also it gives more detailed information concerning other structural parameters, such as strain, average grain size, crystallinity and crystal defects. Constructive interference of a monochromatic beam of X-rays distracted at determined angles from each side of lattice in a specimen generated by X-ray diffraction peaks. The atomic positions in the lattice planes of studied sample assign the peak intensities.

In a cathode ray tube, electrons are generated by heating a filament, applying voltage to accelerate and bombard the target material with subsequent X-rays formation. The most common target material is a copper which is used for single-crystal diffraction with CuKα radiation $\lambda = 1.5418$ Å. Generated X-rays are directed onto the previously collimated specimen. While the specimen and detector are turned around, the intensity of the reflected X-rays is registered. A peak in intensity obtained by occurs of constructive interference, which can be reached when the geometry of the incident X-rays crashing the specimen satisfies the Bragg's:

$$n\lambda = 2d \times \sin\theta \qquad (5)$$

where is: n - a positive integer;

λ is the wavelength of the X-ray beam;

d - the distance between the crystal planes;

θ - the angle between the incident X-rays and the planes of parallel crystal.

A detector registers and works up this X-ray signal and transforms the signal to a count rate which is then lead out to a device (printer or computer monitor).

X-ray powder diffraction is most widespread for the authentication of unknown crystalline materials, such as minerals, inorganic compounds etc. The general possibilities of this technique include: optically determination of unit cell measurement and dimensions of specimen purity; specification of crystalline materials; authentication of fine-grained minerals such as clays and mixed layer clays, which difficult to determine.

Thus, XRD helps in less than 20 minutes to get an analysis of unknown mineral with minimal sample preparation. This method provides an unambiguous mineral determination in the majority. Interpretation of received results is relatively straight forward.

Figure 23 represent basic scheme of X-ray diffractometer. The geometry of an XRD is such that the specimen revolves in the path of the collimated X-ray beam at an θ angle while the X-ray detector is mounted on an arm to compile the diffracted X-rays and turn around at an angle of 2θ. The instrument applied to maintain the angle and turn around the specimen is called a goniometer. Data is collected at 2θ from ~5°-70° angles for typical powder patterns, that are set in the X-ray scan.
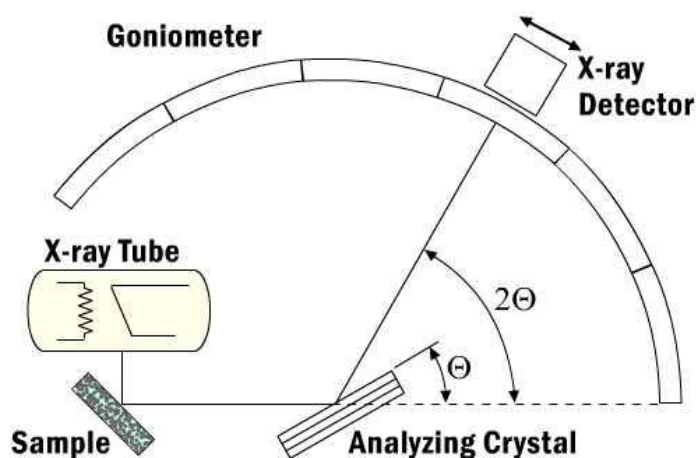

Figure 23 – X-ray diffractometer basic scheme

XRD analysis of the samples in the framework of dissertation were carried out on a Philips PW1710 diffractometer operating in the 5-60°2Θ range with a CuKα radiation ($\lambda = 1.54056$).

2.4 Method of CO_2 capture tests on fixed-bed microreactor

CO_2 adsorption tests under dynamic conditions were performed at IRC-CNR of Naples in collaboration with Dr. Paola Ammendola and Dr. Federica Raganati. Adsorption tests were performed at atmospheric pressure and room temperature in a laboratory scale fixed bed Pyrex micro-reactor with inner diameter 10 mm and length 6.0 cm of column. A scheme of the facility is reported in Figure 24 [148].

The gas feed is prepared using separate two cylinders: of N_2 (99.995%) *1* and CO_2 (99.995%) *2* gases, and mass flow controllers *3,4* (Brooks) were used to set the flow rates. The gases were mixed before injecting to the laboratory scale fixed bed Pyrex micro-reactor. Concentration of the CO_2 in the inlet and outlet gas flows was calculated by an online working infrared gas analyzer *5* (ABB, AdvanceOptima2020) [148, 149].

In a typical experiment, the 0.5 g of sorbent, pelletized to particle size in range 180-400 μm, is put on the substrate of the reactor's column *6*, then, the mixture of

CO_2/N_2 gases (15 Nl/h) at a constant 3% vol. concentration of CO_2 is fed through the substrate with sorbent from the top of the reactor. The CO_2 concentration of entering gas to the column is permanently monitored as a function of time (breakthrough curve) until complete equilibrium (equal value) of gases at the inlet and outlet of the column achieved, i.e., until bed (sorbent on the substrate) saturation is reached. CO_2 concentration profiles were received as a time function, which has been calculated from the time the gas mixture takes to stream from the static bed to the infrared gas analyzer. This transit time (about 50 s) has been preliminary separately counted for each gas streams rate by running the CO_2/N_2 gas mixture through the empty bed.

The breakthrough curves have been developed for estimating:

1) m_{ads} – is the mass of carbon dioxide adsorbed by mass unity of used adsorbent, culculated by inserting the breakthrough curves;

2) t_b – is the breakpoint or the breakthrough time. The time it takes for CO_2 to achieve of the 5% vol. inlet concentration of gas at the adsorption column outlet.
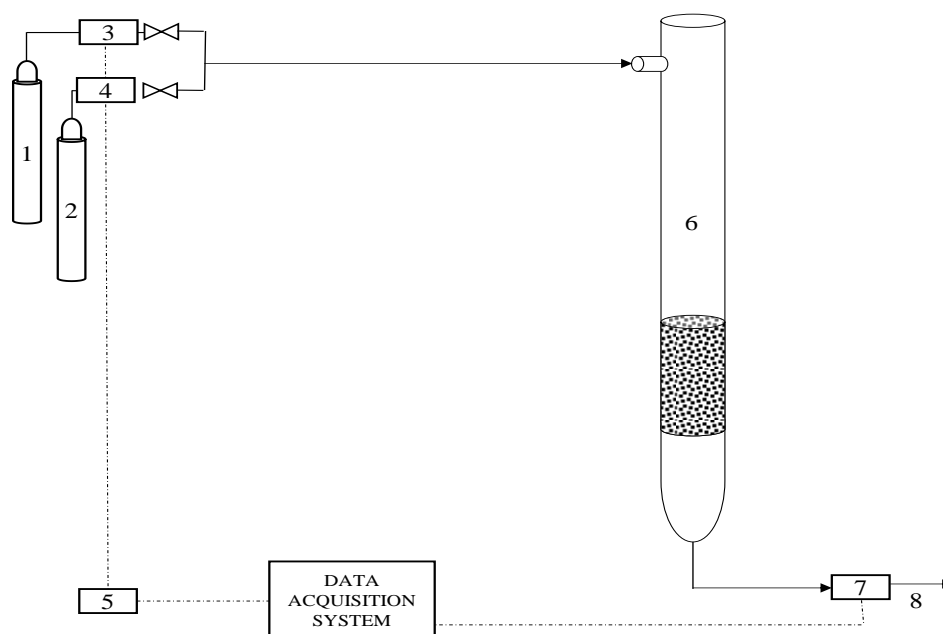
1 – cylinder with N_2; 2 – cylinder with CO_2; 3 – N_2 flow measurer; 4 – CO_2 flow measurer; 5 – multichannel control instrument; 6 –fixed bed reactor with 10 mm inner diameter column; 7 – CO_2 analyzer; 8) stack

Figure 24 – Details of the experimental apparatus – laboratory scale fixed bed Pyrex micro-reactor

The sorbents were tested 3-4 times using new re-prepared samples. Each tested sorbent underwent a regeneration process in a muffle furnace at 250 °C, and after regeneration, the absorption process was carried out additionally 2 times. Taking into account the deviation of the micro-reactor, the measurements error beetween 3-5%.

3 RESULTS AND DISCUSSION

3.1 Characterization of carbon-based nanocomposite materials for CO$_2$ adsorption

3.1.1 Study of rice husk carbonization process

The average composition of rice husk (RH) consists of 50% holocellulose, 25-30% lignin and 15-20% ash. The RH is a lignocellulosic biomass which is very rich in inorganic matter and SiO$_2$ is the most abundant component (around 92 to 95 wt.%). This aspect needs to be taken into account when advanced materials are produced starting from it [150].

The presence of a very high content of ashes was verified by both a thermogravimetric analysis (TGA, Figure 25) in an oxidative atmosphere (air) and by proximate analysis according to the ASTM D1762-84 procedure (TGA 701 LECO thermogravimetric analyzer, Table 11) [151] in the feedstock used during this Thesis for preparation of carbonized rice husk (cRH).

a   b
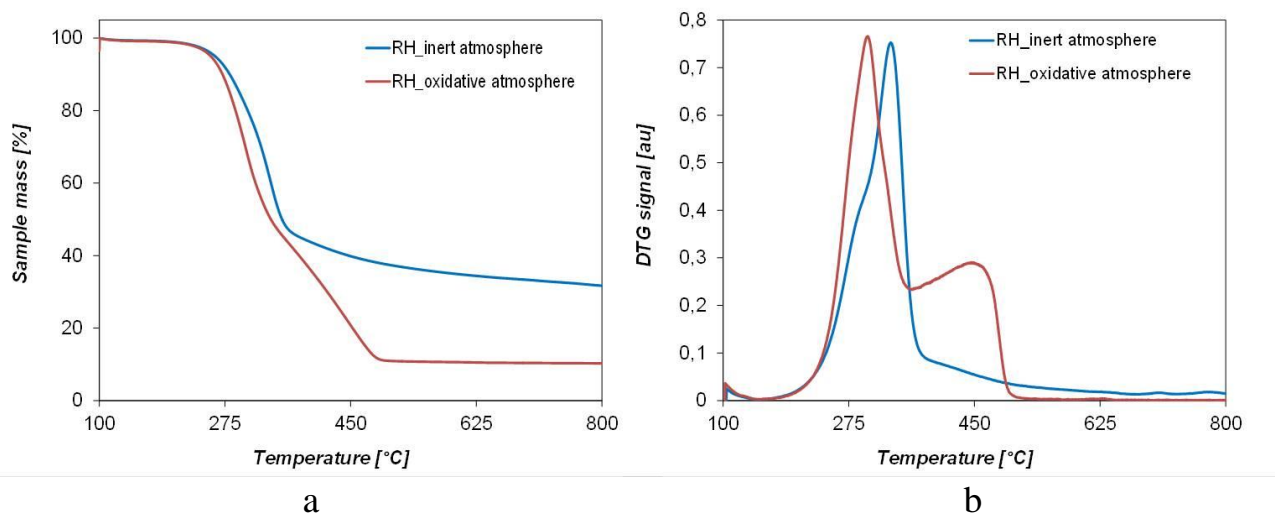
a – analysis at inert atmosphere (N$_2$, 40 ml/min, 10°C/min); b – analysis at oxidative atmosphere (air, 40 ml/min, 10°C/min)

Figure 25 – TGA of raw rice husk

Table 11 – Proximate analysis of RH and cRH

Sample	Moisture, wt.%	Volatiles, wt. %	Fixed carbon, wt.%	Ashes, wt.%
RH	7.69	57.84	18.57	15.9
cRH	5.56	8.18	47.60	38.65

The ashes content evaluated by proximate analysis (15.9 wt.%) is higher than the one evaluated as a residue after TGA in air at 800 °C (10.3 wt.%). Such difference perhaps can be referred to the establishment of two different temperature programs and different samples amount used during the thermogravimetric analysis, the latter reflecting the sample heterogeneity.

TG analysis in inert atmosphere (Figure 25, a) allows predict the behavior of RH under carbonization conditions and gives a clear idea of the carbonized material yield expected at the working temperature (31.5 wt.% of the starting material). RH carbonization process induces the reduction of volatile content and thus an increase of both fixed carbon and ashes (Table 11). The presence of a high content of SiO_2 in the carbonized product was probed by both ICP-MS and SEM-EDAX analyses (Figure 26) [152]. According to energy dispersive spectroscopy data leading contents of three elements were detected: carbon, oxygen and silicon, respectively 66.09%, 19.18% and 13.36%. Elemental XRD analysis confirms amorphous structure of cRH due to the broad peak at 2θ angle of 46∘ (supporting information in appendix). According to experimental XRD analysis results of cRH not detected well defined peaks. A hump is observed in the 2θ ranging 46°, indicating disordered structure, also it seems that XRD is mainly due to amorphous silica particles. As the atomic scattering factor for carbon is very small, intervening carbon atoms seem to contribute very little with respect to scattering from silica
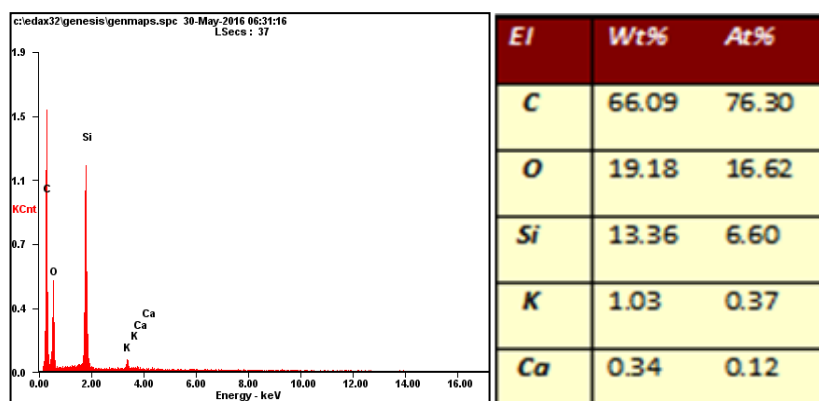

Figure 26 – EDAX analysis of cRH

The contents of carbon, hydrogen and other elements (nitrogen, oxygen and metals) of the starting feedstock and the carbonized rice husk, evaluated by ultimate analysis are reported in Table 12.

Table 12 – Samples composition in terms of carbon, hydrogen and other elements (including nitrogen, oxygen and metals) contents and ashes

Sample	C wt.%	H wt.%	Others wt.%	Ashes wt. %
RH	34.9	5.09	60.0	22.3
cRH	44.5	1.1	54.4	46.1

The amount of ashes evaluated by combustion in pure oxygen at 800°C is also reported (supporting TGA). As expected, after the carbonization process, the carbon content is increased while the hydrogen content decreases. The carbonization of cRH does not significantly alter the morphology of the starting feedstock as demonstrated by SEM images reported in Figure 27.
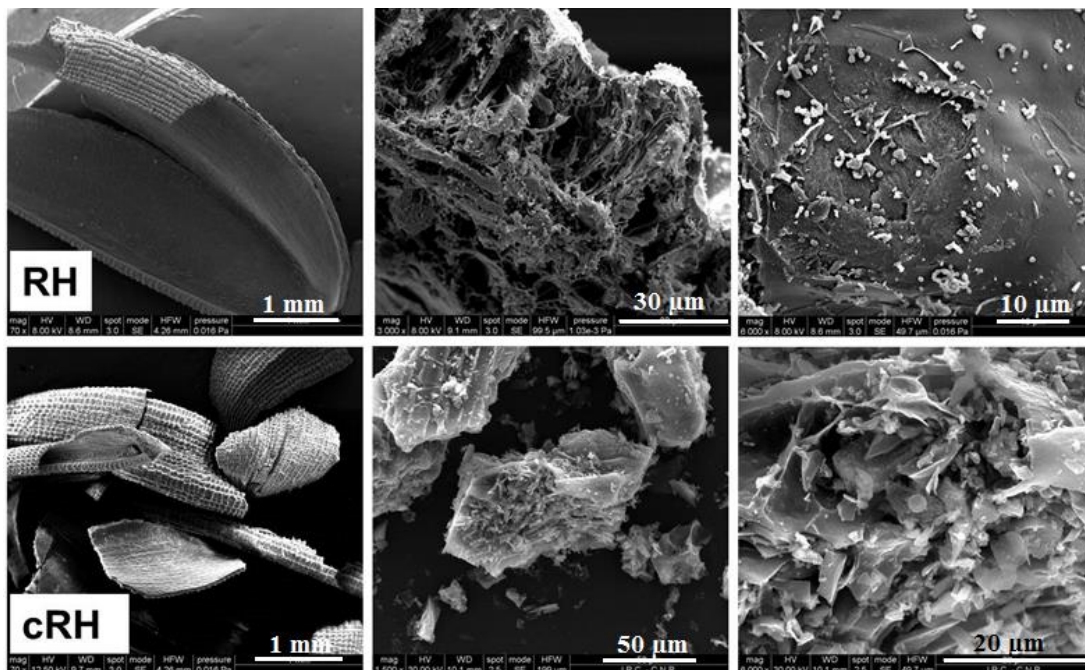

Figure 27 – SEM images of RH and cRH

As we can see from Figure 27, even though the internal structure of RH was rearranged due to high carbonization temperature, the SEM images showed that the cRH keeps the pristine RH porous structures with macropores and mesopores of different shapes (round or oval) arranged in an orderly fashion. Overall, cRH particles appear to be composed by plate walls containing channels and pores of various sizes making the structures aspect fragile. The channels are supposed to emerge upon the removal of cellulose during carbonization while the presence of pores is explained by the volatiles escaping from the surface as a result of quick thermal degradation [153]. Cracks and shrinkages are also observed on the surface of the carbonized material. The structures seemed to be fragile because of their thin walls.

3.1.2 Investigation of alkali-treated carbonized rice husk

In this section the production of cRH-derived sorbents will be investigated paying attention to: 1) the effect of different concentrated alkaline solutions (NH_4OH and NaOH); 2) the effect of the reaction time; 3) the effect of cRH starting amount.

The first set of sorbents for CO_2 capture tests was prepared by treating the cRH with concentrated alkaline solutions (NH_4OH and NaOH) [154].

In the experimental part a lower yield of samples treated by NaOH is indicated which associated possible effect to cRH by applying strong alkali. Figure 28 represents EDAX analysis data of alkali treated samples. Reduced content of Si from 13.36 %

(pure cRH) to 4.49 % in cRH-NH$_4$OH is detected. Also this decreasing of Si to 2.05 % is detected in cRH-NaOH sample. Influence of treatments led to increase in content of C which contributed to decreasing of samples yield.

```
Element    Wt %     At %           Element    Wt %     At %
   C K    81.48    87.07              C K    87.44    91.66
   O K    13.19    10.58              O K     8.29     6.52
   MgK     0.25     0.13              NaK     0.82     0.45
   SiK     4.49     2.05              MgK     0.35     0.18
   K K     0.05     0.02              SiK     2.05     0.92
   CaK     0.28     0.09              CaK     0.44     0.14
   FeK     0.13     0.03              FeK     0.27     0.06
   CuK     0.12     0.02              CuK     0.34     0.07
 Total   100.00   100.00           Total   100.00   100.00
```

a   b

a – cRH-NH$_4$OH; b – cRH-NaOH

Figure 28 – EDAX analysis of selected samples

In Table 13, the contents of carbon, hydrogen and other elements (including nitrogen, oxygen and metals) of the samples obtained after the treatment of cRH with alkali solutions are reported (supporting EA and TGA). For some samples also the amounts of ashes evaluated by combustion in pure oxygen at 800°C are reported.

Table 13 – Samples composition in terms of carbon, hydrogen and other elements (including nitrogen, oxygen and metals) contents

Sample	C wt.%	H wt.%	Others wt.%	Ashes wt. %
cRH	44.5	1.1	54.4	46.1
cRH-NH$_4$OH (1 g, 1h)	51.7	0.7	47.5	n.d.[*]
cRH-NH$_4$OH (5 g, 1h)	47.3	0.8	51.9	n.d.
cRH-NH$_4$OH (10 g, 1h)	45.7	0.5	53.9	n.d.
cRH-NH$_4$OH (10 g, 4h)	47.0	0.8	52.2	n.d.
cRH-NH$_4$OH (10 g, 6h)	47.0	1.0	52.0	43.2
cRH-NaOH (1 g, 2h)	80.1	0.9	19.0	n.d.
cRH-NaOH (5 g, 2h)	76.6	1.2	22.2	n.d.
cRH-NaOH (10 g, 2h)	80.3	1.1	18.6	10.0
[*] n.d. - not determined				

The treatment of cRH with alkali solutions in one case (cRH-NaOH) corresponds to a strong decrease of the ash content and to a considerable increment of the carbon content, in other case (cRH-NH$_4$OH) only a slight increase in the carbon content and a slight decrease in the ash content are detected. These results can be interpreted in light

of the chemistry of silica particles: strong alkali (NaOH) favored silica dissolution since higher pH values are reached. This aspect also justifies the different yields of cRH-NaOH and cRH-NH$_4$OH samples (below 60 % and around 90 %, respectively, see to Figure 9, Ch. 2).

The effect of the reaction time on the yields and on the materials composition is quite negligible, while the effect of cRH starting amount needs some considerations. The use of a little amount of cRH (1g) allows obtaining a high-purity material (higher carbon content and lower content of other elements, Table 13), but in view of a possible scale-up of the treatment process the use of a so little amount is not economically advantageous. On the other side, the materials obtained with 5 or 10 g exhibit an adequate purity for the scope of this work and will be hereinafter considered for further manipulations. For sake of clarity and since the results are comparable, only the characterization data of cRH-NH$_4$OH (10 g, 1h) and cRH-NaOH (10 g, 2h) will be reported in the following, as representative of the corresponding cRH-NH$_4$OH and cRH-NaOH series.

The treatment of cRH with both alkali solutions and in all the investigated experimental conditions does not modify the morphology of the cRH, as demonstrated by SEM images reported in Figure 29.
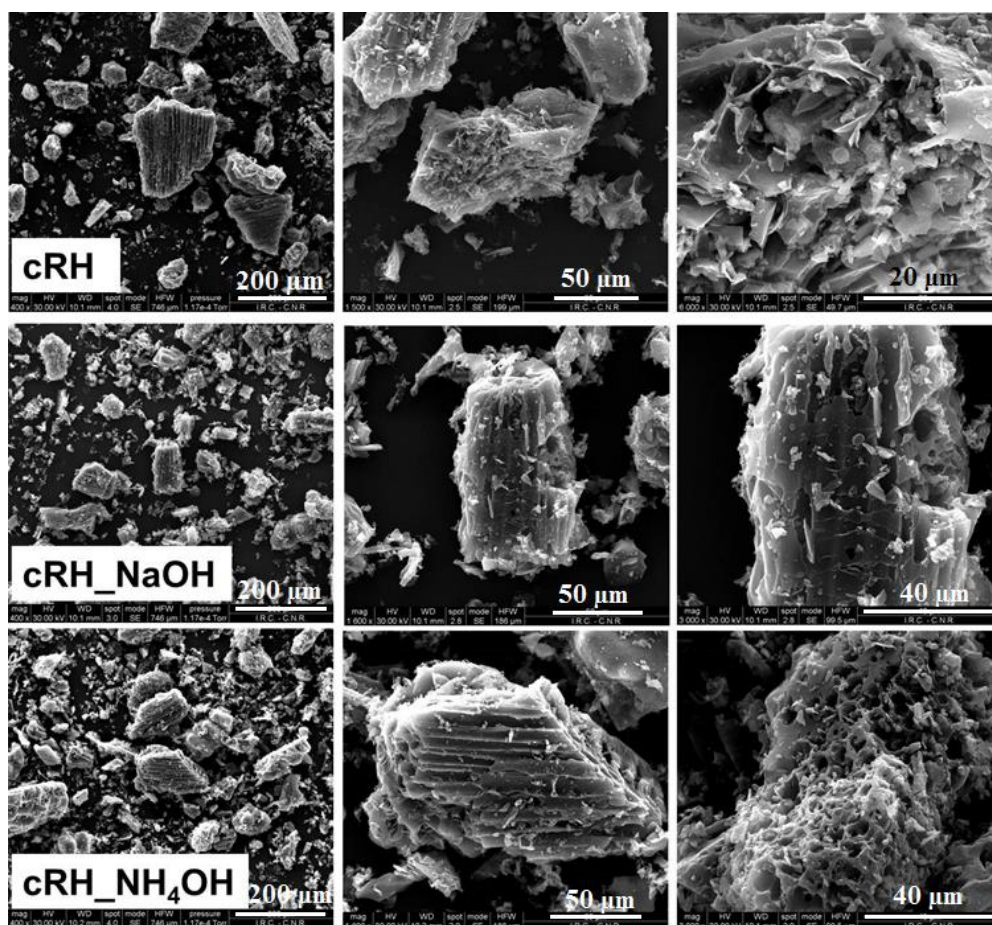

Figure 29 – SEM images of cRH, cRH-NH$_4$OH (10 g, 1h), cRH-NaOH (10 g, 2h)

The texture of cRH is preserved after both treatments (for sake of simplicity, only two experimental conditions have been shown).

The textural characteristics of cRH, cRH-NaOH and cRH-NH$_4$OH were evaluated from Ar adsorption isotherms at 87 K (Figure 30). The shape of isotherms of three samples is different indicating a different porosity. cRH and cRH-NH$_4$OH displayed type IV(a) isotherm (on the basis of IUPAC classification [155], with a marked adsorption at low pressure, indicating a well-developed microporosity along with a not negligible and well-developed mesoporosity, as testified by the high uptake at relative pressures above 0.5 and by the presence of marked hysteresis loops. Therefore, on the basis of Ar adsorption isotherms (Figure 4) cRH and cRH-NH$_4$OH can be classified as mesoporous materials. cRH-NaOH also displayed a type IV(a) isotherm with a marked adsorption at low relative pressures, indicating a well-developed microporosity along with the mesoporosity.

a   b
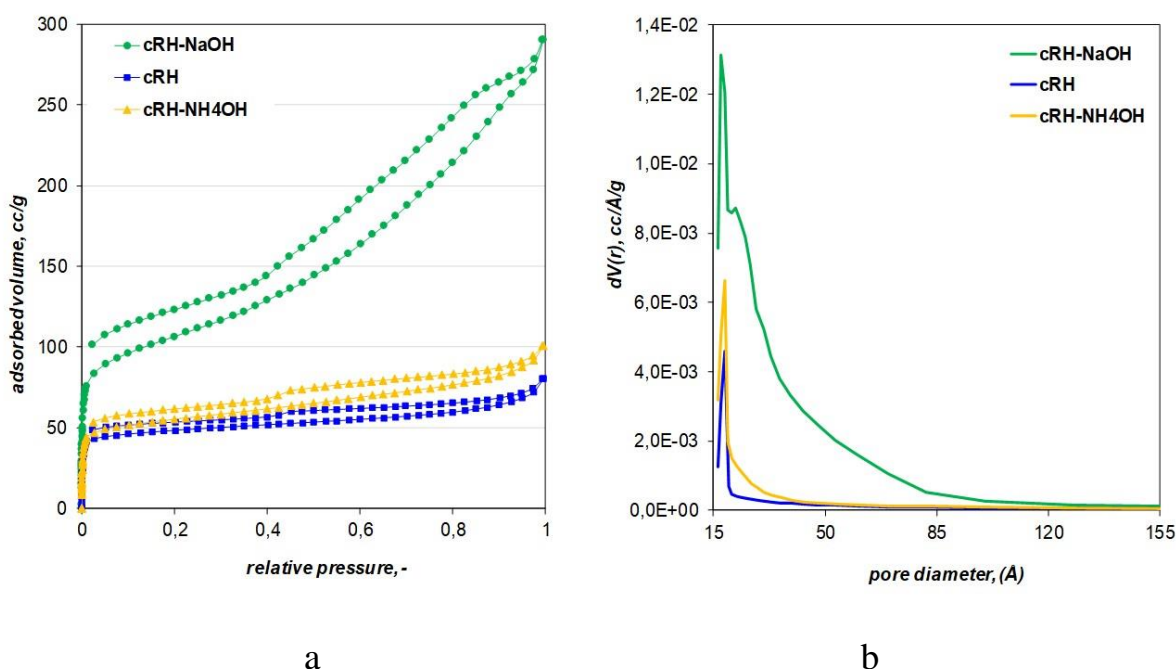
a – Ar adsorption isotherms at 87 K, b – pore size distributions

Figure 30 – BET data of cRH, cRH-NaOH and cRH-NH$_4$OH

The corresponding specific surface area values and pore volumes are reported in Table 14. cRH and cRH-NH$_4$OH are characterized by quite similar surface area values (162 and 180 m^2/g, respectively) while cRH-NaOH exhibits a higher value (431 m^2/g) indicating that the presence of ashes (typically non-porous matter) contributes to lower the surface area and should not be neglected (the surface area magnitude is expressed per gram of material).

An increase of the volumes of both mesopores and micropores (V_{tot} and V_{micro}) after both strong alkaline treatments is also detected, suggesting that the removal of silica particles turns clogged pores into accessible pores and no new porosity (in terms of pore dimension) was developed. In panel b of Figure 28 also the pore size

distributions, evaluated with the BJH model, are plotted. The three distribution appear quite similar: for all samples a main peak due to pores with a diameter of 18 Å is easily identified and a growing porosity is detected passing from cRH to cRH-NaOH.

Table 14 – Textural properties estimated for cRH, cRH-NaOH and cRH-NH$_4$OH

Sample	BET area m^2/g	V$_{tot}$(p/p^0=0.99) cm$^3_{liq}$/g	V$_{micro}$ cm^3/g
cRH	162	0.102	1.07E-02
cRH-NH$_4$OH	180	0.128	1.91E-02
cRH-NaOH	431	0.370	5.32E-02

The carbonaceous materials cRH, cRH-NaOH and cRH-NH$_4$OH were analyzed by infrared spectroscopy (ATR method). The spectra of cRH and cRH-derived carbons (Figure 31) contain broad peaks in the region between 1600 and 1000 cm^{-1} typical of complex carbon-based materials [156]. FTIR analysis, moreover, confirmed the removal of the silica particles by the strong alkaline treatment with NaOH since in the spectrum of cRH-NaOH the characteristic Si-O-Si stretching mode signal at 1100 cm^{-1} [157] is absent. On the contrary, the characteristic Si-O-Si peak is present in both the spectra of cRH and cRH-NH$_4$OH (Figure 29).
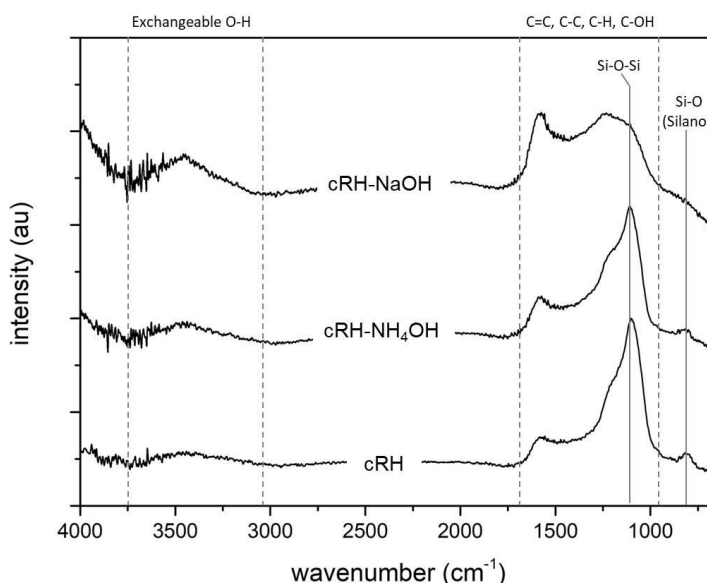

Figure 31 – ATR spectra of cRH, cRH-NaOH and cRH-NH$_4$OH

No significant variations have been detected in the FTIR spectra of the samples obtaining varying the time and the starting amount during the treatment with alkaline solutions.

The presence of silica and the amorphous character of the materials were also demonstrated by XRD investigation. The XRD patterns of cRH, cRH-NaOH and cRH-NH$_4$OH are contrasted in Figure 32.
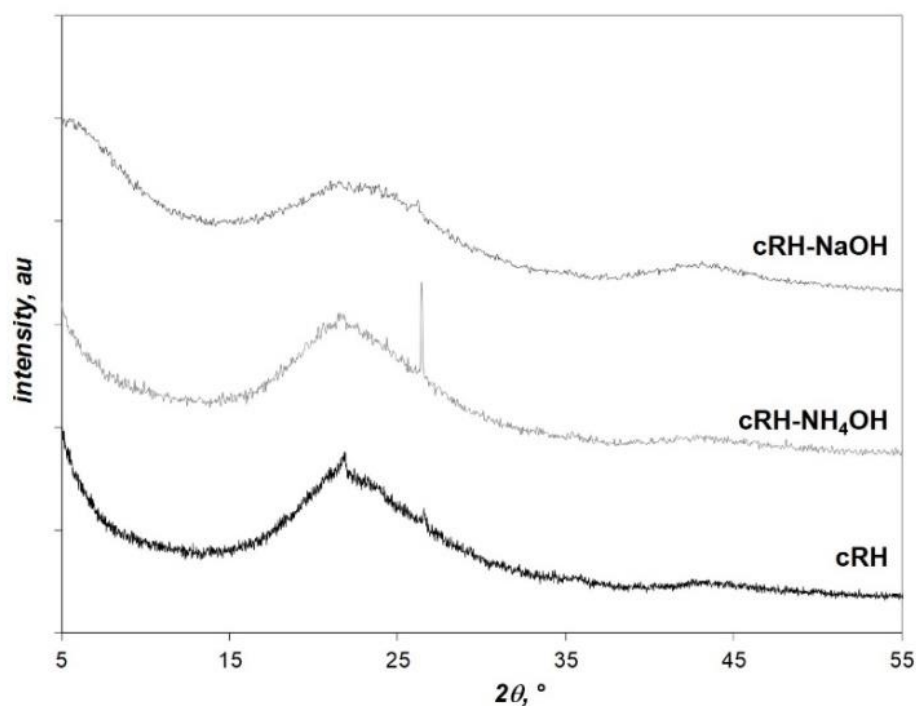
Figure 32 – XRD patterns of cRH, cRH-NaOH and cRH-NH₄OH

The thermal stability of cRH, cRH-NaOH and cRH-NH₄OH under oxidative conditions (air) was evaluated by TGA. TG profiles and corresponding DTG curves are shown in Figure 33.
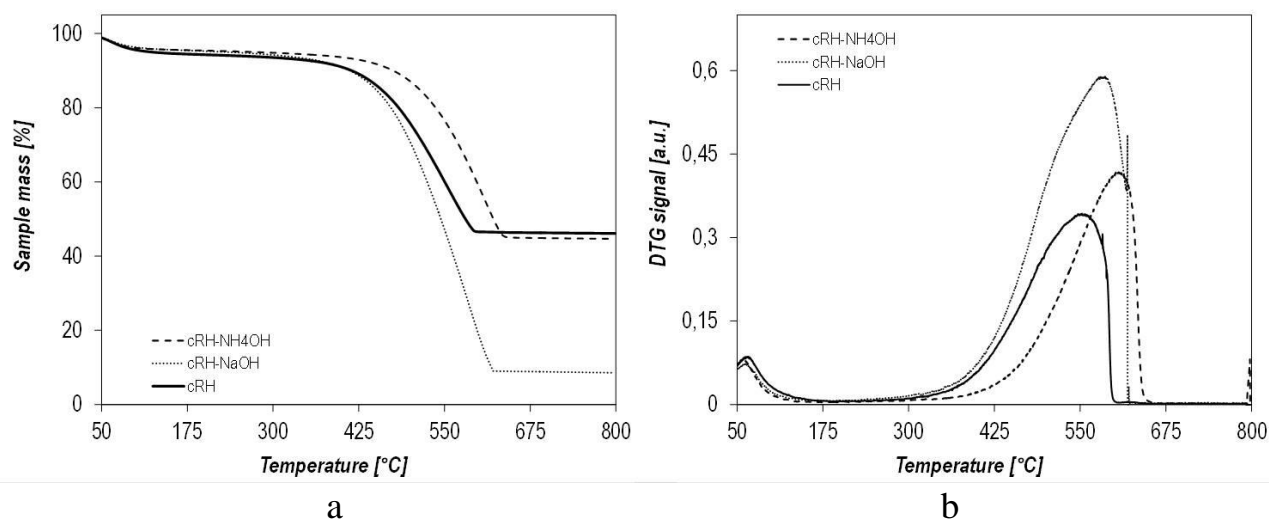

a   b

Figure 33 – TG profiles (a) and corresponding DTG curves (b) of cRH, cRH-NaOH and cRH-NH₄OH

All samples are stable up to 400 °C; after that temperature slow decrease of the sample mass occurs in all samples. As concerns the temperatures of burn-off, a great variability was detected: 550 °C for cRH, 580 for cRH-NaOH and 610 °C for cRH-

NH$_4$OH. The interpretation of such differences is not obvious and cannot be simply related to the difference in the content of ash with catalytic properties (cRH and cRH-NH$_4$OH have similar ash contents but behave differently). Probably the bulk properties are responsible for such differences more than the composition. The similarity in the final residue amounts for cRH (46.1 wt.%) and cRH-NH$_4$OH (44.7 wt.%) is in agreement with ultimate analysis results and mirrors the lower effect of NH$_4$OH on the dissolution of cRH ashes. As expected, the lower residue (8.6 wt.%) was detected for cRH-NaOH.

3.1.3 Characterization of carbonized rice husk-magnetite composites

Starting from the work of Alfe et al. [131] based on the production of carbon-ferric oxide composite materials cRH was coated with ferric oxide nanoparticles, a well-known active phase for CO$_2$. A series of seven sorbents was produced by varying the amount of cRH used as support and keeping constant amount of ferric oxide.

The yield of each hybrid material is lower with respect to simple sum of the amount of expected FM and the amount of cRH used in each synthesis (see to Table 8, Figure 10 Ch. 2). This discrepancy is explained by the result of the treatment of cRH with ammonia in absence of FM precursors (cRH-NH$_4$OH): the alkaline conditions cause the dissolution of a part of inorganic matter (mainly silica) present in cRH causing a reduction of the effective amount of cRH recovered at the end of the synthetic procedure.

Table 15 reports the compositions of the different samples belonging to the cRH-FM series as weight percentage contents of C, H, and other elements (others) including N, O. The compositions of raw cRH, FM and cRH-NH$_4$OH are also reported for comparative purposes. The content of Fe, determined by ICP-MS (Figure34), and the total amount of ashes determined after combustion in pure oxygen at 800 °C are reported for a selection of samples.
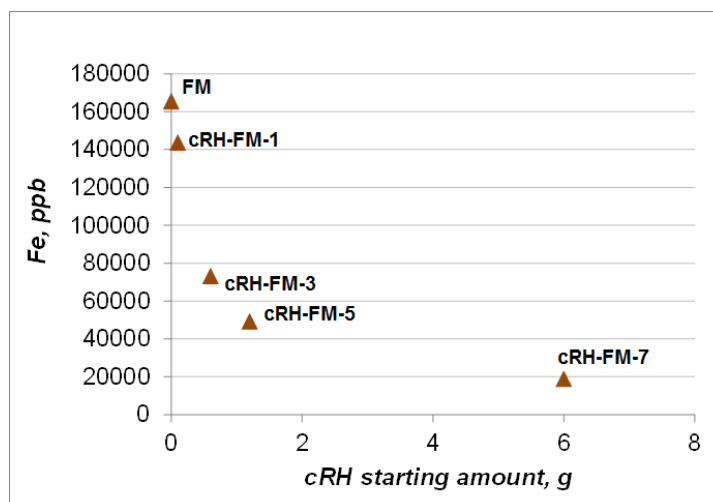

Figure 34 – ISP-MS data of magnetite FM and composites based on its cRH-FM-1, cRH-FM-3, cRH-FM-5, cRH-FM-7

Table 15 – Compositions of materials belonging to cRH-FM series

Sample	C (wt.%)	H (wt.%)	Others wt.%)	Fe (mg/g %)	Ash (wt.%)
cRH	44.5	1.1	54.3	n.d.[*]	46.1
FM	0.2	0.2	99.6	16.6	n.d
cRH-FM-1	7.5	0.4	92.1	14.4	n.d
cRH-FM-2	23.1	0.5	76.4	n.d	n.d
cRH-FM-3	29.2	0.7	70.2	7.32	n.d.
cRH-FM-4	32.5	0.5	67.0	n.d	60.0
cRH-FM-5	33.1	0.6	66.2	4.92	56.7
cRH-FM-6	40.5	0.2	59.3	n.d	52.0
cRH-FM-7	42.8	0.8	56.4	1.89	44.9
cRH-NH$_4$OH	47.0	0.8	52.2	n.d.	43.3
[*]n.d. - not determined					

The morphology of the samples has been investigated by SEM imaging. In Figure 35 the images of a selection of representative samples belonging to cRH-FM series are contrasted. The morphology of the starting feedstock is clearly discernable only in the investigated sample with the lower content of FM (cRH-FM-6). The typical smooth surface of FM is observed in the pure sample (FM), while agglomeration of big particles is imaged in other composites.
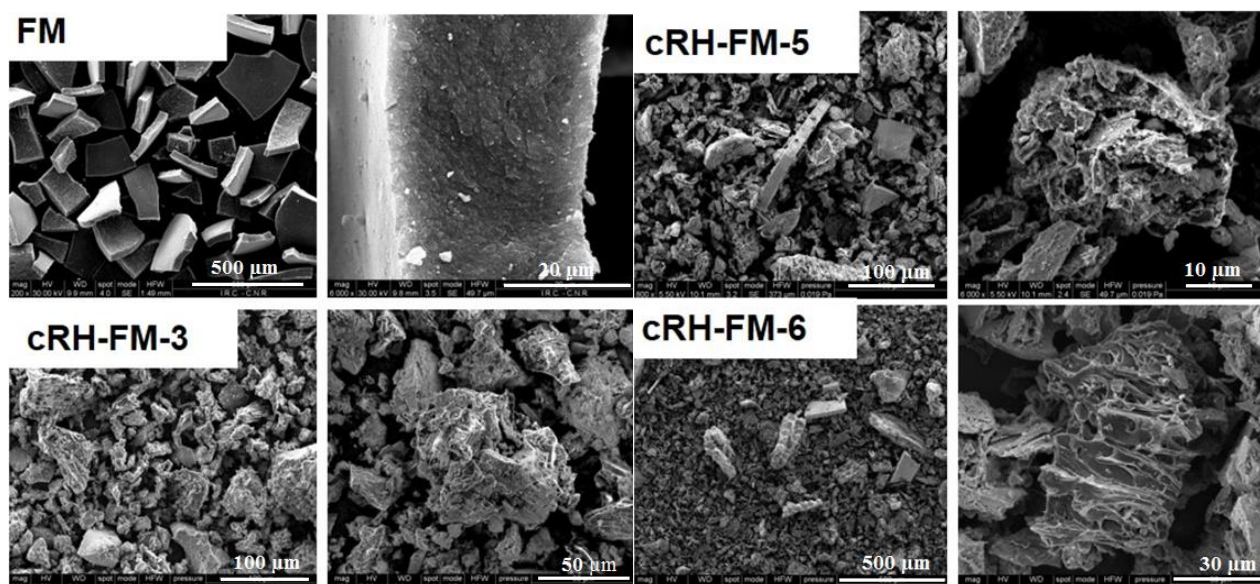

Figure 35 – SEM images of a selection of samples belonging to cRH-FM series

As expected, in accordance with synthetic procedure applied, the amount of carbon increases moving from cRH-FM-1 to cRH-FM-7, while the contents of total ashes and Fe decrease. Generally, the carbon content is always lower 50 wt.%.

Textural properties of a selection of samples of the cRH-FM were investigated performing Ar adsorption tests at 87 K. Isotherms are reported in Figure 36 together with pure FM, raw cRH and cRH-NH$_4$OH as a comparison. In all cases, the shape of isotherms resembles the typical isotherms of mesoporous materials. In case FM and two composites marked hysteresis loops and consistent Ar uptake at relative pressures above 0.5 are detected suggesting a very developed mesoporosity. The high argon uptake at very low relative pressures detected for cRH-FM-6 comparable to cRH and cRH-NH$_4$OH suggested non-negligible microporosity of the sample. It is worth of noting the similarity between isotherms of FM and the sorbent is richer in FM phase (cRH-FM-2) and the presence of features found in both components (the microporosity of cRH and marked hysteresis loop of FM) in the isotherm of cRH-FM-6. This aspect mirrors the compositions of two composites: cRH-FM-2 is richer in FM while cRH-FM-6 is richer in cRH.

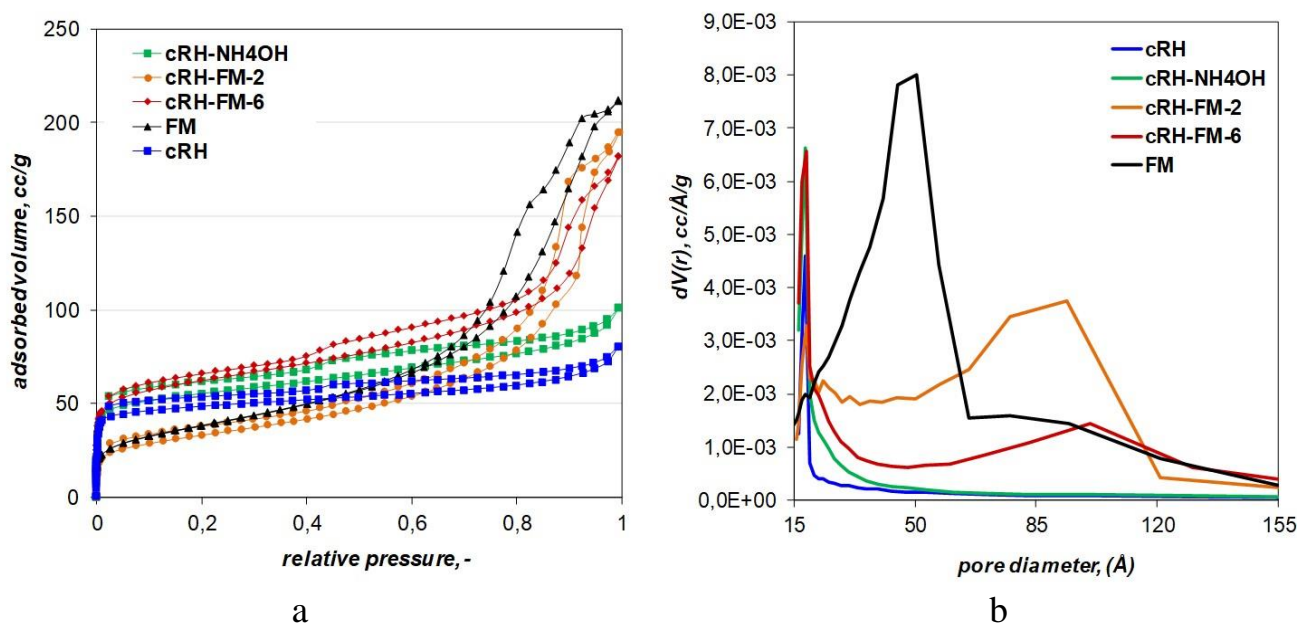a   b

Figure 36 – Ar adsorption isotherms at 87 K (a) and pore size distributions (b) of a selection of samples belonging to cRH-FM series

The adsorption data were worked out to calculate: 1) the specific surface area values through the BET equation; 2) total pore volume at p/p^0=0.99 and 3) pore size distribution through BJH model. The data collected is mentioned in Table 16 along with pure FM and cRH. The data of cRH-NH$_4$OH is also reported for comparative purposes. The Ar adsorption isotherms and the pore size distributions are plotted in Figure 36. All samples exhibited quite similar BET surface area values whereas some differences were detected for pore volumes. The presence of a larger amount of FM particles on the surface of cRH in cRH-FM-2 caused a not negligible drop of both surface area and pore volume compared to both cRH and cRH-NH$_4$OH since a

blockage of the pores of the carbonaceous support occurred. This circumstance is less pronounced in case with cRH-FM-6 where the particles of FM phase are dispersed over a large amount of cRH (acting as support) and blockage of the pores is limited. The presence of a not negligible porosity ascribable to the inorganic part (FM) is highlighted in the pore size distribution plot (PSD plot) (Figure 36, b) for both cRH-FM-2 and cRH-FM-6 (broad peak between 50-120 Å), even if the pore size distribution of FM is centered at 50 Å.

Table 16 – Textural properties estimated for a selection of samples of cRH-FM series

Sample	BET area m^2/g	V_{tot} (p/p^0=0.99) m^3_{liq}/g	V_{micro} cm^3/g
cRH	162	0.102	1.07E-02
cRH-NH$_4$OH	180	0.128	1.91E-02
cRH-FM-2	119	0.302	1.40E-02
cRH-FM-6	199	0.232	2.20E-02
FM	136	0.211	1.29E-02

FTIR is in transmission method in order to characterize their surface chemistry. The spectra of materials selection belonging to cRH-FM series are contrasted in Figure 37. The typical stretching signals of Fe-O bonds are located below 800 cm^{-1} and were easily detected in the FM spectrum as well as in the spectra of composites. The presence of signals around 580 cm^{-1} and 630 cm^{-1} typical of magnetite (Fe$_3$O$_4$) [131] indicates that the main phase produced is the desired (magnetite, Fe$_3$O$_4$) one and not maghemite ($\square$-Fe$_2$O$_3$) characterized by signals at 709, 693,640, and 563 cm^{-1} [158].
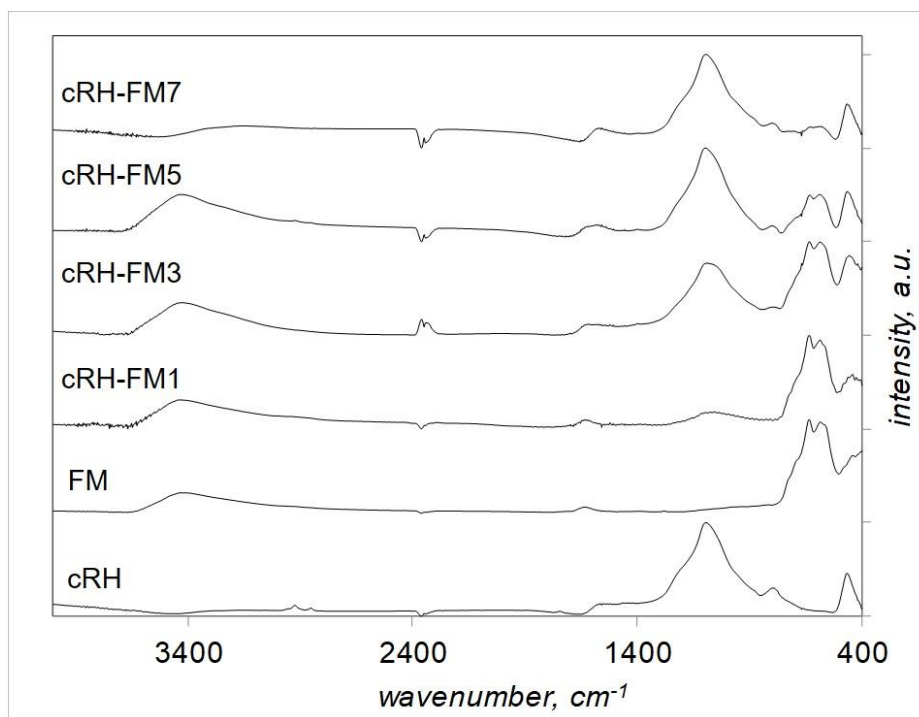

Figure 37 – FITR spectra of a selection of samples belonging to the cRH-FM series

It is worth of noting that moving from cRH-FM-1 up to cRH-FM-7, the peak ascribable to SiO_2 (1100 cm^{-1}) in cRH grows in intensity and the peaks ascribable to Fe_3O_4 phase decrease in intensity, in accordance with the composition of the materials analyzed. Peaks 3500 cm^{-1} occur due to O-H stretching signals pointed to water, 1600 cm^{-1} is the result of signals overlapping of carbonaceous network such as C=C, C-C, C-H bonds.

In order to confirm the presence of the desired ferric oxide form (magnetite, Fe_3O_4) in each sample, XRD measurements were also performed. The results of the diffractometric survey are reported in Figure 38, where the XRD patterns have been highly normalized and shifted on the vertical for clarity. The XRD pattern of FM is also reported for comparison.

The XRD FM pattern is in accordance with reported in literature for magnetite [159, 160] and the main features identified in its pattern are detected in all patterns of the materials included in cRH-FM series (Figure 38).
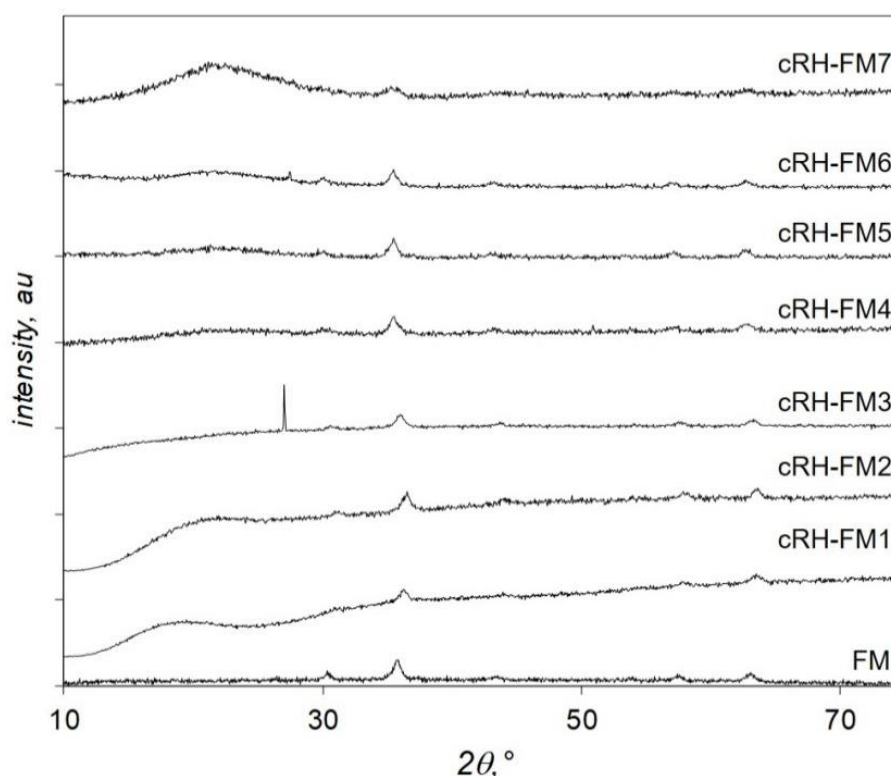

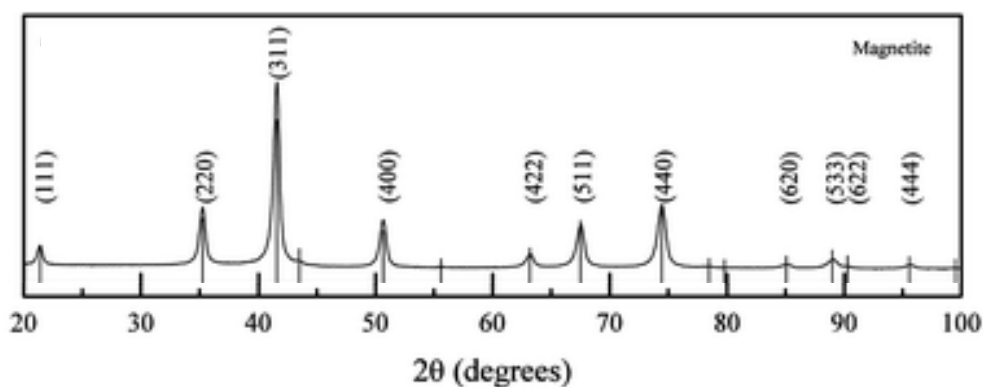Figure 38 – XRD patterns of nanocomposites
(cRH-FM series)

Figure 39 – Simulated FM pattern [160]

This result confirmed that the applied synthetic procedure ensures production of magnetite particles also in the presence of cRH as carbonaceous support. This result is also corroborated by the magnetic activity detected in each sample by simply locating a magnet close to each material.

The thermal stability of the samples of cRH-FM series under oxidative conditions (air) was evaluated by TGA. TG profiles and corresponding DTG curves are reported in Figure 40. The data of FM, cRH and cRH-NH$_4$OH is also reported for comparison purposes.

All samples are stable up to 400°C and the carbonaceous part is completely burned before 600°C. It is worth of noting that the burn -off temperature of the composites is higher compared to both cRH and cRH-NH$_4$OH. This result is quite interesting considering the catalytic properties of iron oxide and can be interpreted taking into account diffusive phenomena.

The final residue amount was expected on the basis of sorbents composition (ref. Table 15): the higher residue recovered for the sorbent is richer in FM (cRH-FM-1).
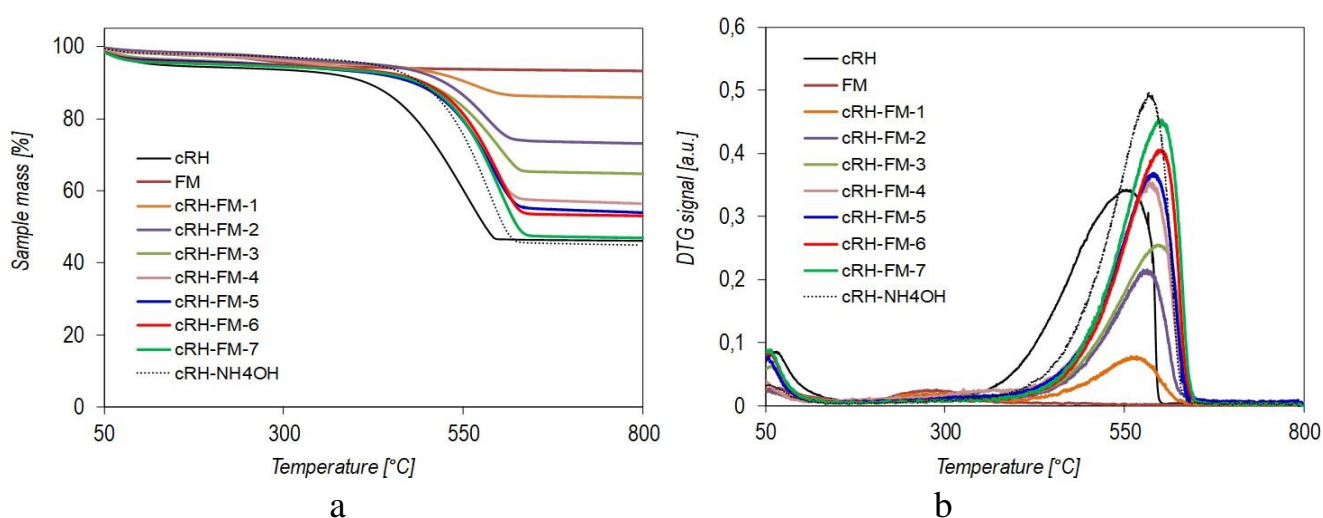

a   b

Figure 40 – TG profiles (a) and corresponding DTG curves (b) samples of cRH-FM series

3.1.4 Investigation of carbonized rice husk-nanoparticulate magnetite composites

Another set of carbon-ferric oxide composite materials was synthetized in strong alkaline conditions (NaOH) and in presence of a surfactant (see Figure 11, Ch. 2) with the aim of prevention of magnetite agglomeration and obtaining the coating of cRH with nanosized magnetite particles.

The synthesis was performed adapting the procedure of [139]. Five sorbents were produced by varying the starting amount of cRH (used as support for nFM phase) and keeping constant amounts of FM precursors (namely keeping constantly expected amount of FM in each composite) [161].

Table 17 reports the compositions of different samples belonging to cRH-nFM series as weight percentage contents of C, H and other elements (briefly referred to as "others") including N, O. The compositions of raw cRH, nFM and cRH-NaOH are also reported for comparison. The content of Fe determined by ICP-MS and total amount of ashes determined after combustion in pure oxygen at 800 °C are also reported for all composites.

Table 17 – Composition of materials belonging to cRH-nFM series

Sample	C (wt.%)	H (wt.%)	Others (wt.%)	Fe (mg/g %)	Ash (wt.%)
cRH	44.5	1.1	54.3	0.007	46.1
nFM	0.1	0.2	99.7	36.4	n.d.
cRH-nFM-a	4.6	0.4	95.0	62.5	88.1
cRH-nFM-b	12.8	0.5	86.7	43.7	78.0
cRH-nFM-c	46.1	1.1	52.8	23.8	56.4
cRH-nFM-d	50.3	1.4	48.4	12.5	41.4
cRH-nFM-e	68.6	0.9	30.5	9.46	28.4
cRH-NaOH	76.6	1.2	22.2	n.d.	9.90
n.d.: not determined					

In these composites the amount of nFM is very high (up to 90 % in cRH-nFM-a) and this explains very high ash contents and very low carbon contents for cRH-nFM-a and cRH-nFM-b. As expected, on the basis of the synthetic approach, the content of carbon is increased moving from cRH-FM-a to cRH-FM-e and Fe is descreased.

Comparing the compositional data of these series with cRH-FM, it is worth of noting how the content of carbon is higher than cRH-nFM series with respect to cRH-FM materials at comparable theoretical FM content (for example cRH-nFM-e vs cRH-FM-6). The higher carbon content for sorbents of cRH-nFM series is explained on the basis of the effect of the applied synthetic conditions: NaOH is used as reactant (in place of NH_4OH it is used for cRH-FM series) for the synthesis of cRH-nFM series which leads to higher pH and to quite complete dissolution of SiO_2 determining an overall reduction of the inorganic component (ashes) of cRH support.

Figure 41 presents ICP-MS results for carbonized rice husk modified by nanoparticulate magnetite. It was expected that the content of Fe in nanocomposites

shows a linear dependence of the loaded cRH. Value of points created in the Figure 41 presents in Table 17.
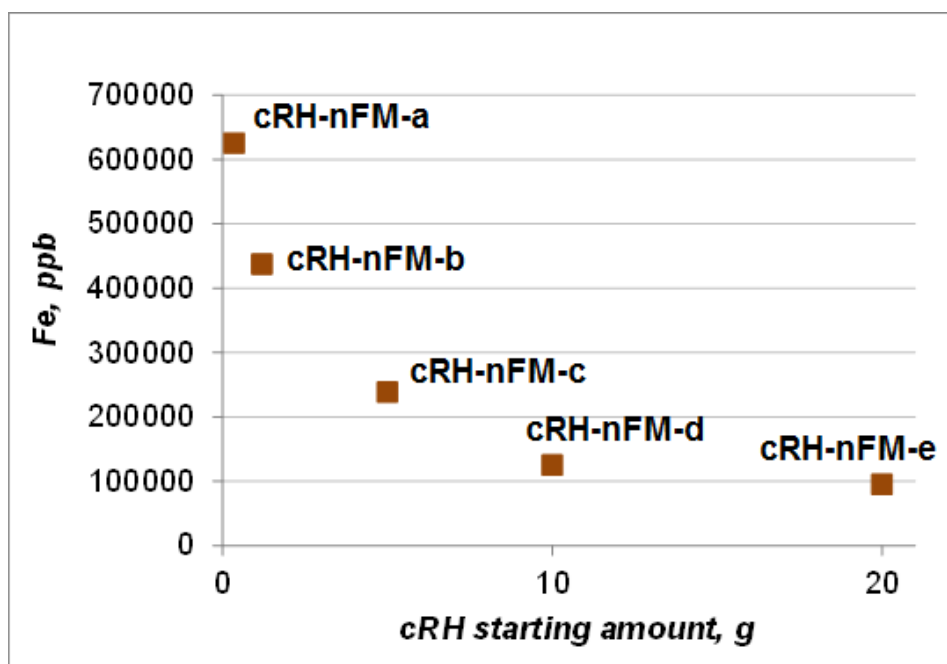

Figure 41 – ICP-MS analysis data of cRH-nFM series nanocomposites

The morphology of the samples was investigated by SEM imaging. In Figure 42 the images of a selection of samples belonging to cRH-nFM series is reported. The morphology of the starting feedstock is clear discernable only in the sample with the lower content of nFM (cRH-nFM-d). Nanoparticulate magnetite nFM at first sight present such morphology as FM samples, the difference is that the particles look smaller and have a variety of shapes. Composite materials based on cRH and nFM presented in 3000 magnification showed an inhomogeneous structure corresponding to sorbent materials. cRH-nFM-c and cRH-nFM-d display surface morphology more close to carbonized rice husk structure. It is impossible to distinguish the nanoparticles of the obtained magnetite, at the same time there is a prediction that the particles enter cRH pores during coprecipitation method.

The typical smooth surface of nFM is detected in the neat sample (nFM), while agglomerates with a smooth surface are found in the other cRH-nFM composites. Nanomposite materials based on cRH and nFM presented in Figure 42 showed an inhomogeneous structure corresponding to sorbent materials.

However, these composite materials of carbonized rice husk treated with tetramethylammonium hydrooxide are significantly distinguishable by the above-described composites based on cRH and simple magnetite fine particles.
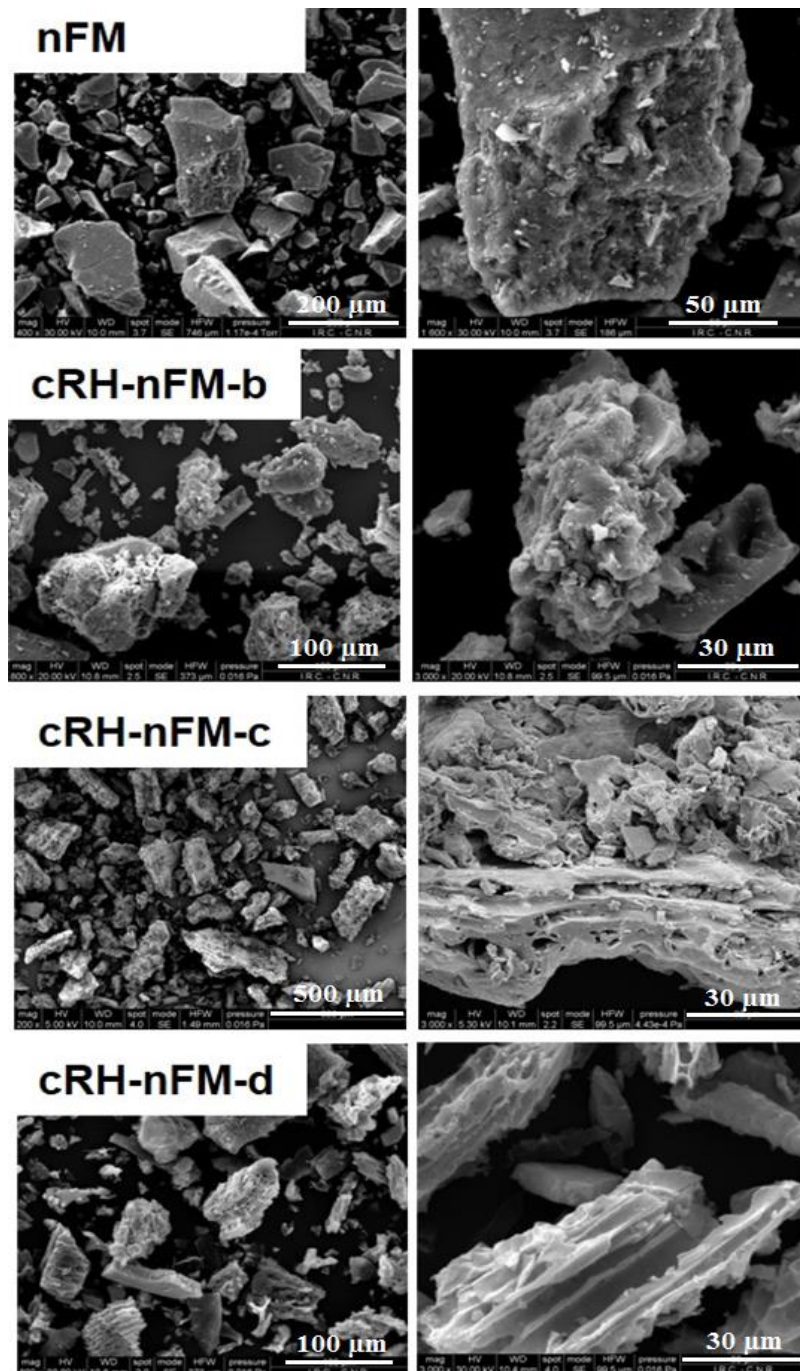
Figure 42 – SEM images of samples selection belonging to cRH-nFM series

To probe the nanosized character of the produced nFM, a more detailed microscopy survey was performed by both SEM and AFM (Figure 44) microscopies.

SEM images of nFM at different magnifications are reported in Figure 43: nanometric particles are clearly discernable even at low magnification degree allowed by SEM microscopy (24 000 magnification). In this way, image data represents the difference between nanoparticulate magnetite nFM and simple FM reported above.

Figure 43 – SEM images of nFM at different magnifications

Figure 44 – Morphological AFM images of nFM on mica substrate
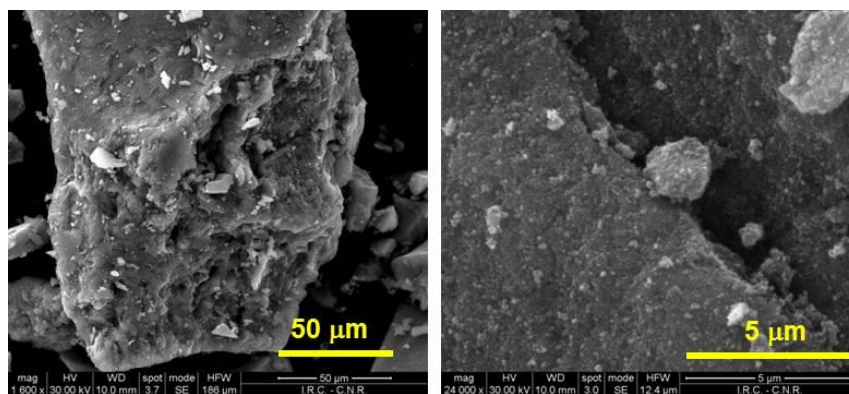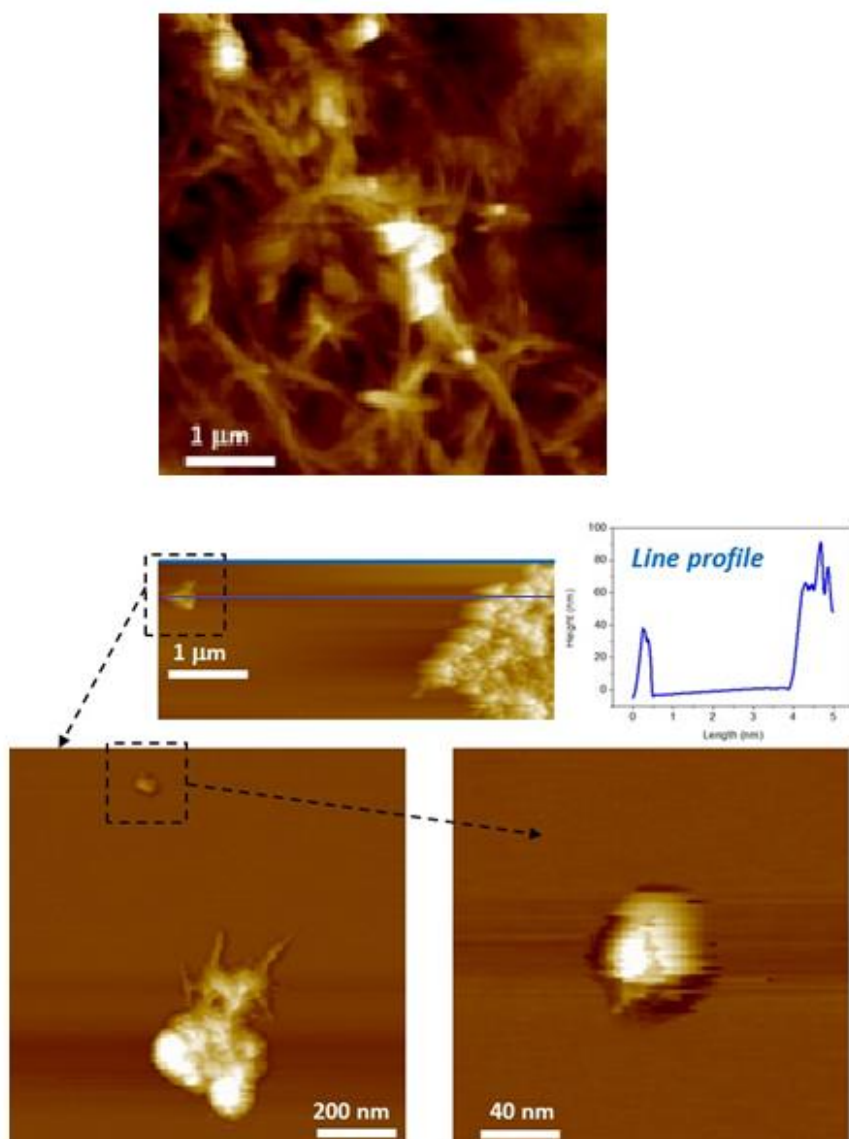
To obtain further structural information on nFM nanodispersion degree, AFM imaging (non-contact mode) were carried out on nFM. The nFM sample in aqueous

suspension was drop-cast deposited on atomically flat mica substrates. The images (Figure 44) show a well-developed structuration of the material at the nanometric level. A deeper analysis on isolated clusters shows that they have lateral dimensions (also in height) of the order of a few tens of nanometers (line profile panel, Figure 44).

The textural properties of samples selection of cRH-nFM series were investigated performing Ar adsorption tests at 87 K. The isotherms are reported in Figure 45 together with those of pure FM, raw cRH and cRH-NaOH for comparison. In all the cases the shape of the isotherms resembles that of a typical mesoporous material. nFM exhibits a Ar adsorption isotherm typical of mesoporous materials (IVa according to IUPAC classification) with a very low gas adsorption at low relative pressure values (below 0.1) and a high adsorption at relative pressure above 0.6. The marked hysteresis loop also confirms the mesoporous character of the materials.

a   b
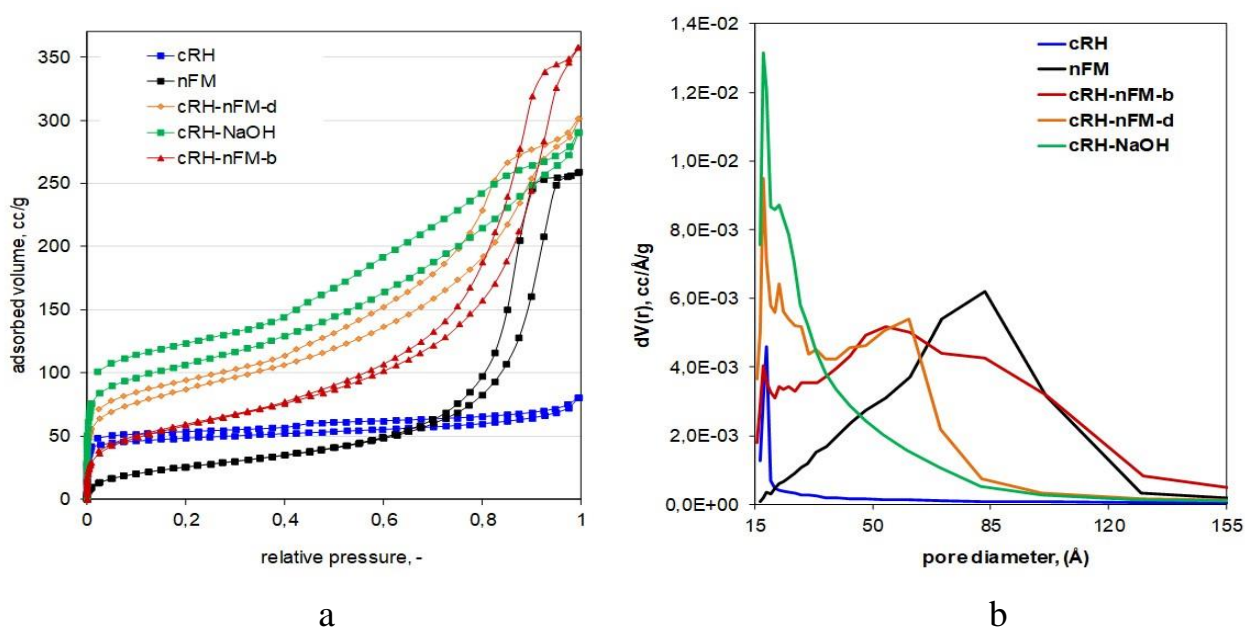
Figure 45 – Ar adsorption isotherms at 87 K (a) and pore size distribution (b) of samples selection belonging to cRH-nFM series

The material containing the highest amount of nFM (cRH-nFM-b) showed an isotherm is quite similar to nFM confirming that nFM characteristics prevail on the support, even if non-negligible microposity is expected on the basis of the gas uptake at lower relative pressure values.

When the content of iron oxide decreases (as in case of cRH-nFM-d), the similarity with nFM isotherm is less marked and the shape of the isotherm becomes more similar to that of the support (cRH). It is worth of note that the similarity is larger towards the isotherm of cRH-NaOH than that of cRH, confirming that the presence of NaOH in the reaction mixture favors the dissolution of inorganic matter that clogged the pores of pristine cRH. Overall, the analysis revealed a microporous character for both cRH-nFM-d and cRH-NaOH along a very well developed mesoporosity.

The specific surface area values calculated by means of BET equation, total pore volume at $p/p^0=0.99$ and pore size distribution determined by means of BJH model are reported in Table 18 along with pure nFM, raw cRH and cRH-NaOH for comparison.

Table 18 – Textural properties estimated for samples of cRH-nFM series selection

Sample	BET area m²/g	V_{tot} (p/p⁰=0.99) cm³$_{liq}$/g	V_{micro} cm³/g
cRH	162	0.102	1.07E-02
nFM	84	0.329	1.54E-03
cRH-nFM-b	190	0.455	1.92E-02
cRH-nFM-d	271	0.383	3.81E-02
cRH-NaOH	431	0.375	1.70E-02

The samples exhibited very different BET surface area and pore volume values highlighting a great variability of textural properties. nFM is characterized by a very low SA value (84 m²/g) and also by a low volume of micropores as expected on the basis of the isotherms. It can be concluded that high total pore volume is mostly due to mesopores as also suggested by PSD distribution peaked at 85 Å (Figure 45).

The values calculated for cRH-nFM-b suggested that the overall textural properties mirror the composition of the material (60 wt.% of nFM): the SA is larger than that of nFM but far from that of cRH-NaOH, the same trend is found for the volume of micropores. As concerns the total pore volume, cRH-nFM-b exhibits the highest value among the investigated materials. This result can be explained considering a well-developed mesoporosity as testified by both isotherm and PSD profile. It is worth of noting that the PSD curve resembled the sum of pure nFM and cRH-NaOH with a maximum centered at 70 Å.

Similar results are also found for cRH-nFM-d: in this material the presence of a higher amount of carbonaceous part is explained by higher amount of SA and micropores volume values compared to cRH-nFM-b. Drop in total pore volume can be explained by the mesoporosity reduction and by clogging of pores operated by nFM. Also, in case with cRH-nFM-d, PSD curves characterized by the combined features of both components are found (Figure 45).

In order to assess the presence of the desired ferric oxide form (magnetite, Fe_3O_4) in each sample, XRD measurements were performed for all samples. The results of the diffractometric survey are reported in Figure 46, where XRD patterns were highly normalized and shifted on the vertical for clarity. The XRD pattern of nFM is also reported for comparison.

Even if the intensity of signals is very low, the XRD pattern of iron oxide matches with the XRD pattern of magnetite (reported in Figure 36) and the presence of the desired ferric oxide form is confirmed in all samples.
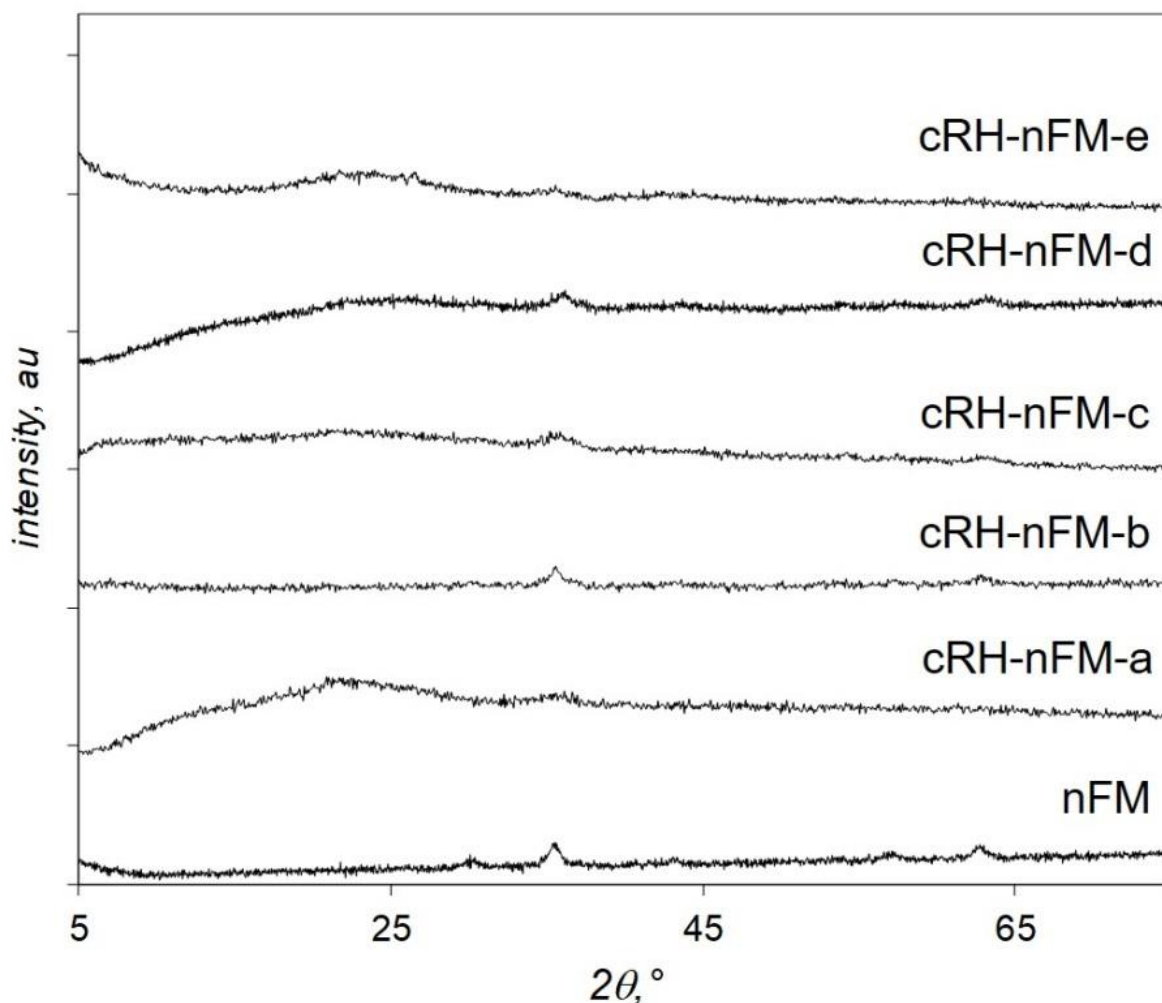
Figure 46 – XRD patterns of samples of cRH-nFM series

The thermal stability of samples under oxidative conditions (air) was probed by TGA. The TG profiles and corresponding DTG curves are reported in Figure 47. The data of FM, cRH and cRH-NaOH are also reported for comparison.

All investigated samples are stable up to 400 °C and the carbonaceous part is completely burned up to 600 °C. A great variability among temperatures of sample burn-off is detected: some composites (those composites with lower nFM contents) are burned off at a temperature lower than cRH-NaOH while other composites (those with higher nFM contents) are burned off at temperature comparable to cRH-NaOH. The presence of such behaviors could be as the result of combination of two effects: 1) diffusive phenomena and 2) catalytic effect due to iron oxide. In case with nFM -rich sorbent the diffusive phenomena prevail and the burn-off temperature is comparable to the support (cRH) while in the case with sorbents with lower nFM contents the catalytic action of iron oxide prevails causing a reduction of the burn-off temperature of the carbonaceous part [131].

As found for the cRH-FM series, the final residue amount is expected on the basis of sorbents composition: higher residue is found for sorbent which is richer in nFM (cRH-nFM-a).
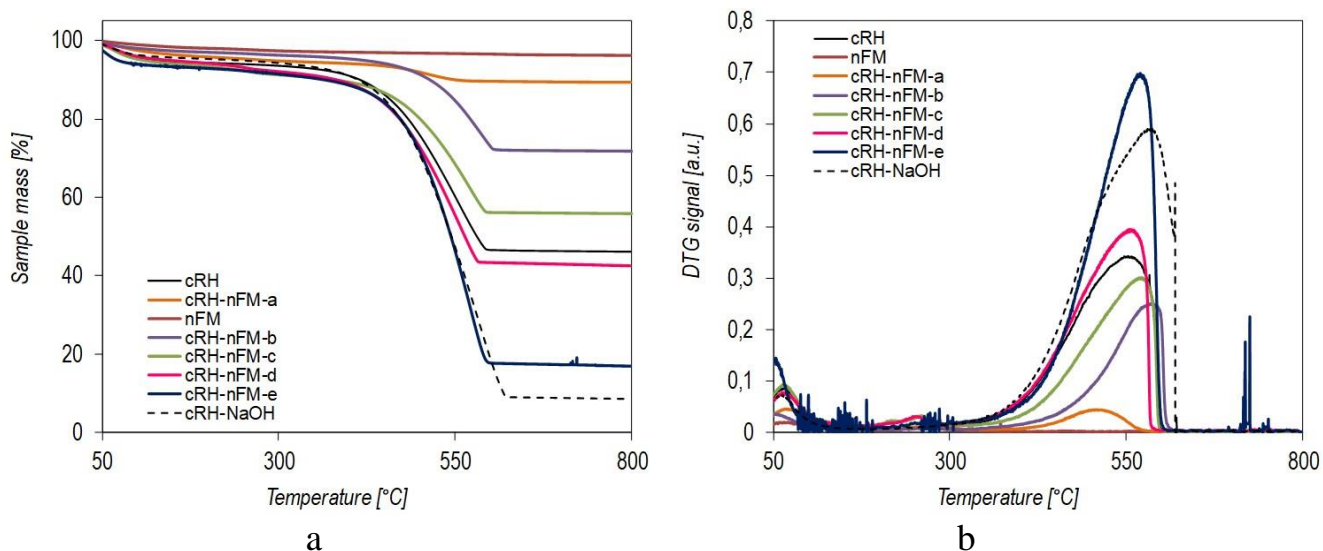
Figure 47 – TG profiles (a) and corresponding DTG curves (b) of samples of the cRH-nFM series

3.1.5 Characterization of composites based on carbon black-nanoparticulate magnetite

Carbon black used as a matrix for producing nanocomposites is a type of super resistant abrasion material with high reinforcement and tensile obtained by injecting liquid hydrocarbon feedstock into a stream of gases of fuel complete combustion. According to Alfe et al. [131] carbon black is monodispersive chain-like aggregates of spherical primary carbon particles, average diameters of 150-200 Å. Content of carbon in CB 110 type reached 99%, also uniform texture and interesting structural characteristics prompted the use of this affordable cheap effective carbon material as a matrix for composite materials in nanoscale and, in general, in solid state materials science.

In order to have a set of materials to be used as reference, composites using a nanostructured carbon black have been produced applying the same synthetic approach used for cRH-nFM series.

Since CB is a material with a very low content of inorganic matter (below 2 wt.%) the yields of the CB-nFM series composites are up to 100 % and the recovered amounts resemble the sum of the expected nFM quantity and the starting CB amount used in each synthesis (see to Table10, Ch. 2).

Table 19 reports the compositions of the different samples belonging to the CB-nFM series as weight percentage contents of C, H, and other elements (others) including N, O. The compositions of raw CB, nFM and CB-NaOH are also reported for comparison. For all the composites the content of Fe, determined by ICP-MS (Figure 49), and the total amount of ashes, determined after combustion in pure oxygen at 800 °C are also reported.

Table 19 – Compositions of the materials belonging to CB-nFM series

Samples	C (wt.%)	H (wt.%)	Others (wt.%)	Fe (mg/g %)	Ash (wt.%)
CB	98.9	0.5	0.6	n.d.[*]	1.40
nFM	0.1	0.2	99.7	36.4	n.d.
CB-nFM-a	9.9	0.0	90.1	33.0	76.8
CB-nFM-b	23.1	1.1	75.8	25.4	66.6
CB-nFM-c	57.9	0.3	41.8	15.7	38.4
CB-nFM-d	66.5	0.0	33.5	4.32	24.6
CB-nFM-e	81.4	0.0	18.6	6.03	14.9
CB-NaOH	96.9	0	3.1	n.d.	1.71
[*]n.d. - not determinied					

In agreement with the synthetic approach and with the compositions of the two components (nFM and CB), moving from CB-nFM-a to CB-nFM-e, as expected, the carbon content increases while that of iron decreases.

The morphology of a selection of samples was investigated by SEM imaging (Figure 50). Agglomerates with a smooth surface (typical of nFM) are found in all the composites and the morphology of the carbonaceous support is not clear discernable neither in the sample with the lower content of nFM (CB-nFM-d). Further nano structuration of the composites driven by the presence of nFM cannot be easily discernible given the low magnification degree here used (2000-3000x).

Magnified images of composite based on CB and nFM – CB-nFM-b, CB-nFM-c, CB-nFM-d, as can be seen from Figure 49, have mixed morphology different from components CB and nFM (see to Figure 39).
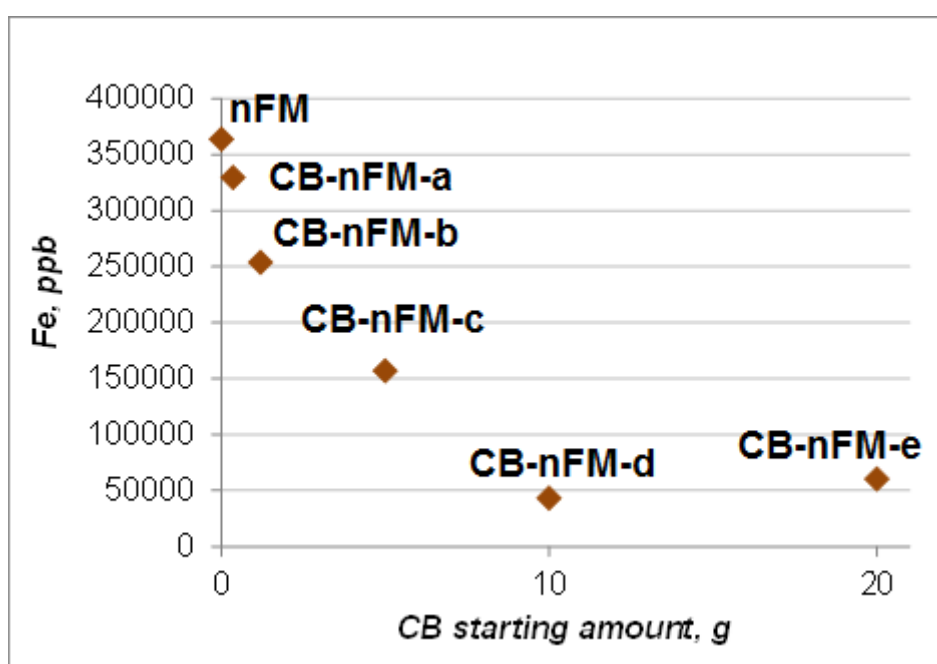

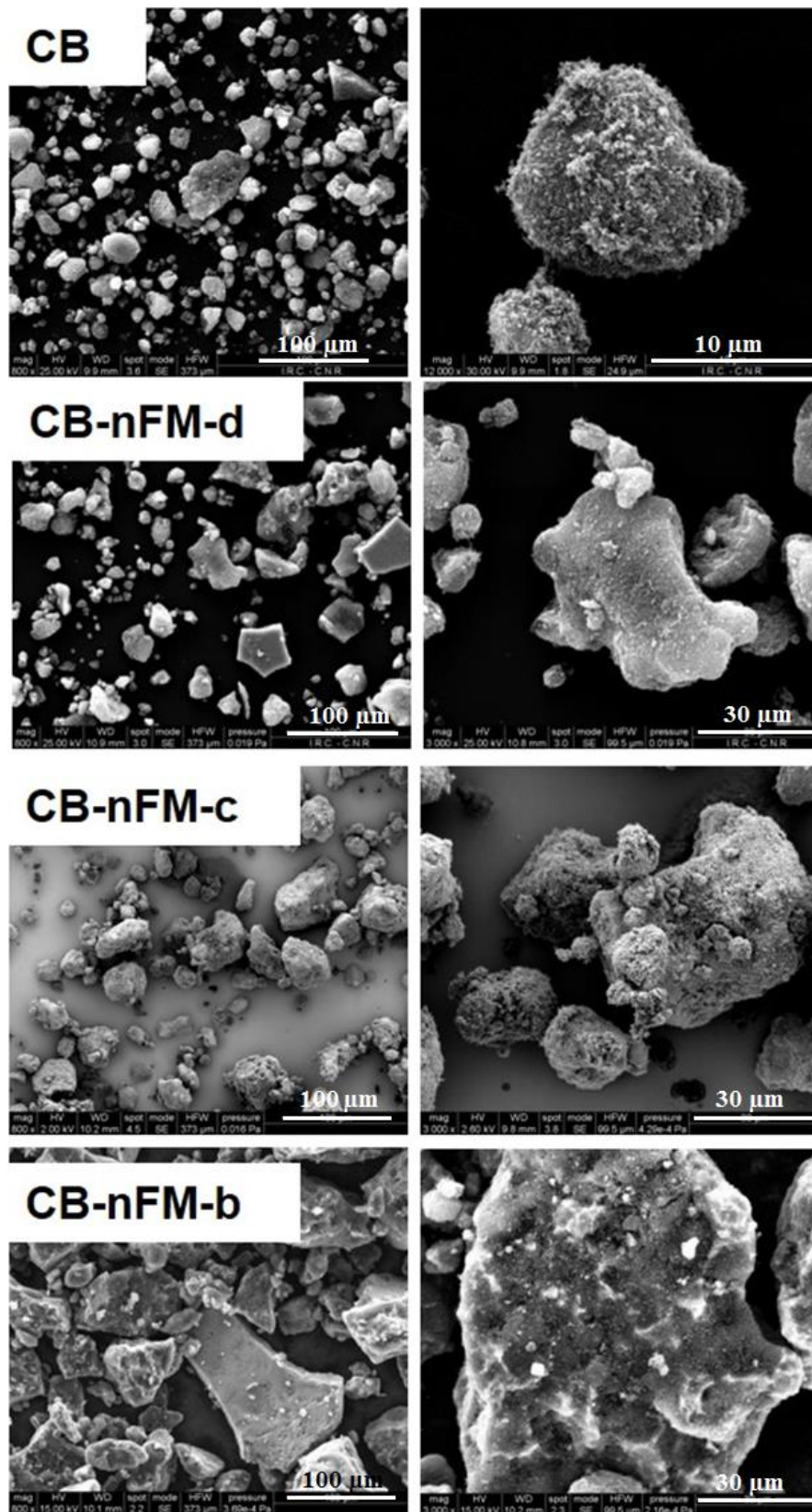Figure 49 – ICP-MS analysis data of CB-nFM series nanocomposites

Figure 50 – SEM images of samples selection belonging to CB-nFM series

The textural properties of samples selection of CB-nFM series were investigated performing Ar adsorption tests at 87 K. The isotherms are reported in Figure 51

together with pure nFM, raw CB and CB-NaOH for comparison. In all cases, isotherms typical for mesoporous materials are measured.

a   b
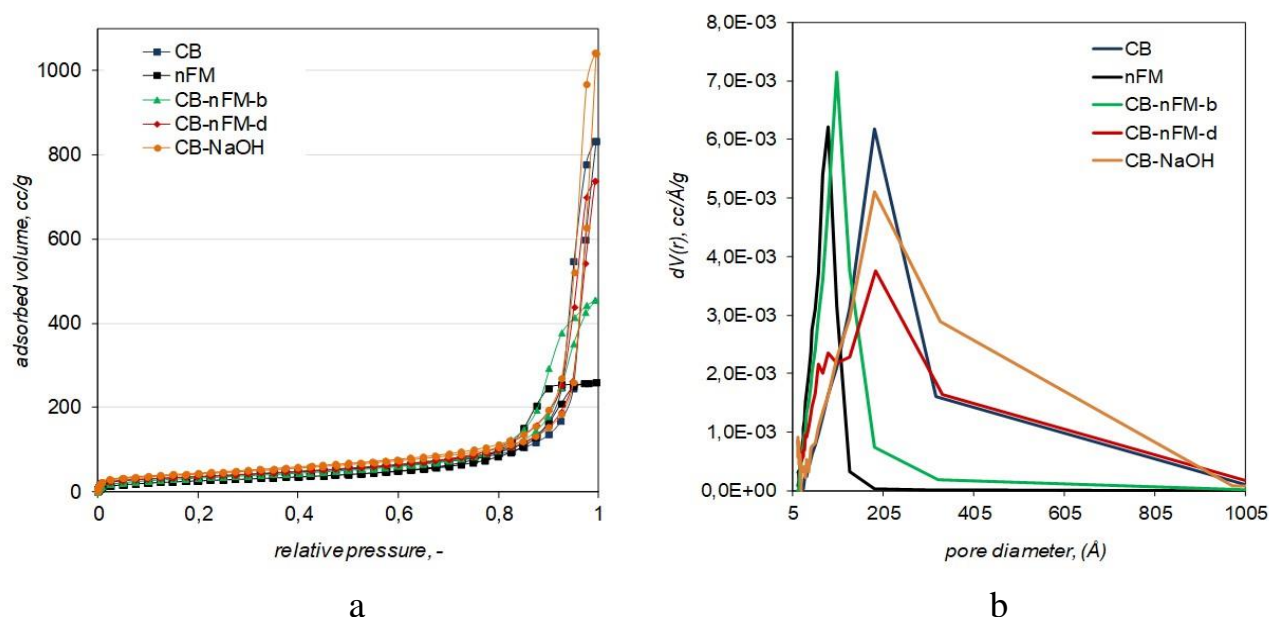
Figure 51 – Ar adsorption isotherms at 87 K (a) and pore size distributions (b) of samples selection belonging to CB-nFM series

CB, CB-NaOH and the composite richer in CB (CB-nFM-d) exhibit a very high Ar uptake at relative pressures above 0.8, indicating a well-developed mesoporosity. It is worth of noting that such uptake is higher in CB-NaOH than in CB, assuming that the treatment with NaOH favors the development of additional mesoporosity.

nFM exhibits a lower uptake in that pressure range while CB-nFM-b exhibits a higher uptake compared to nFM but a quite far uptake compared to raw CB.

The specific surface area values calculated by means of BET equation, total pore volume at $p/p^0=0.99$ and pore size distribution determined by means of BJH model are reported in Table 20.

Table 20 – Textural properties estimated for samples of the CB-nFM series

Sample	BET area m^2/g	V_{tot} ($p/p^0=0.99$) cm^3_{liq}/g	V_{micro} cm^3/g
CB	162	0.102	1.17E-03
nFM	84	0.329	1.54E-03
CB-nFM-b	119	0.302	1.06E-03
CB-nFM-d	199	0.232	3.63E-03
CB-NaOH	180	0.128	4.08E-03

All the SA values are below 200 m^2/g confirming the mesoporous character of all investigated samples. Looking at the pore volume data, a great textural variability

arises: total pore volumes are higher for nFM and the composites while the volumes of micropores are higher for CB-NaOH and CB-nFM-d.

As concerns the pore size distributions looking at the curves reported in Figure 51, as expected, nFM and CB-nFM-b have similar distributions, even if that of CB-nFM-b is peaked at higher values. CB and CB-NaOH exhibit similar PSD curves confirming the marked mesoporous character while CB-nFM-d exhibits a PSD curve containing the features of both constituents (CB and nFM).

The presence of the desired ferric oxide form (nanoparticulate magnetite) in each composite was assessed by XRD measurements. The resulting XRD patterns, height normalized and shifted on the vertical for clarity, are reported in Figure 46. The XRD pattern of nFM is also reported for comparison. In the diffraction spectra of all samples, a wide halo is observed throughout the entire region. The intensity of reflexes corresponding to amorphous glass is very low, so one-two of the strongest lines is visible; also as it can be seen 35º and 62º at 2Θ characterized magnetite (Fe_3O_4).
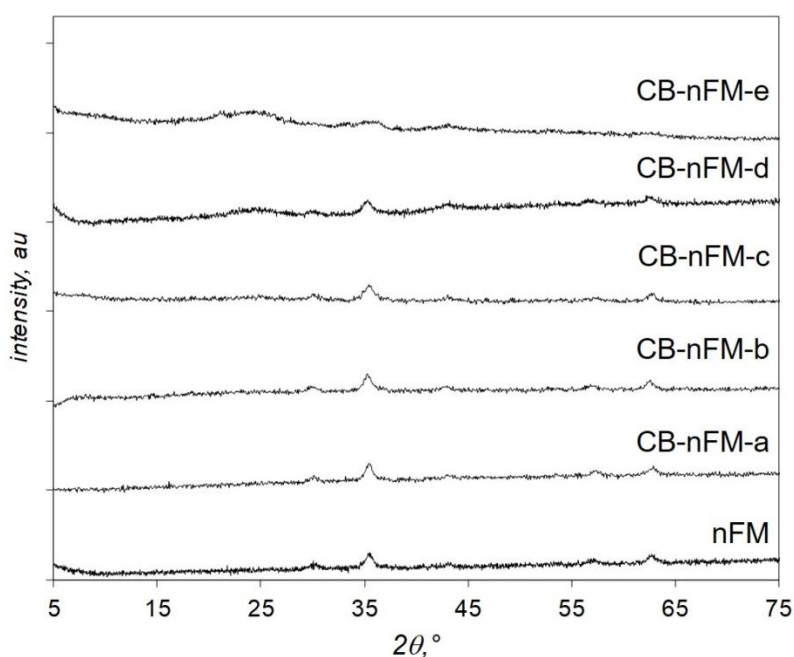
Figure 52 – XRD patterns of samples of the CB-nFM series

The thermal stability of the samples under oxidative conditions (air) was evaluated by TGA. The TG profiles and the corresponding DTG curves are reported in Figure 53, the data of nFM, CB and CB-NaOH are also reported for comparison.

All the composites are stable up to 400 °C and the carbonaceous part (CB) is completely burned before 650 °C. For all the composites the burn off temperature is lower than those of CB and CB-NaOH (around 680 °C). This result is due to catalytic effect of iron oxide favoring an early burn-off of the carbonaceous part as previously observed for CB-FM composites [131]. Also, for the materials of these series, the final residue amount after thermogravimetric analysis (ashes) is expected on the basis of the

sorbent's theoretical composition: the higher residue is found for the sorbent which is richer in nFM (CB-nFM-a).

Figure 53 – TG profiles (a) and the corresponding DTG curves (b) of the samples of the CB-nFM series

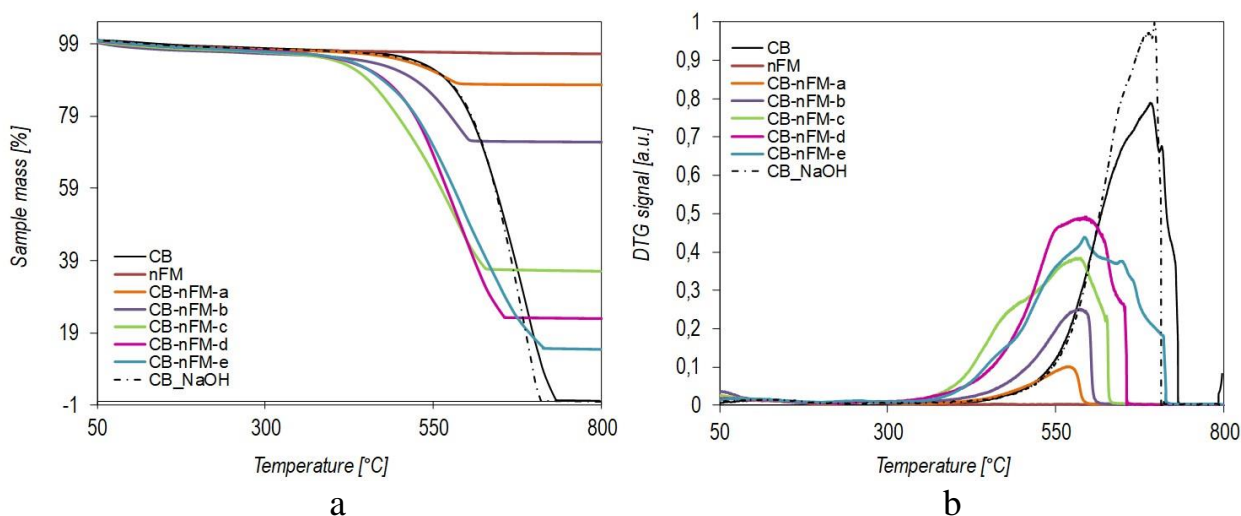## 3.2 Investigation of CO_2 sorption characteristics of carbon-based nanocomposite materials

The CO_2 uptake of cRH-derived samples (also based on CB) were evaluated from the work-up of breakthrough curves obtained through adsorption experiments under dynamic conditions in a lab-scale fixed bed reactor.[162] The adsorption experiments were performed at ambient conditions on comparable amount of sample (500 mg); each material before the adsorption tests was sieved to isolate only particles within a specific granulometric range (pelletized to particle size 180-400 µm). A CO_2/N_2 gas mixture (15 Nl/h) at a fixed 3% volume CO_2 concentration has been used to determine the breakthrough curves of each sample.

For each material the following quantities have been calculated:

1) m_{ads} or mass of carbon dioxide adsorbed by mass unity of adsorbent, accounted by inserting the breakthrough curves;

2) t_b,breakpoint or breakthrough time - the time required for CO_2 to achieve 5% of the incoming concentration at the adsorption column outlet.

The adsorption results on cRH-based samples obtained after alkaline treatments will be first presented. After that, the adsorption results on samples belonging to cRH-FM, cRH-nFM and CB-nFM series will be described. A comparison of all investigated samples performance will then be reported.

3.2.1 CO_2 sorption characteristics of carbonized rice husk and alkali treated carbonized rice husk

The breakthrough curve of cRH is reported in Figure 54, the corresponding values of m_{ads} and t_b are reported in Table 21. The sigmodal shape of the curve is indicative

of a favorable interaction between the cRH and the CO_2, but the very low breakthrough time (8 s) highlights the quick saturation of the adsorption sites on the material surface.
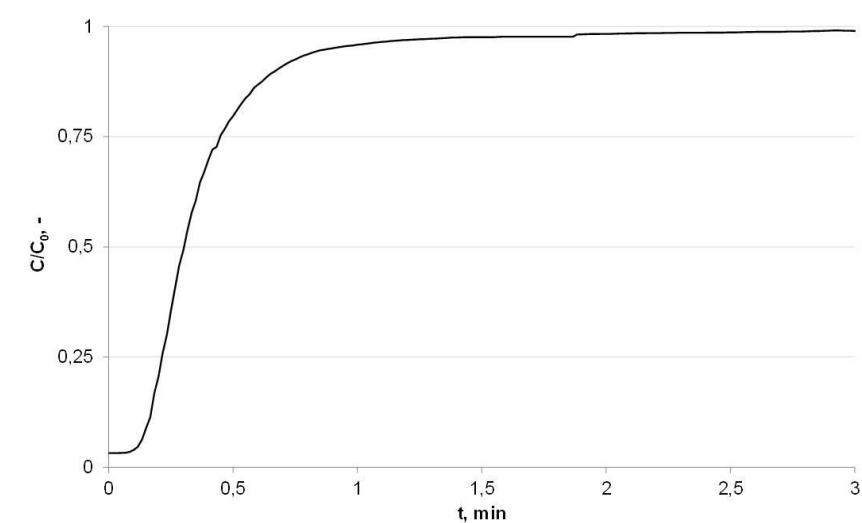

Figure 54 – cRH breakthrough curve (mixture of gases CO_2 and N_2 (15 Nl/h) at a constant 3% vol. CO_2 concentration)

Overall, the cRH CO_2 uptake is not very high if compared to other carbon-based sorbents analyzed in similar conditions [163]. The material acts, as expected, as a physisorbent since it does not contain any reactive moieties (as basic functional groups or unsaturated coordination centers) able to establish strong interaction with acidic CO_2 molecules [95]. Moreover, cRH exhibits a very low microporosity. That is a fundamental characteristic to act as a good physisorbent material.

Table 21 – CO_2 uptakes (m_{ads}) and breakthrough times (t_b) of cRH and alkali treated samples

Sample	m_{ads} (mg/g)	T (s)
cRH	11.3	8
cRH-NH$_4$OH (1 g, 1h)	29.2	21
cRH-NH$_4$OH (10 g, 1h)	13.7	12
cRH-NH$_4$OH (10 g, 4h)	11.9	10
cRH-NH$_4$OH (10 g, 6h)	12.0	10
cRH-NaOH (1 g, 2h)	21.9	13
cRH-NaOH (10 g, 2h)	15.3	14

The treatment with strong alkali solutions allowed the production of sorbents with different sorption characteristics. The CO_2 uptake of these materials is listed in Table 21 and graphically compared in Figure 55. The treatment with a strong alkali solution (NaOH or NH$_4$OH) allowed producing a material with a better sorption capacity. In the case of cRH-NH$_4$OH (1g, 1h) a considerable higher CO_2 uptake value was obtained (60 % higher with respect to raw cRH). This result is comparable to values obtained in

the same experimental conditions by chemisorbent materials, namely sorbents containing reactive sites with high affinity towards CO_2 in their structure [163].
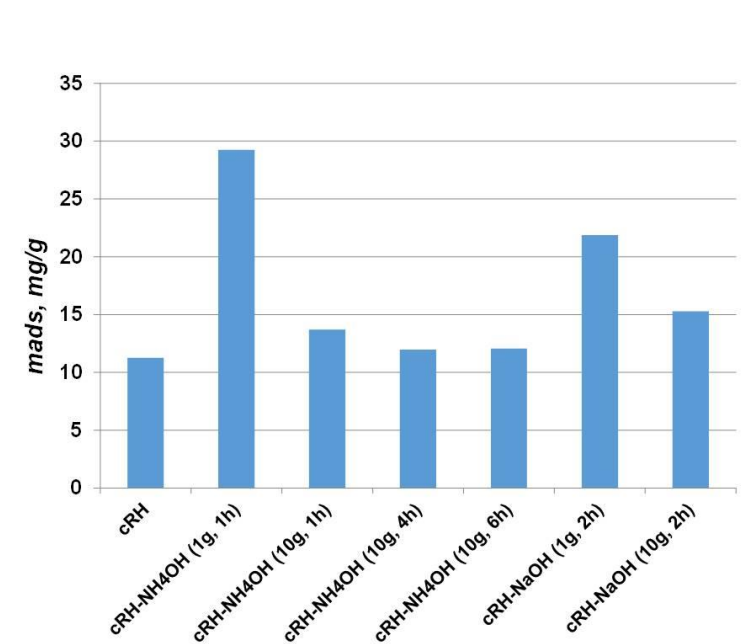

Figure 55 – Graphical comparison among CO_2 uptakes of cRH alkali-treated samples

Figure 55 evidences that the samples obtained after longer treatments with NH_4OH (up to 6 h) or by using higher starting amounts of cRH (up to 10 g) exhibit slightly higher CO_2 uptakes compared to the raw cRH, but lower CO_2 uptake compared to cRH-NH_4OH (1g, 1h). These differences can be ascribed to higher purity of the obtained sample in terms of higher carbon content (acting as physisorbent phase thanks to its porosity) and lower content of other elements as silica (see Table 13, section 3.1.1), and so to the overall textural properties.

The samples obtained after treatment with NaOH exhibit a clearly better sorption capacity compared to the raw cRH (26% of increment with respect to cRH): this result is likely due to the efficient removal of silica and other inorganics that are a not-adsorbing phase. Indeed, in case with cRH-NaOH samples a surface area increase is detected (431 m^2/g) as a result of the removal of inorganic phase clogging pores of the carbonaceous matrix. It is interesting to observe that the sample belonging to the cRH-NH_4OH series obtained treating the smallest amount of cRH (1g) for 1h with NH_4OH-cRH-NH_4OH (1g, 1h)- exhibits the highest CO_2 uptake even in comparison to the samples from the cRH-NaOH series. The use of that material for practical purposes is not economically beneficial also in view of the scale-up of the treatment process but the peculiar behavior of this sample (up to now is not completely clear) surely deserves more dedicated and fundamental study that is beyond the aim of this thesis.

3.2.2 CO_2 sorption characteristics of carbonized rice husk-magnetite composites

The breakthrough curves of a selection of samples belonging to cRH-FM series are reported in Figure 56 where the curves of raw cRH and pure FM are also reported for comparison (mixture of gases CO_2 and N_2 (15 Nl/h) at a constant 3% vol. CO_2

concentration). The shape of all curves is indicative of an overall favorable interaction between the sorbents and CO_2. Very low breakthrough times highlight, also for the composites, a quick saturation of the adsorption sites.
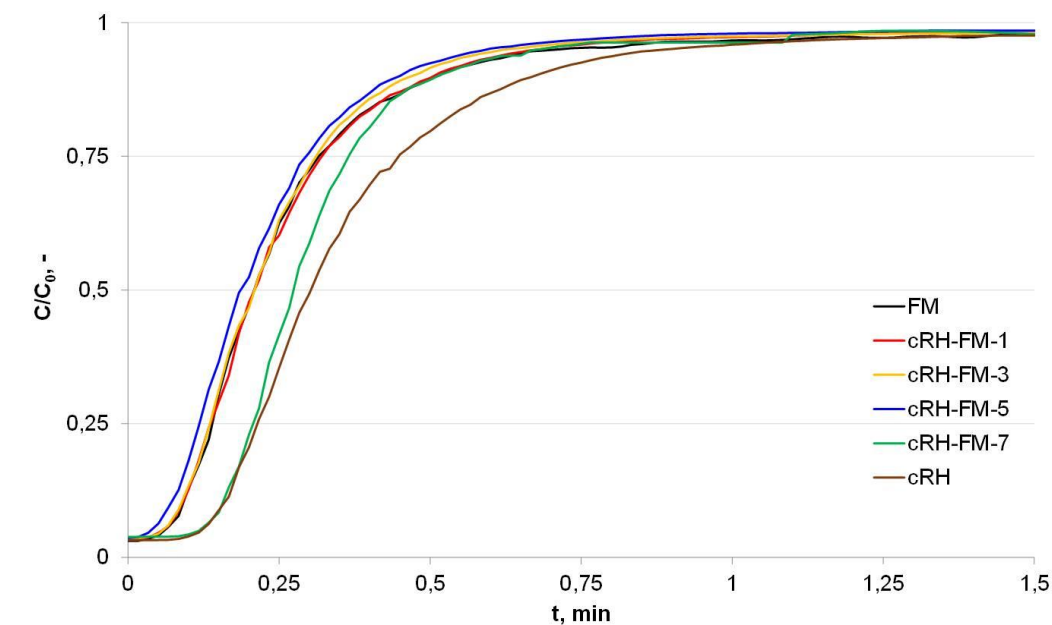
Figure 56 – cRH breakthrough curves of a selection of sorbents of cRH-series

The values of m_{ads} and t_b of the composite materials of cRH-FM series are reported in Table 22. Graphical comparisons among the m_{ads} values (panel a) and among the t_b values are reported in Figure 57.

Table 22 – CO_2 uptakes (m_{ads}) and breakthrough times (t_b) of cRH-FM series samples

Samples	m_{ads} mg/g	t_b s	Number of the sample in Figure 51
cRH	11.3	8	1
cRH-FM-7	9.59	8	2
cRH-FM-6	8.44	6	3
cRH-FM-5	7.4	3	4
cRH-FM-4	7.4	4	5
cRH-FM-3	8.9	4	6
cRH-FM-2	11.9	7	7
cRH-FM-1	9.4	4	8
FM	10.9	4	9

The raw cRH and pure FM exhibit comparable CO_2 uptakes; the m_{ads} estimated for the cRH-FM composite materials exhibit a great variability. Overall, it can be observed that the CO_2 uptake does not take any advantage from the combination of cRH and FM: only for one sample (cRH-FM-2, point #7 in Figure 57) a slightly higher m_{ads} value with respect the two pure components is detected.

Figure 57 – Graphical comparison of CO_2 uptakes m_{ads} (a) and t_b (b) of cRH-FM series as function of FM content

As general trend, in the cRH-FM series higher m_{ads} values are detected for those samples containing more than 60 wt.% of FM. Since these samples are also the samples with lower SA values (cRH-FM-2, 119 m^2/g, Table 16, section 3.1.3) also if compared to cRH, cRH-NH$_4$OH and FM (162, 180 and 136 m^2/g, respectivel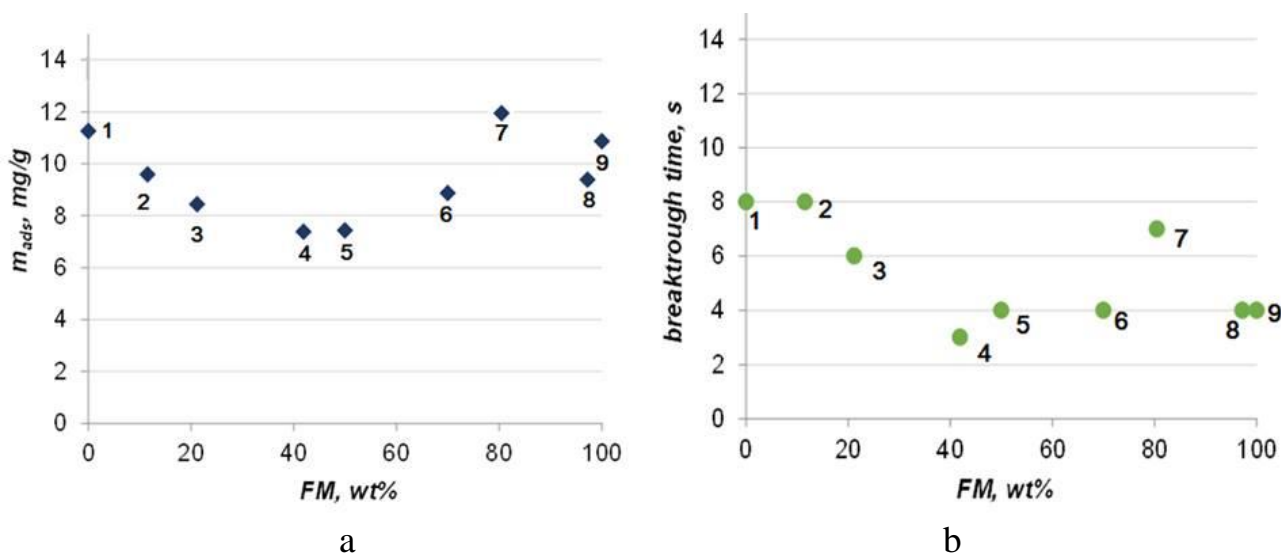y, Table 16, section 3.1.3), a combined chemisorption and physisorption behavior can be hypothesized for these materials. On the other side, lower m_{ads} values are detected for those samples containing less than 50 wt.% of FM. These sorbents exhibit the higher SA values in the cRH-FM series (cRH-FM-6, 199 m^2/g, table 16, section 3.1.3) allowing us to speculate that the gain in a low quantity of chemisorbent material (FM) in the cRH-FMx composition does not counterbalance the high pore size loss in the 5 nm range, relevant for CO_2 capture (Figure 33b, section 3.1.3) .

As a final consideration, all the materials belonging to the cRH-FM series are characterized by m_{ads} values lower than those reported for samples obtained by treating cRH with NH$_4$OH solution (Table 21).

3.2.3 CO$_2$ sorption characteristics of carbonized rice husk-nanoparticulate magnetite composites

The values of m_{ads} and t_b of the composite materials belonging to cRH-nFM series are reported in Table 23. Graphical comparisons among the m_{ads} values (Figure 58a) and among the t_b values (Figure 58b) are reported in Figure 58. The neat nFM exhibit a higher CO_2 uptake compared to the cRH (13.8 and 11.3 mg/g, respectively) but overall lower with respect to the cRH-NaOH sample (15.3 mg/g) here reported for comparison since the samples of the cRH-nFM series were obtained using NaOH to establish alkaline condition for nFM formation. The m_{ads} values estimated for the cRH-nFM series exhibit, also in this case, a great variability.

In the case of the composites of cRH-nFM series the CO_2 uptake trends appeared clearly defined: for a nFM loading lower than 50 wt.%, the CO_2 uptake tends to increase up to 15.6 mg/g (sample cRH-nFM-d); at higher nFM load, the CO_2 uptake

drops reaching the lowest value of 9.00 mg/g (sample cRH-nFM-b). In this case a synergistic effect driven by the cooperation between the carbonaceous support (cRH) and nFM is evidenced for low nFM loadings.

Table 23 – CO_2 uptakes (m_{ads}) and breakthrough times (t_b) of cRH-nFM series samples

Samples	m_{ads} mg/g	t_b s	Number of the sample in Figure 52
cRH	11.3	8	1
cRH-nFM-e	13.9	14	2
cRH-nFM-d	15.6	12	3
cRH-nFM-c	11.8	12	4
cRH-nFM-b	9.00	4	5
cRH-nFM-a	10.0	7	6
nFM	13.8	9	7

a

b
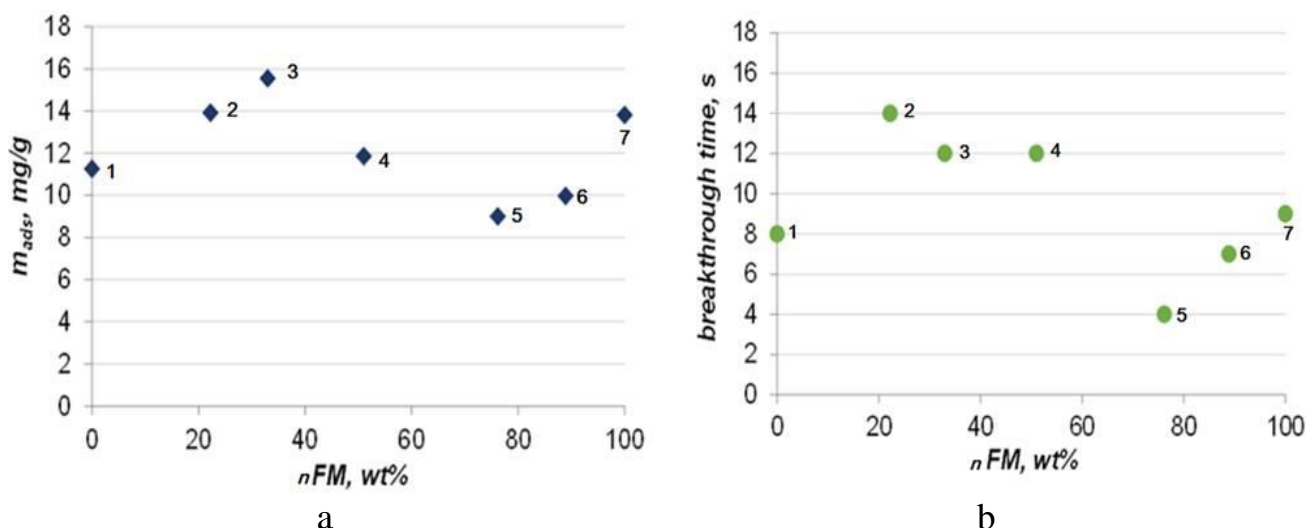
Figure 58 – Graphical comparisons among CO_2 uptakes m_{ads} (a) and t_b (b) of cRH-nFM samples as function of nFM content

At higher nFM load the lower CO_2 uptake can be rationalized taking into account cRH pore clogging phenomena, as also indicated from the surface area values and pore size distribution analysis (cRH-nFM-b and cRH-nFM-d, 190 m^2/g and 271 m^2/g, respectively, table 16, section 3.1.4).

3.2.4 CO_2 sorption characteristics of composites based on carbon black-nanoparticulate magnetite

The values of m_{ads} and t_b of the composite materials belonging to CB-nFM series are reported in Table 24. Graphical comparisons among the m_{ads} values (a) and among the tb values (b) are reported in Figure 59.

Table 24 – CO_2 uptakes (m_{ads}) and breakthrough times (t_b) of CB-nFM series samples

Sample	m_{ads} mg/g	t_b s	Number of the sample in Figure 53
CB	7.50	4	1
CB-nFM-e	10.8	11	2
CB-nFM-d	10.1	10	3
CB-nFM-c	9.36	10	4
CB-nFM-b	8.54	1	5
CB-nFM-a	9.00	5	6
nFM	13.8	9	7

a   b
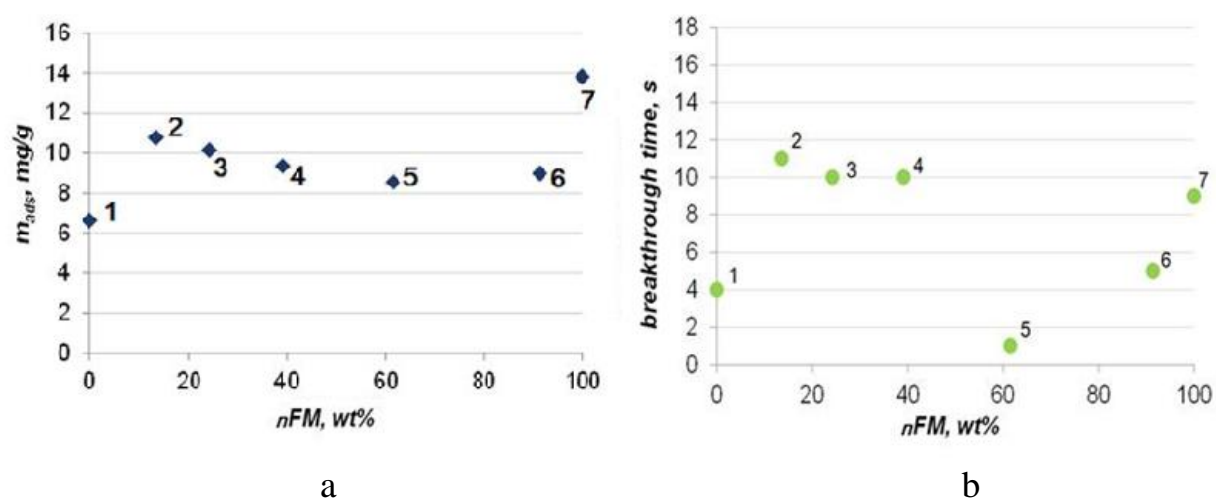
Figure 59 – Graphical comparison of CO_2 uptakes m_{ads} (a) and t_b (b) of CB-nFM samples as function of nFM content

The materials of the CB-nFM series have been produced applying the same synthetic approach used for cRH-nFM series in order to compare cRH-based composites with a set of materials produced starting from a non-porous carbonaceous support with a very low content of inorganic matter (below 2 wt.%). The CB-FM series was previously studied in Alfe et al [131].

Generally, samples of the CB-nFM series exhibit a slightly higher CO_2 uptake (from 8.5 to 10.8 mg/g) compared to the raw CB (7.50 mg/g) but lower of neat nFM (13.8 mg/g). The CO_2 uptake trend of the CB-nFM series is quite flat without clearly identified maxima or minima peaks. Even if the textural characteristics of the low nFM loaded CB and the high nFM loaded CB resembles those of CB and nFM, respectively (3.1.4 section), the combination of the two phases (CB and nFM) into a composite it is not advantageous for CO_2 capture applications.

3.3 Comparison among the carbon-based composites and discussion of experimental results

The comparisons among CO_2 uptakes (m_{ads}) of the cRH-derived series (cRH-FM and cRH-nFM), CB-derived series (CB-FM and CB-nFM) and CB-nFM and cRH-nFM

series as a function of nFM content are reported in the following Figure 60 and Figure 61.

a b
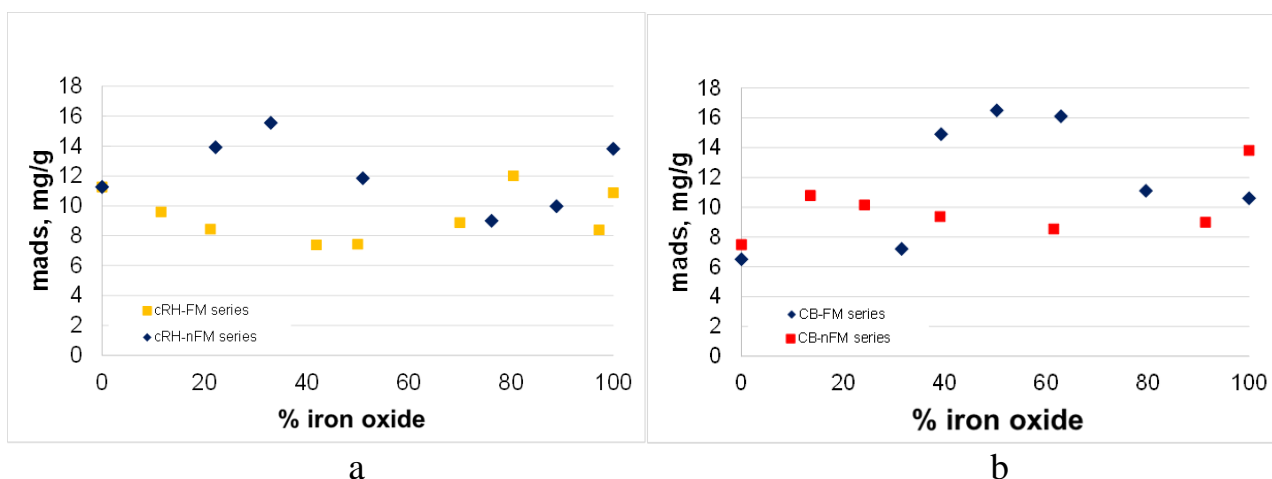
Figure 60 – Comparisons among CO_2 uptakes m_{ads} of the cRH-derived series (a), CB-derived series (b) as a function of iron oxides (FM and nFM) content

a b
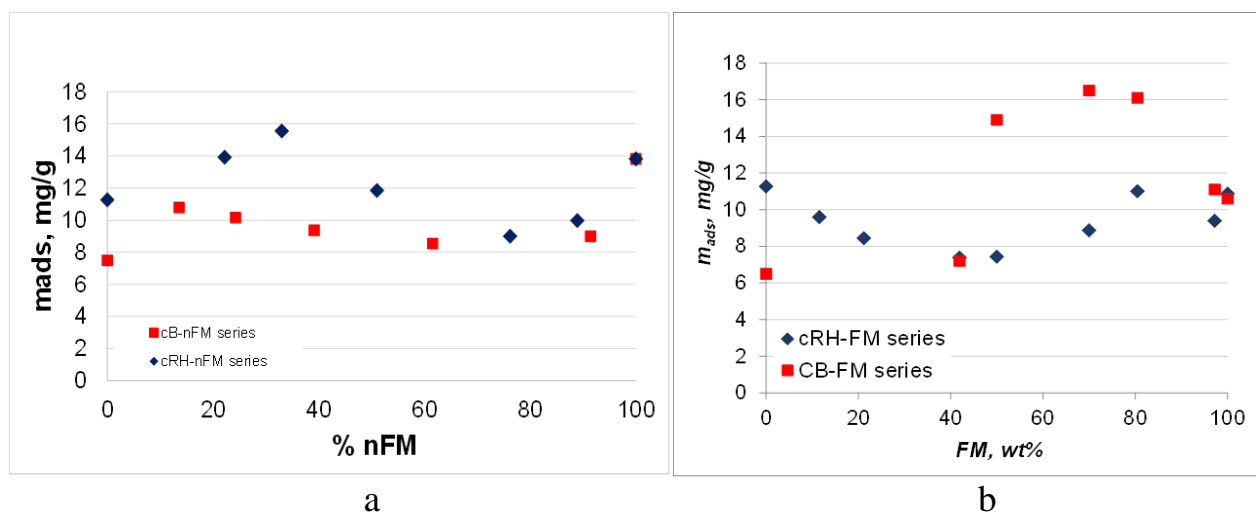
Figure 61 – Comparisons among CO_2 uptakes m_{ads} of the carbon-based modified by nanoparticulate magnetite composites (a) and carbon-based modified by magnetite composites (b) as a function of nFM and FM content

From the comparison of the CO_2 uptakes it can be observed that the use of magnetite nanoparticles (nFM) gives some advantages when applied to coat a support made up by micrometric particles (as cRH is) rather than to coat a support made up by nanometric particles (as CB is, whose aggregate dimension is 180 nm) allowing to produce synergistic effects between the two phases (nFM and the carbonaceous support, chemisorption and physisorption phases, respectively) enhancing CO_2 adsorption. The very low CO_2 uptakes can be probably related to pore clogging phenomena occurring with a different extent and modality on the two different carbonaceous phases during the composites production.

3.3.1 Comparison of the CO_2 adsorbent material used in the laboratory scale static fixed-bed reactor in ambient conditions

Materials produced in the framework of dissertation work were tested in typical post-combustion technology in ambient pressure and temperature with CO_2 concentration up to 5%. Table 25 presents results, which was received in the same condition at fixed bed, but produced by using different methods of synthesis and materials [94, 115, 131, 132, 135, 136 149, 152, 161, 163].

Table 25 – Materials investigated as a CO_2 adsorbent in the same condition

Sample	Description	m_{ads} (mg/g)	t* (s)
cRH	Carbonized rice husk	11.26	8
cRH-FM	Carbonized rice husk-magnetite	12.00	7
cRH-nFM	Carbonized rice husk-nanoparticulate magnetite	15.55	12
cRH-NH$_4$OH	Carbonized rice husk-treated by NH$_4$OH	29.2	25
nFM	Nanoparticulate magnetite	13.81	9
CB-nFM	Carbon black-nanoparticulate magnetite	10.8	11
cRH-NaOH	Carbonized rice husk treated by NaOH	21.88	13
CB	Carbon black	6.5	2
FM	Magnetite	10.8	1
CB$_{ox}$	Oxidized carbon black	6.6	0
CB–FM	Carbon black–Magnetite composite	18.3	2
CB$_{ox}$–FM	Oxidized carbon black–Magnetite composite	8.0	1
CB–IL	Ionic liquid supported on carbon black	27.3	18
CB$_{ox}$–IL	Ionic liquid supported on oxidized carbon black	9.9	6
CB$_{ox}$–NH$_2$	Oxidized carbon black - amino-groups	12.8	1

First seven samples of the sorbent described in this research, others provided by previous results from applied references. High sorption capacity is due to cRH-NH$_4$OH, CB-IL and cRH-NaOH adsorbent. Both materials based on rice husk have possibility to following investigations; at once carbon-black supported with ionic liquid is a sorbent with high adsorption capacity. But a significant difference is the price advantage of cheaper materials based on rice husks and its simple method of production, while materials have a more complex obtaining process, which increases the price criterion. Patent of utility model #4302 of the Republic of Kazakhstan named "Method of producing sorbent based on rice husk" developed by Zhumagaliyeva A. and Doszhanov Ye. is applied to appendix.

Carbonaceous sorbents for CO_2 capture applications were produced starting from carbonized rice husk (cRH) by base leaching with NH$_4$OH or NaOH and coating with iron oxide nanoparticles were applied to improve cRH sorption performances. After a

structural characterization, the materials were tested as potential CO_2 sorbent in labscale fixed bed reactor. The materials exhibited improved sorption capacities against CO_2 in comparison with the starting material cRH but overall their performances were lower than those of conventional carbon-based sorbents or related materials obtained by coating carbon black with iron oxide. The data acquired on cRH-derived sorbents together with the CO_2 adsorption data acquired in dynamic conditions in a lab-scale fixed-bed reactor or in a fluidized-bed reactor on commercial and ad-hoc synthetized sorbents were used to tentatively correlate adsorption capacities and materials textural properties or relevant adsorption parameters. The correlation of m_{ads} vs. surface area allows gathering the sorbents into three groups corresponding to the three main CO_2-material interactions: physisorption, physisorption+chemisorption, and chemisorption. Table 26 exhibit collected data about adsorption properties and structured characteristics of materials, tested in typical post-combustion [ref in 163].

Table 26 – CO_2 adsorption and textural properties

	Sample	m_{ads} mg_{CO2} g^{-1}	t_b, s	$\Delta\tau$, s	W, %	SA m^2 g^{-1}	Total pore volume cm^3 g^{-1}	Micropores volume cm^3 g^{-1}	Mesopores volume cm^3 g^{-1}	$\%CO_2$ %vol. in N_2
1	2	3	4	5	6	7	8	9	10	11
chemisorption	HKUST-1 (Zn)	13.86	10.00	13.00	29.22	20	0.0068	-	0.0068	3
	MIL-96 (Al)	21.66	15.00	27.00	36.41	51	0.0047	0.0180	0.0029	3
	CBox–NH$_2$	12.80	1.00	16.00	n.a.	30	0.0044	0.0005	0.0039	3
	CB–IL	27.30	18.00	22.00	n.a.	36	0.0055	0.0019	0.0036	3
	CBox–IL	9.90	6.00	16.00	n.a.	40	0.0127	0.0057	0.0070	3
physisorption+chemisorption	HKUST-1 (Cu)*	22.88	n.a.	n.a.	n.a.	680	0.6600	n.a.	n.a.	5
	FM	10.60	13.00	n.a.	n.a.	154	0.0472	0.0089	0.0383	3
	CB–FM-1	11.10	15.00	15.00	n.a.	160	0.0534	0.0179	0.0355	3
	CB–FM-2	16.10	25.00	19.00	n.a.	148	0.0405	0.0159	0.0246	3
	CB–FM-3	16.50	24.00	16.00	n.a.	157	0.0359	0.0098	0.0261	3
	CB–FM-4	14.90	27.00	18.00	n.a.	157	0.0338	0.0088	0.0250	3
	CB–FM-5	7.20	3.00	19.00	n.a.	145	0.0312	0.0105	0.0207	3
	CBox–FM	8.00	1.00	19.00	n.a.	248	0.0531	0.0181	0.0350	3
	nFM	13.81	9.00	12.00	28.27	84	0.339	0.0015	0.3375	3
	cRH-nFM	15.55	12.00	n.a.	n.a.	271	0.326	0.038	0.288	3
	C-700	19.34	n.a.	n.a.	n.a.	463	0.4800	n.a.	n.a.	10
	SBA-APTSgraf	13.55	n.a.	n.a.	n.a.	230	n.a.	n.a.	n.a.	4
	SIFSIX-2-Cu-i	55	n.a.	n.a.	n.a.	735	0.26	n.a.	n.a.	10
	RN-450-3	41.36	n.a.	n.a.	n.a.	1432	0.53	n.a.	n.a.	10
	NC-650-3	48.4	n.a.	n.a.	n.a.	1535	0.56	n.a.	n.a.	10
	RUK-600-3	43.12	n.a.	n.a.	n.a.	1404	0.53	n.a.	n.a.	10

Table continuation 26

1	2	3	4	5	6	7	8	9	10	11
physisorption	CB	6.50	2.00	n.a.	n.a.	143	0.1750	0.0050	0.1700	3
	CBox	8.81	8.00	11.00	38.80	277	0.5700	0.3600	0.2100	3
	CNT	16	n.a.**	n.a.	n.a.	394	0.63	n.a.	n.a.	5
	GAC Filtr 400	14	n.a.	n.a.	n.a.	954	0.48	n.a.	n.a.	5
	cRH	11.26	8.00	15.00	30.76	105	0.0640	0.0410	0.0230	3
	cRH_NaOH	15.28	14.00	20.00	38.78	431	0.3750	0.1700	0.2050	3
	cRH_NH$_4$OH	12.04	10.00	14.00	n.a.	180	0.0640	0.0410	0.0230	3
	CBox_T	11.12	14.00	8.00	58.19	464	0.9000	0.5800	0.3200	3
	MIL-100 (Fe)	7.71	2.00	10.00	13.58	1105	0.7400	0.6000	0.1400	3
	AC Norit*	10.56	n.a.	n.a.	n.a.	1060	1.3400	n.a.	n.a.	10
	Zeolite 13X*	10.12	4.00	n.a.	n.a.	960	0.4100	n.a.	n.a.	10
	Zeolite Na-Y*	8.36	n.a.	n.a.	n.a.	756	0.4000	n.a.	n.a.	10
	TUFF	1.54	12.00	11.00	n.a.	141	n.a.	n.a.	n.a.	5
	Zeolite CBV100	13	n.a.	n.a.	n.a.	788	0.35	n.a.	n.a.	5
* fluidized bed; **n.a. – not analyzed										

In the Table 26 the time parameter $\Delta\tau = t_{70}-t_{10}$ (with t_{10} and t_{70} being the time for which CO_2 reach 10% and 70% of the inlet concentration at the adsorption column outlet, respectively), which is related to the slope of the linear part of the sigmoid (the smaller this parameter is, the steeper the breakthrough curve and consequently the faster the adsorption kinetics will be); the fraction of bed utilized at breakpoint, W, namely the ratio between the CO_2 adsorbed until the breakpoint and that adsorbed until saturation.

It is clear from the analysis in Table 26 that the RH-derived materials exhibited different CO_2 adsorption performances. The starting material cRH exhibited the lowest sorption capacity and only a slight increase of CO_2 sorption is detected in cRH-NH4OH sample. The treatment with a stronger basic solution (NaOH 5M) allowed to produce a material with better sorption capacity (26% of increment with respect to cRH): this result is likely due to the removal of silica and other inorganics that are a not-adsorbing matrix. In the case of cRH-NaOH a not negligible increase of surface area is detected as a result of the removal of inorganics clogging the pores of the carbonaceous matrix. The coating with iron oxide nanoparticles did not correspond to a noticeable increment of the sorption capacity, since even if the m_{ads} of cRH-nFM is higher compared to that of cRH, it results comparable to the cRH-NaOH performances. Furthermore, it can be also observed that the m_{ads} value of cRH-nFM is pretty similar to the sum of the m_{ads} values of the two components (cRH-NaOH and nFM) scaled for the relative quantities inside the composite material (~ 65 and ~ 35 wt.%, respectively).

The correlation of m_{ads} vs. t_b indicates that higher t_b values are exhibited by sorbents falling in the chemisorption+ physisorption regime, the lower t_b value for materials falling in the almost pure physisorption regime while an intermediate trend is discernible in the case of chemisorbents. These results confirm there is no robust

linear relationship between the surface area and the adsorption of CO_2 at a given pressure and that both the textural properties (surface area, pore volumes, pore shapes) and materials surface chemistry have to be considered (Figure 62). In particular, the results on materials falling in the physisorbent regime agree with the correlation reported by Yin et al. for a wide group of activated carbons. In general, for materials acting as pure physisorbents the surface area has little effect on CO_2 adsorption at lower adsorption pressures as those typical of post-combustion conditions.
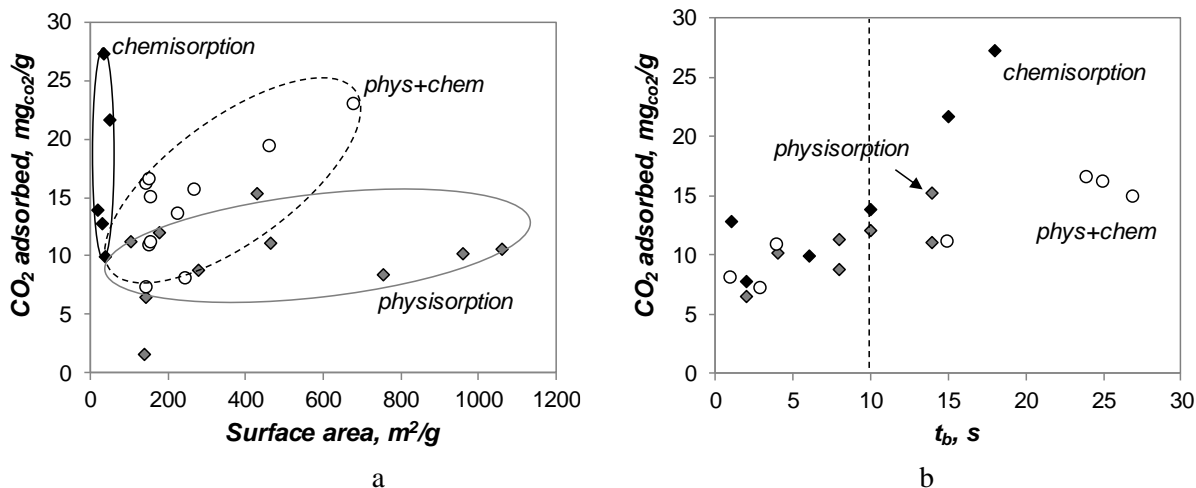

Figure 62 – Plots of m_{ads} vs surface area (a)   and m_{ads} vs t_b (b) as a function

m_{ads} was also reported as a function of the breakthrough time t_b (Figure 62b). For this correlation, only data acquired under the same experimental conditions (fixed-bed, CO_2 inlet pressure 3%) were considered. t_b together with the m_{ads}, is widely considered a useful single metric for ranking adsorbents, since, for practical purposes, a high value of tb is highly desirable because it reduces the frequency of sorbent regeneration. On the basis of the available data and as a very preliminary outcome, Figure 62b indicates that materials acting in the chemisorption+physisorption regime exhibit higher breakthrough times (> 15 s) for a quite limited CO_2 uptake (11-22 mg CO_2/g). The materials falling in the almost pure physisorption regime overall exhibited the lowest t_b (< 15 s) while an intermediate trend is discernible for chemisorbents.

A focused experimental campaign is planned to shed light into possible correlations between t_b and the other parameters characterizing a sorbent under dynamic conditions with the final goal of defining the combination of characteristics that a suitable sorbent for post-combustion CO_2 capture have to exhibit.

CONCLUSIONS

In a view of exploiting the advantages and shortcomings in the use of a real biomass as starting material for preparation of sorbent for CO_2 capture applications in this thesis carbonized rice husk (cRH) was used for preparation of different solid sorbents tested under dynamic condition in a lab-scale fixed bed reactor. Rice husk has been selected as waste biomass since it is widely available as waste material in all rice producing countries such as Kazakhstan.

At first, a set of materials was prepared by treating cRH with strong bases (NH_4OH and $NaOH$) with purpose of evaluating the effect of base leaching on material sorption performances. Then composite materials have been produced by coating cRH with different amount of iron oxide particles (FM) or nano disperse FM particles (nFM). A set of composite materials containing a non-porous material (carbon black) as support and nano disperse FM particles (nFM) was also produced for comparative purposes. All produced materials have been structurally, morphologically and thermally characterized. The CO_2 adsorption performances of all materials have been finally determined from the breakthrough curves obtained as result of the experimental CO_2 adsorption tests under dynamic conditions at room temperature and pressure.

1. Nanosructured composites based on carbonized rice husk and iron oxide particles exhibited different of components structural and adsorption features synthesized by coprecipitation method. It was found out that the sorption of CO_2 molecules in these materials is influenced by the indefinite presence of both micropores and mesopores. In nanostructured composites the amount of mesopores is more significant than the increase of SSA, since the latter plays the role of a tunnel for CO_2 molecules passing from mesopores to micropores

2. The optimal parameters of producing alkali treated cRH is developed. The maximum adsorption capacity of material achieved by alkaline treatments by NH_4OH is 29.2 mg/g is set to ratio of 1: 9, the sorbent has properties of chemisorption interaction, containing in structure reactive sites with high affinity towards CO_2. cRH treated by $NaOH$ sorbent is set to 1:20 exhibited 21.9 mg/g of adsorbed CO_2 , this efficiency bounded with removal of inorganic phase clogging the pores of the carbonaceous matrix provided physisorption behavior

3. CO_2 sorption performances of synthesized nanostructured composites on static laboratory-scale fixed-bed microreactor in post-combustion flue-gas ambient conditions have been evaluated. Negligible effect of cRH-FM composite increased adsorption capacity up to 11.9 mg/g displaied due to weak appearance of chemisorption interractions in composite.

4. Composite based on cRH modified by nanoparticulate magnetite perform 15.5 mg/g adsorption capacity has been developed. Relation of the components cRH and nFM corresponds to 24:76, detected cluster of magnetite particles in range 40-90 nm. SSA area is increased to 271 m_2/g, the efficiency rationalized taking into account cRH pore clogging phenomena. The sorbent exhibit physisorption interraction. All synthesized materials exhibit stable adsorption/desorption kinetics under vacuum at 250 °C.

REFERENCES

1 Stocker T.F., Qin D., Plattner G-K., Tignor M., Allen S.K., Boschung J., Nauels A., Xia Y., Bex V., Midgley P.M. Climate Change 2013. The Physical Science Basis // Contribution of Working Group I to the Fifth Assessment Report of the Intergovernmental Panel on Climate Change IPCC.; Cambridge, United Kingdom and New York. – NY, USA: Cambridge University Press, 2013. – P. 4.

2 McGlade C., Ekins P. The geographical distribution of fossil fuels unused when limiting global warming to 2 °C // Nature. – 2015. – Vol. 517, Iss. 7533. – P. 187-190.

3 Tian H., Lu C., Ciais P., Michalak A.M., Canadell J.G., Saikawa E., Wofsy S.C. The terrestrial biosphere as a net source of greenhouse gases to the atmosphere // Nature. – 2016. – Vol. 531. – P. 225-228.

4 Liu Y., Meng B., Hubacek K., Xue J., Feng K., Gao Y. "Made in China": A reevaluation of embodied CO_2 emissions in Chinese exports using firm heterogeneity information // Applied Energy. – 2016. – Vol. 184. – P. 1106-1113.

5 Meinshausen M. et al. Greenhouse gas emission targets for limiting global warming to 2 °C // Nature. – 2009. – Vol. 458. – P. 1158-1162.

6 Anderson T.R. Hawkins E. Jones P.D. CO_2, the greenhouse effect and global warming: from the pioneering work of Arrhenius and Callendar to today's Earth System Models // Endeavour. – 2016. – Vol. 40, Iss. 3. – P. 178-187.

7 Climate Change 2007: The Physical Science Basis. Contribution of Working Group I to the Fourth Assessment Report of the Intergovernmental Panel on Climate Change IPCC. – Cambridge: Cambridge University Press, 2007. – P. 115.

8 Gattuso J.-P., Magnan A., Bille R., Cheung W.W.L., Howes E.L., Joos F., Turley C. Contrasting futures for ocean and society from different anthropogenic CO_2 emissions scenarios // Science. – 2015. – Vol. 349, Iss. 6243. – P. aac4722.

9 Sadorsky P. Renewable energy consumption, CO_2 emissions and oil prices in the G7 countries // Energy Economics. – 2009. – Vol. 31, Iss. 3. – P. 456-462.

10 Jaforullah M., King A. Does the use of renewable energy sources mitigate CO_2 emissions? A reassessment of the US evidence // Energy Economics. – 2015. – Vol. 49. – P. 711-717.

11 Jackson R.B. et al. Warning signs for stabilizing global CO2 emissions // Environ. Res. Lett. – 2017. – Vol. 12. – P. 110202.

12 Rhodes C.J. The 2015 Paris Climate Change Conference: COP21 // Science Progress. – 2016. – Vol. 99, Iss. 1. – P. 97-104.

13 Siegenthaler U., Oeschger H. Biospheric CO_2 emissions during the past 200 years reconstructed by deconvolution of ice core data. Tellus B // Chemical and Physical Meteorology. – 1987. – Vol. 39, Iss. 1-2. – P. 140-154.

14 Special Report of Working Group III of the Intergovernmental Panel on Climate Change. – Cambridge: Cambridge University Press, 2005. – p. 4.

15 Fanchi J.R., Fanchi Ch.J. Energy in the 21st Century // World Scientific Publishing Co Inc. – 2016. – P. 350.

16 Hester R.E., Roy M.H. Carbon capture: sequestration and storage // Issues in environmental science and technology. – 2009. – 29 ed.: Royal Society of Chemistry. – P. 308

17 Benson S.M., Orr F.M. Carbon Dioxide Capture and Storage // MRS Bulletin. – 2008. – Vol. 33, Iss. 04. – P. 303-305.

18 Bhown A.S., Freeman B.C. Analysis and status of post-combustion carbon dioxide capture technologies // Environ. Sci. Technol. – 2011. – Vol. 45, Iss. 86. – P. 2-4.

19 Paul A. Adsorption technology for CO_2 separation and capture: a perspective // Webley Adsorption. – 2014. – Vol. 20. – P. 225-231.

20 Samanta A., Zhao A., Shimizu G.K.H., Sarkar P., Gupta R. Post-Combustion CO_2 Capture Using Solid Sorbents: A Review // Industrial & Engineering Chemistry Research. – 2011. – Vol. 51, Iss. 4. – P. 1438-1463.

21 D'Alessandro D.M., Smit B., Long J.R. Carbon dioxide capture: prospects for new materials // Angew. Chem. Int. – 2012. – Vol. 49, Iss.35. – P. 6058.

22 Wang M., Lawal A., Stephenson P., Sidders J., Ramshaw C. Post-combustion CO_2 capture with chemical absorption: a state-of-the-art review // Chem. Eng. Res. Des. – 2011. – Vol. 89. – P. 1609-1624.

23 Li P., Paul D.R., Chung T. High performance membranes based on ionic liquid polymers for CO_2 separation from the flue gas // Green Chem. – 2012. – Vol. 14. – P. 1052-1063.

24 Hedin N., Andersson L., Bergström L., Yan J. Adsorbents for the post-combustion capture of CO_2 using rapid temperature swing or vacuum swing adsorption // Appl. Energy. – 2013. – Vol. 104. – P. 418-433.

25 Bui M., Adjiman C.S., Bardow A., Anthony E.J., Boston A., Brown S., Fennell P.S. Carbon capture and storage (CCS): the way forward // Energy Environ. Sci. – 2018. – Vol. 11. – P. 1062.

26 Merkel T.C., Lin H., Wei X., Baker R. Power plant post-combustion carbon dioxide capture: An opportunity for membranes // Journal of Membrane Science. – 2010. – Vol. 359, Iss. 1-2. – P. 126-139.

27 Smit B. Carbon capture and storage: introductory lecture // Faraday Discuss. – 2016. – Vol. 192. – P. 9-25.

28 Karla M., Wrightb R.F., Berglena T.F., Denbya B. Worst case scenario study to assess the environmental impact of amine emissions from a CO_2 capture plant // Int J Greenhouse Gas Control. – 2011. – Vol. 5, Iss. 4. – P. 39-47.

29 D'Alessandro D.M., Smit B., Long J.R. Carbon Dioxide Capture: Prospects for New Materials // Angewandte Chemie International Edition. - 2010. - Vol. 49, Iss. 35. - P. 6058-6082.

30 Kanniche M., Gros-Bonnivard R., Jaud P., Valle-Marcos J., Amann J.-M., Bouallou C. Pre-combustion, post-combustion and oxy-combustion in thermal power plant for CO_2 capture // Applied Thermal Engineering. – 2010. – Vol. 30, Iss. 1. – P. 53-62.

31 Sjostrom S., Krutka H. Evaluation of solid sorbents as a retrofit technology for CO_2 capture // Fuel. – 2010. – Vol. 89, Iss. 6. – P. 1298-1306.

32 D'Alessandro D.M. Exploiting redox activity in metal-organic frameworks: concepts, trends and perspectives // Chemical Communications. – 2016. – Vol. 52, Iss. 58. – P. 8957-8971.

33 Martín C.F., Plaza M.G., Pis J.J., Rubiera F., Pevida C., Centeno T.A. On the limits of CO_2 capture capacity of carbons // Separation and Purification Technology. – 2010. – Vol. 74, Iss. 2. – P. 225-229.

34 Rouquerol F., Rouquerol J., Sing K.S.W., Llewelly N.P., Maurin G. Adsorption by Powders and Porous Solids Principles // Methodology and Applications, Second edition. – Amsterdam: Elsevier, 2014. – P. 646.

35 Oschatz M., Antonietti M. A search for selectivity to enable CO_2 capture with porous adsorbents // Energy Environ. Sci. – 2018. – Vol. 11. – P. 57.

36 Calvo-Muñoz E.M., García-Mateos F.J., Rosas J.M., Rodríguez-Mirasol J., Cordero T. Biomass Waste Carbon Materials as adsorbents for CO_2 Capture under Post-Combustion Conditions // Frontiers in Materials. – 2016. – Vol. 3. – Article 23.

37 Hoffman J.S., Pennline H.W. Study of regenerable sorbents for CO_2 capture // In Proceedings of First National Conference on Carbon Sequestration. – Washington, DC, 2001. – №. DOE/NETL-2001/1144.

38 Hayashi H., Taniuchi J., Furuyashiki N., Sugiyama S., Hirano S., Shigemoto N., Nonaka T. Efficient Recovery of Carbon Dioxide from Flue Gases of Coal-Fired Power Plants by Cyclic Fixed-Bed Operations over K_2CO_3-on-Carbon // Ind. Eng. Chem. Res. – 1998. – Vol. 37. – P. 185-191.

39 Hayashi H., Hirano S., Shigemoto N., Yamada S. Characterization of Potassium Carbonate Supported on Porous Materials and Application for the Recovery of Carbon Dioxide 10 from Flue Gases under Moist Conditions // Nippon Kagaku Kaishi. – 1995. – P. 1006-1012.

40 Hirano S., Shigemoto N., Yamada S., Hayashi H. Cyclic Fixed-Bed Operations over K_2CO_3-on-Carbon for the Recovery of Carbon Dioxide under Moist Conditions // Bull. Chem. Soc. Jpn. – 1995. – Vol. 68. – P. 1030-1035.

41 Liang Y., Harrison D.P., Gupta R.P., Green D.A., McMichael W.J. Carbon dioxide capture using dry sodium-based sorbents // Energy Fuels. – 2004. – Vol. 18. – P. 569-575.

42 Lee J.B., Ryu C.K., Baek J.I., Lee J.H., Eom T.H., Kim S.H. Sodium-based dry regenerable sorbent for carbon dioxide capture from power plant flue gas // Ind. Eng. Chem. Res. – 2008. – Vol. 47. – P. 4465-4472.

43 Seo Y., Jo S.H., Ryu C.K., Yi C.K. Effects of water vapor pretreatment time and reaction temperature on CO_2 capture characteristics of a sodium-based solid sorbent in a bubbling fluidized-bed reactor // Chemosphere. – 2007. – Vol. 69. – P. 712-718.

44 Yi C.K., Jo S.H., Seo Y., Lee J.B., Ryu C.K. Continuous operation of the potassium-based dry sorbent CO_2 capture process with two fluidized-bed reactors // Int. J. Greenhouse Gas Control. – 2007. – Vol. 1. – P. 31-36

45 Lee S.C., Kwon Y.M., Ryu C.Y., Chae H.J., Ragupathy D., Jung S.Y., Lee J.B., Ryu C.K., Kim J.C. Development of new alumina-modified sorbents for CO_2

sorption and regeneration at temperatures below 200 C // Fuel. – 2011. – Vol. 60. – P. 1465-1470.

46 Lee K.B., Beaver M.G., Caram H.S., Sircar S. Reversible Chemisorbents for Carbon Dioxide and Their Potential Applications // Industrial & Engineering Chemistry Research. – 2008. – Vol. 47, Iss. 21. – P. 8048-8062.

47 Ruthven D.M. Principles of Adsorption and Adsorption Processes. – New York: WileyInterscience, 1984. – P. 464.

48 Cazorla-Amorós D., Alcañiz-Monge J., de la Casa-Lillo M.A., Linares-Solano A. CO_2 As an Adsorptive To Characterize Carbon Molecular Sieves and Activated Carbons // Langmuir. – 1998. – Vol. 14, Iss. 16. – P. 4589-4596.

49 Wahby A., Ramos-Fernández J.M., Martínez-Escandell M., Sepúlveda-Escribano A., Silvestre-Albero J., Rodríguez-Reinoso F. High-Surface-Area Carbon Molecular Sieves for Selective CO_2 Adsorption // ChemSusChem. – 2010. – Vol. 3, Iss. 8. – P. 974-981.

50 Carr D.A., Lach-hab M., Yang S., Vaisman I.I., Blaisten-Barojas E. Machine learning approach for structure-based zeolite classification // Microporous and Mesoporous Materials. – 2009. – Vol. 117, Iss. 1-2. – P. 339-349.

51 Kelut P., Kulkarni K., Kulkarni A.D. CO_2 Adsorption By Various Catalysts // Chemical and Process Engineering Research. – 2014. – Vol. 18. – P. 7-15.

52 Hauchhum L., Mahanta P. Carbon dioxide adsorption on zeolites and activated carbon by pressure swing adsorption in a fixed bed // International Journal of Energy and Environmental Engineering. – 2014. – Vol. 5, Iss. 4. – P. 349-356.

53 Ko D., Siriwardane R., Biegler L.T. Optimization of a pressure-swing adsorption process using zeolite 13X for CO_2 sequestration // Ind. Eng. Chem. Res. – 2003. – P. 339-348.

54 Zhao Z., Cui X., Ma J., Li R. Adsorption of carbon dioxide on alkali-modified zeolite 13X adsorbents // Int. J. Greenh. Gas Control. – 2007. – Vol. 1 – P. 355-359.

55 Querejeta N., Plaza M., Rubiera F., Pevida C. Water Vapor Adsorption on Biomass Based Carbons under Post-Combustion CO_2 Capture Conditions: Effect of Post-Treatment // Materials. – 2016. – Vol. 9, Iss. 5. – P. 359.

56 Rogge S.M.J., Bavykina A., Hajek J., Garcia H., Olivos-Suarez A.I., Sepúlveda-Escribano A., Gascon J. Metal-organic and covalent organic frameworks as single-site catalysts // Chemical Society Reviews. – 2017. – Vol. 46, Iss. 11. – P. 3134-3184.

57 Stock N., Biswas Sh. Synthesis of Metal-Organic Frameworks (MOFs): Routes to Various MOF Topologies, Morphologies, and Composites // Chem. Rev. – 2012. – Vol. 112. – P. 933-969.

58 Devic T., Serre C. High valence 3p and transition metal based MOFs // Chem. Soc. Rev. – 2014. – Vol. 43, Iss. 16. – P. 6097-6115.

59 Evans J.D., Garai B., Reinsch H., Li W., Dissegna S., Bon V., Senkovska I., Fischer R.A., Kaskel S., Janiak C., Stock N., Volkmer D. Metal-organic frameworks in Germany: From synthesis to function // Coord. Chem. Rev. – 2019. – Vol. 380. – P. 378-418.

60 Sumida K., Rogow D.L., Mason J.A., McDonald T.M., Bloch E.D., Herm Z.R., Bae T.-H., Long J.R. Carbon Dioxide Capture in Metal-Organic Frameworks // Chem. Rev. – 2012. – Vol. 112. – P. 724-781.

61 Wang J., Huang L., Yang R., Zhang Z., Wu J., Gao Y., Zhong Z. Recent advances in solid sorbents for CO_2 capture and new development trends // Energy Environ. Sci. – 2014. – Vol. 7, Iss. 11. – P. 3478-3518.

62 Creamer A.E., Gao B. Carbon-Based Adsorbents for Postcombustion CO_2 Capture: A Critical Review // Environmental Science & Technology. – 2016. – Vol. 50, Iss. 14. – P. 7276-7289.

63 Plaza M.G., García S., Rubiera F., Pis J.J., Pevida C. Post-combustion CO_2 capture with a commercial activated carbon: Comparison of different regeneration strategies // Chemical Engineering Journal. – 2010. – Vol. 163, Iss. 1-2. – P. 41-47.

64 García S., Gil M.V., Martín C.F., Pis J.J., Rubiera F., Pevida C. Breakthrough adsorption study of a commercial activated carbon for pre-combustion CO_2 capture // Chemical Engineering Journal. – 2011. – Vol. 171, Iss. 2. – P. 549-556.

65 Hao W., Björkman E., Lilliestråle M., Hedin N. Activated carbons prepared from hydrothermally carbonized waste biomass used as adsorbents for CO_2 // Applied Energy. – 2013. – Vol. 112. – P. 526-532.

66 Ebrahimi F. Nanocomposites: New Trends and Developments. – InTech, Croatia, 2012. – p. 516

67 Camargo P.H.C., Satyanarayana K.G., Wypych F. Nanocomposites: Synthesis, Structure, Properties and New Application Opportunities // Materials Research. – 2009. – Vol. 12, №1. – P. 1-39.

68 High-Performance Composites Sourcebook / под ред. – Cincinnati, OH: Gardner Publications Inc., 2009. – P. 5-206

69 Mazumdar S.K. Composites Manufacturing: Materials, Product, and Process Engineering. – Boca Raton, FL: CRC Press, 2002. – p. 392

70 Palmer J., Savage L., Ghita O. R., Evans K. E. Sheet moulding compound (SMC) from carbon fibre recyclate // Composites Part A: Applied Science and Manufacturing. – 2010. – Vol. 41, №9. – P. 1232-1237.

71 Ajayan P.M., Schadler L.S., Braun P.V. Nanocomposite Science and Technology. – Weinheim: WILEY-VCH Verlag GmbH Co. KGaA, 2003. – P. 230.

72 Kamigaito O. What can be improved by nanometer composites? // Journal of the Japan Society of Powder and Powder Metallurgy. – 1991. – Vol. 38, Iss. 3. – P. 315-321.

73 Singh B., Chauhan S., Verma G. Nanocomposites–a review //J Chem Cheml. – 2015. – Т. 5. – №. September. – С. 506-510.

74 Cammarata R. Introduction to Nano Scale Science and Technology. – Midtown Manhattan, New York City: Springer Publishers, 2006. – p. 611.

75 Okpala C.C. Nanocomposites – An Overview // International Journal of Engineering Research and Development. – 2013. – Vol. 8, Iss. 11. – P. 17-23.

76 Композиты и нанокомпозиты // https://en.ppt-online.org/340177.

77 Senthil Kumar P., Gunasundari E. Nanocomposites: Recent Trends and Engineering Applications // Nano Hybrids and Composites. – 2018. – Vol. 20. – P. 65-80.

78 Mechanical properties of poly (lactic acid) (pla)/clay nanocomposite // http://umpir.ump.edu.my/id/eprint/3234/1/CD5698_MOHD_SHAIFOL_HAMID.pdf.

79 Ganguly S., Bhawal P., Ravindren R., Das N.C. Polymer Nanocomposites for Electromagnetic Interference Shielding: A Review // Journal of Nanoscience and Nanotechnology. – 2018. – Vol. 18, Iss. 11. – P. 7641-7669.

80 Johal M. S., Johnson L. E. Understanding nanomaterials. – Boca Raton, FL, USA: CRC Press, 2011. – C. 195-196.

81 Gaurav L., Henslee A.M., Farshid B., Parmar P., Lin L., Qin Y.X., Kasper F.K., Mikos A.G., Sitharaman B. Tungsten disulfide nanotubes reinforced biodegradable polymers for bone tissue engineering // Acta Biomaterialia. – 2013. – Vol. 9, Iss. 9. – P. 8365-8373.

82 Carrow J.K., Gaharwar A.K. Bioinspired Polymeric Nanocomposites for Regenerative Medicine // Macromolecular Chemistry and Physics. – 2014. – Vol. 216, Iss. 3. – P. 248-264.

83 Gaharwar A.K., Peppas N.A., Khademhosseini A. Nanocomposite hydrogels for biomedical applications // Biotechnology and Bioengineering. – 2013. – Vol. 111, Iss. 3. – P. 441-453.

84 Zhang S., Sun D., Fu Y., Du H. Recent advances of superhard nanocomposite coatings: a review // Surface and Coatings Technology. – 2003. – Vol. 167, Iss. 2-3. – P. 113-119.

85 Birkholz M., Albers U., Jung T. Nanocomposite layers of ceramic oxides and metals prepared by reactive gas-flow sputtering // Surface and Coatings Technology. – 2004. – Vol. 179, Iss. 2-3. – P. 279-285.

86 Boccaccini A.R., Kaya C., Shaffer M.S.P. Electrophoretic Deposition of Carbon Nanotubes (CNTs) and CNT/Nanoparticle Composites // Electrophoretic Deposition of Nanomaterials. – 2011. – P. 157-179.

87 Casati R., Vedani, M. Metal Matrix Composites Reinforced by Nano-Particles - A Review // Metals. – 2014. – Vol. 4, Iss. 1. – P. 65-83.

88 Xiang Z., Hu Z., Cao D., Yang W., Lu J., Han B., Wang W. Metal-Organic Frameworks with Incorporated Carbon Nanotubes: Improving Carbon Dioxide and Methane Storage Capacities by Lithium Doping // Angewandte Chemie International Edition. – 2010. – Vol. 50, Iss. 2. – P. 491-494.

89 Alhwaige A.A., Ishida H., Qutubuddin S. Carbon Aerogels with Excellent CO_2 Adsorption Capacity Synthesized from Clay-Reinforced Biobased Chitosan-Polybenzoxazine Nanocomposites // ACS Sustainable Chemistry & Engineering. – 2016. – Vol. 4, Iss. 3. – P. 1286-1295.

90 Chowdhury S., Parshetti G.K., Balasubramanian R. Post-combustion CO_2 capture using mesoporous TiO_2/graphene oxide nanocomposites // Chemical Engineering Journal. – 2015. – Vol. 263. – P. 374-384.

91 An H., Feng B., Su S. CO$_2$ capture capacities of activated carbon fibre-phenolic resin composites // Carbon. – 2009. – Vol. 47, Iss. 10. – P. 2396-2405.

92 Bhagiyalakshmi M., Hemalatha P., Palanichamy M., Jang H.T. Adsorption, regeneration and interaction of CO$_2$ with a polythiophene-carbon mesocomposite // Colloids and Surfaces A: Physicochemical and Engineering Aspects. – 2011. – Vol. 374, Iss. 1-3. – P. 48-53.

93 Wang Q., Luo J., Zhong Z., Borgna A. CO$_2$ capture by solid adsorbents and their applications: current status and new trends // Energy Environ. Sci. – 2011. – Vol. 4, Iss. 1. – P. 42-55.

94 Gargiulo V., Alfè M., Ammendola P., Raganati F., Chirone R. CO$_2$ sorption on surface-modified carbonaceous support: Probing the influence of the carbon black microporosity and surface polarity // Applied Surface Science. – 2016. – Vol. 360. – P. 329-337.

95 Aguilera-Herrador E., Lucena R., Cárdenas S., Valcárcel M. The roles of ionic liquids in sorptive microextraction techniques // TrAC Trends in Analytical Chemistry. – 2010. – Vol. 29, Iss. 7. – P. 602-616.

96 Blanchard L.A., Hancu D., Beckman E.J., Brennecke J.F. Green processing using ionic liquids and CO$_2$ // Nature. – 1999. – Vol. 399, Iss. 6731. – P. 28-29.

97 Hao G.-P., Li W.-C., Qian D., Lu A.-H. Rapid Synthesis of Nitrogen-Doped Porous Carbon Monolith for CO$_2$ Capture // Advanced Materials. – 2010. – Vol. 22, Iss. 7. – P. 853-857.

98 Meng L. Y., Park S. J. Effect of exfoliation temperature on carbon dioxide capture of graphene nanoplates //Journal of colloid and interface science. – 2012. – Т. 386. – №. 1. – С. 285-290.

99 Mishra A. K., Ramaprabhu S. Palladium nanoparticles decorated graphite nanoplatelets for room temperature carbon dioxide adsorption //Chemical Engineering Journal. – 2012. – Т. 187. – С. 10-15.

100 Yang S. et al. Graphene-based porous silica sheets impregnated with polyethyleneimine for superior CO2 capture //Advanced Materials. – 2013. – Т. 25. – №. 15. – С. 2130-2134.

101 Alhwaige A. A. et al. Biobased chitosan hybrid aerogels with superior adsorption: Role of graphene oxide in CO 2 capture //RSC advances. – 2013. – Т. 3. – №. 36. – С. 16011-16020.

102 Saleh M. et al. Synthesis of N-doped microporous carbon via chemical activation of polyindole-modified graphene oxide sheets for selective carbon dioxide adsorption //Nanotechnology. – 2013. – Т. 24. – №. 25. – С. 255702.

103 Zhou D. et al. Graphene-manganese oxide hybrid porous material and its application in carbon dioxide adsorption //Chinese science bulletin. – 2012. – Т. 57. – №. 23. – С. 3059-3064.

104 Hong S. M., Kim S. H., Lee K. B. Adsorption of carbon dioxide on 3-aminopropyl-triethoxysilane modified graphite oxide //Energy & Fuels. – 2013. – Т. 27. – №. 6. – С. 3358-3363.

105 Asai M. et al. Marked adsorption irreversibility of graphitic nanoribbons for CO2 and H2O //Journal of the American Chemical Society. – 2011. – T. 133. – №. 38. – C. 14880-14883.

106 She L., Li J., Wan Y., Yao X., Tu B., Zhao D. Synthesis of ordered mesoporous MgO/carbon composites by a one-pot assembly of amphiphilic triblock copolymers // J. Mater. Chem. – 2011. – Vol. 21, №3. – P. 795-800.

107 Sevilla M., Valle-Vigón P., Fuertes A. B. N-Doped Polypyrrole-Based Porous Carbons for CO_2 Capture // Advanced Functional Materials. – 2011. – Vol. 21, Iss. 14. – P. 2781-2787.

108 Wei J., Zhou D., Sun Z., Deng Y., Xia Y., Zhao D. A Controllable Synthesis of Rich Nitrogen-Doped Ordered Mesoporous Carbon for CO_2 Capture and Supercapacitors // Advanced Functional Materials. – 2012. – Vol. 23, Iss. 18. – P. 2322-2328.

109 Ye Qing, Jiang J., Wang C., Liu Y., Pan H., Shi Y. Adsorption of Low-Concentration Carbon Dioxide on Amine-Modified Carbon Nanotubes at Ambient Temperature // Energy & Fuels. – 2012. – Vol. 26, Iss. 4. – P. 2497-2504.

110 Nie Y., Wang W.-N., Jiang Y., Fortner J., Biswas P. Crumpled reduced graphene oxide–amine–titanium dioxide nanocomposites for simultaneous carbon dioxide adsorption and photoreduction // Catalysis Science & Technology. – 2016. – Vol. 6, Iss. 16. – P. 6187-6196.

111 Cascarini de Torre L.E., Fertitta A.E., Flores E.S., Llanos J.L., Bottani E.J. Characterization of shungite by physical adsorption of gases // J. Argent. Chem. Soc. – 2004. – Vol. 92, Iss. 4-6. – P. 51-58.

112 Тауасаров Е.К., Бержанова Р.Ж., Жумагалиева А.Н., Досжанов Е.О., Бодыков Д., Мансуров З.А. Очистка сточной воды при использовании природного минерала «Таурит» // Вестник КазНИТУ. – 2016. – №4. – С. 31-35.

113 Rozhkova N.N., Yemel'yanova G.I., Gorlenko L.E., Gribanov A.V., Lunin V.V. From stable aqueous dispersion of carbon nanoparticles to the clusters of metastable Shungite carbon // Glass Physics and Chemistry. – 2011. – Vol. 37, Iss. 6. – P. 613-618.

114 Deng S., Wei H., Chen T., Wang B., Huang J., Yu G. Superior CO_2 adsorption on pine nut shell-derived activated carbons and the effective micropores at different temperatures // Chem. Eng. J. – 2014. – Vol. 253. – P. 46-54.

115 Gargiulo V., Gomis-Berenguer A., Giudicianni P., Ania C.O., Ragucci R., Alfè M. Assessing the potential of bio-chars prepared by steam assisted slow pyrolysis for CO_2 adsorption and separation // Energy & Fuels. – 2018. – Vol. 32. – P. 10218-10227.

116 Creamer A.E., Gao B., Zhang M. Carbon dioxide capture using biochar produced from sugarcane bagasse and hickory wood // Chem. Eng. J. – 2014. – Vol. 249. – P. 174-179.

117 Madzaki H., Ghani W.A., Rebitanim N.Z., Alias A.B. Carbon Dioxide Adsorption on Sawdust Biochar // Procedia Engineer. – 2016. – Vol. 148. – P. 718-725.

118 Plaza M.G., González A.S., Pis J.J., Rubiera F., Pevida C. Production of microporous biochars by single-step oxidation: Effect of activation conditions on CO_2 capture // Appl. Energ. – 2014. – Vol. 114. – P. 551-562.

119 Heo Y-J., Park S-J. A role of steam activation on CO_2 capture and separation of narrow microporous carbons produced from cellulose fibers // Energy. – 2015. – Vol. 91. – P. 142-150.

120 Heidari A., Younesi H., Rashidi A., Ghoreyshi A.A. Adsorptive removal of CO_2 on highly microporous activated carbons prepared from Eucalyptus camaldulensis wood: Effect of chemical activation // Chem. Eng. J. – 2014. – Vol. 254. – P. 503-513.

121 Wei H., Deng S., Hu B., Chen Z., Wang B., Huang J., Yu G. Granular Bamboo-Derived Activated Carbon for High CO_2 Adsorption: The Dominant Role of Narrow Micropores // ChemSusChem. – 2012. – Vol. 5. – P. 2354-2360.

122 Ello A.S., de Souza L.K.C., Trokourey A., Jaroniec M. Coconut shell-based microporous carbons for CO_2 capture // Micropor. Mesopor. Mat. – 2013. – Vol. 180. – P. 280-283.

123 Zhang C., Song W., Ma Q., Xie L., Zhang X., Guo H. Enhancement of CO_2 Capture on Biomass-Based Carbon from Black Locust by KOH Activation and Ammonia Modification // Energy & Fuels. – 2016. – Vol. 30, Iss. 5. – P. 4181-4190.

124 Boonpoke A, Chiarakorn S, Laosiripojana N, Towprayoon S, Chidthaisong A. Synthesis of activated carbon and MCM-41 from bagasse and rice husk and their carbon dioxide adsorption capacity // J Sustain Energy Environ. – 2011. – Vol. 2. – P. 77-81.

125 Li D., Ma T., Zhang R., Tian Y., Qiao Y. Preparation of porous carbons with high low-pressure CO_2 uptake by KOH activation of rice husk char // Fuel. – 2015. – Vol. 139. – P. 68-70.

126 Khalili S., Khoshandam B., Jahanshahi M. Synthesis of activated carbon/polyaniline nanocomposites for enhanced CO_2 adsorption // RSC Advances. – 2016. – Vol. 6, Iss. 42. – P. 35692-35704.

127 Nowrouzi M., Younesi H., Bahramifar N. Superior CO_2 capture performance on biomass-derived carbon/metal oxides nanocomposites from Persian ironwood by H_3PO_4 activation // Fuel. – 2018. – Vol. 223. – P. 99-114.

128 Wasilewski P., Günther K. Lodestone: Nature's only permanent magnet - What it is and how it gets charged // Geophysical Research Letters. – 1999. – Vol. 26, Iss. 15. – P. 75-78.

129 Mishra A.K., Ramaprabhu S. Nano magnetite decorated multiwalled carbon nanotubes: a robust nanomaterial for enhanced carbon dioxide adsorption // Energy Environ. Sci. – 2011. – Vol. 4. Iss. 3. – P. 889-895.

130 Mishra A.K., Ramaprabhu S. Enhanced CO_2 capture in Fe_3O_4-graphene nanocomposite by physicochemical adsorption // Journal of Applied Physics. – 2014. – Vol. 116, Iss. 6. – P. 064306.

131 Alfe M., Ammendola P., Gargiulo V., Raganati F., Chirone R. Magnetite loaded carbon fine particles as low-cost CO_2 adsorbent in a sound assisted fluidized bed // Proceedings of the Combustion Institute. – 2015. – Vol. 35, Iss. 3. – P. 2801-2809.

132 Raganati F., Alfe M., Gargiulo V., Chirone R., Ammendola P. Isotherms and thermodynamics of CO_2 adsorption on a novel carbon-magnetite composite sorbent // Chemical Engineering Research and Design. – 2018. – Vol. 134. – P. 540-552.

133 Mansaray K.G., Ghaly A.E. Physical and Thermochemical Properties of Rice Husk // Energy Sources. – 2007. – Vol. 19, Iss. 9. – P. 989-1004.

134 Abikenova S., Rau A., Kalybekova E. Research of the rice productivity on saline lands of rice systems in Kazakhstan Republic //Life Sci J. – 2014. – Т. 11. – №. 11. – С. 356-361.

135 Zhumagaliyeva A., Jumabayev M., Gargiulo V., Ammendola P., Raganati F., Doszhanov Ye., Alfe M., Mansurov Z. Modified Carbonized Rice Husk as Low-Cost CO_2 Adsorbent: Perspectives and Possible Improvements // 2016 International Conference on Applied Mechanics, Mechanical and Materials Engineering. – Xiamen, China, 2016. – P. 572-575.

136 Zhumagaliyeva A., Gargiulo V., Raganati F., Doszhanov Ye., Alfè M. Carbon based nanocomposite material for CO_2 capture technology // Горение и плазмохимия. – 2019. – Т. 17, №. 1 – С. 9-13.

137 Zhumagaliyeva A., Gargiulo V., Ammendolo P., Raganati F., Luciani G., Chirone R., Doszhanov Ye., Alfe M. Magnetite loaded on carbonized rice husk: low cost biomass-derived composites for CO_2 capture // Proceeding of XXXIX Meeting of the Italian Section of the Combustion Institute. – Naples, 2016. – P. 12.

138 Zhumagaliyeva A., Gargiulo V., Raganati F., Mansurov Z., Doszhanov Ye., Alfè M. Sorption capacity of materials based on carbonized rice husk and carbon black for used as low cost adsorbent for CO_2 capture // Proceeding of the Joint IX International Symposium «Physics and Chemistry of Carbon Materials/Nanoengineering» and International Conference «Nanoenergetic Materials and Nanoenergetics», Almaty, 13-15 September. – Almaty, 2016. – P. 51-55.

139 Utkan G. (Guven), Sayar F., Batat P., Ide S., Kriechbaum M., Piskin E. Synthesis and characterization of nanomagnetite particles and their polymer coated forms // Journal of Colloid and Interface Science. – 2011. – Vol. 353, №2. – P. 372-379.

140 Zhumagaliyeva A., Gargiulo V., Doszhanov Ye., Alfe M. Testing composite material based on nano-particulate magnetite and carbonized rice husk for CO_2 sorption // Proceeding X International Symposium «The Physics and Chemistry of Carbon and Nanoenergetic Materials». – Almaty, 2018. – P. 168-170.

141 Senneca O. et al. Slow pyrolysis of walnut shells in nitrogen and carbon dioxide //Fuel. – 2018. – Т. 225. – С. 419-425..

142 Pandey R.K., Shukla S.S., Vyas A., Jain V., Jain P., Saraf S. Fingerprinting Analysis and Quality Control Methods of Herbal Medicines. – New York: CRC Press, Taylor and Francis Group, 2018. – P. 202.

143 Najera M. et al. Carbon capture and utilization via chemical looping dry reforming //Chemical Engineering Research and Design. – 2011. – Т. 89. – №. 9. – С. 1533-1543..

144	He M. et al. Advanced functional materials in solid phase extraction for ICP-MS determination of trace elements and their species-a review //Analytica Chimica Acta. – 2017. – Т. 973. – С. 1-24.

145	Sing K.S. Adsorption methods for the characterization of porous materials // Advances in Colloid and Interface Science. – 1998. – Vol. 76-77. – P. 3-11.

146	Shao X. et al. Adsorption of CO2, CH4, CO2/N2 and CO2/CH4 in novel activated carbon beads: Preparation, measurements and simulation //AIChE Journal. – 2011. – Т. 57. – №. 11. – С. 3042-3051.

147	Wei Q., Huang F., Cai Y. Textile surface characterization methods // Surface Modification of Textiles. – 2009. – № 97. – P. 26-57.

148	Ammendola P., Raganati F., Chirone R., Miccio F. Preliminary Assessment of Tuff as CO_2 Sorbent // Energy Procedia. – 2017. – Vol. 114. – P. 46-52.

149	Максутова К., Алибеков А., Жумагалиева А., Досжанов Е., Альфе М., Гарджюло В. Получение углеродных сорбентов на основе рисовой шелухи для улавливания диоксида углерода // Вестник КазНИТУ. – 2017. – №3. – С. 629-633.

150	Soltani N., Bahrami A., Pech-Canul M.I., González L.A. Review on the physicochemical treatments of rice husk for production of advanced materials // Chemical Engineering Journal. – 2015. – Vol. 264. – P. 899-935.

151	Junmeng Cai, Yifeng He, Xi Yu, Scott W. Banks, Yang Yang, Xingguang Zhang, Yang Yu, Ronghou Liu, Anthony V. Bridgwater. Review of physicochemical properties and analytical characterization of lignocellulosic biomass // Renewable and Sustainable Energy Reviews. – 2017. –Vol. 76. – P. 309-322.

152	Zhumagaliyeva A., Gargiulo V., Doszhanov Ye., Alfè M. Nanocomposite material like advanced sorbent materials for carbon dioxide capture // Горение и плазмохимия. – 2018. – Т 16, № 1. – С. 3-7.

153	Ismagilov Z.R., Shikina N.V., Andrievskaya I.P., Rudina N.A., Mansurov Z.A., Burkitbaev M.M., Biisenbaev M.A., Kurmanbekov A.A. Preparation of carbonized rice husk monoliths and modification of the porous structure by SiO_2 leaching // Catalysis Today. – 2009. – Vol. 147S. – P. S58-S65.

154	Maksutova K., Alibekov A., Zhumagaliyeva A. Alkali-treated carbonized rice husk adsorbent for capture and storage CO_2: developing of sorbents // Proceeding of The II Conference of the students and young scientists "Chemical physics and nanomaterials". – Almaty, 2017. – P. 37.

155	Thommes M., Kaneko K., Neimark A. V., Olivier J. P., Rodriguez-Reinoso F., Rouquerol J., Sing K.S.W. Physisorption of gases, with special reference to the evaluation of surface area and pore size distribution (IUPAC Technical Report) // Pure Appl. Chem. – 2015. – Vol. 87. – P. 1051-1069.

156	Arnal C., Alfè M., Gargiulo V., Ciajolo A., Alzueta, M.U., Millera, A., and Bilbao, R. Characterization of Soot // Chap 13 in Cleaner Combustion- Developing Detailed Chemical Kinetic Models / Eds. Battin-Leclerc F., Simmie J.M., Blurock E. – London: Springer, 2013. – P. 333-362.

157	Sankar S., Sharma S.K., Kaur N., Lee B., Kim D.Y., Lee S., Jung H. Biogenerated silica nanoparticles synthesized from sticky, red, and brown rice husk

ashes by a chemical method // Ceramics International. – 2016. – Vol. 42, № 4. – P. 4875-4885.

158 Li D., Teoh W.Y., Selomulya C., Woodward R.C., Munroe P., Amal R. Insightinto microstructural and magnetic properties of flame-made y-Fe_2O_3 nanoparticles // Journal of Materials Chemistry. – 2007. – Vol. 17. – P. 4876-4884.

159 Rui Han, Wei Li, Weiwei Pan, Minggang Zhu, Dong Zhou & Fa-shen Li. 1D Magnetic Materials of Fe3O4 and Fe with High Performance of Microwave Absorption Fabricated by Electrospinning Method // Scientific Reports. – 2004. – Vol. 4. – P. 7493.

160 Cristina Blanco-Andujar, Daniel Ortega, Quentin A. Pankhurst and Nguyen Thi Kim Thanh J. Elucidating the morphological and structural evolution of iron oxide nanoparticles formed by sodium carbonate in aqueous medium // Journal of Materials Chemistry. – 2012. – Vol. 22. – P. 12498-12506.

161 Gargiulo V., Zhumagaliyeva A., Ammendola P., Raganati F., Doszhanov Ye., Jumabayev M., Mansurov Z., Chirone R., Alfe M. From agricultural wastes to advanced sorbent materials for CO_2 capture: advantages and shortcomings of carbonized rice husk // Proceedings of Tenth Mediterranean Combustion Symposium. – Naples, Italy, 2017. – WIP12.

162 Zhumagaliyeva A., Tauassarov E. Low-cost CO_2 adsorbents for use in large point sources of pollution // Proceeding of The I Conference of the students and young scientists "Chemical physics and nanomaterials". – Almaty, 2016. – P. 40.

163 Gargiulo V., Alfè M., Raganati F., Zhumagaliyeva A., Doszhanov Y., Ammendola P., Chirone R. CO_2 Adsorption under Dynamic Conditions: An Overview on Rice Husk-Derived Sorbents and Other Materials // Combustion Science and Technology. – 2019. – Vol. 191(9). – P. 1484-1498.

APPENDIX A

ПАТЕНТ

ҚАЗАҚСТАН РЕСПУБЛИКАСЫ   РЕСПУБЛИКА КАЗАХСТАН

REPUBLIC OF KAZAKHSTAN

ПАТЕНТ
PATENT

№ 4302

ПАЙДАЛЫ МОДЕЛЬГЕ / НА ПОЛЕЗНУЮ МОДЕЛЬ / FOR UTILITY MODEL

(21) 2018/0775.2

(22) 26.10.2018

Қазақстан Республикасы Пайдалы модельдер мемлекеттік тізілімінде тіркеу күні / Дата регистрации в Государственном реестре полезных моделей Республики Казахстан / Date of the registration in the State Register of Utility Models of the Republic of Kazakhstan: 16.09.2019

(54) Күріш қауызы негізіндегі сорбентті алу тәсілі
Способ получения сорбента на основе рисовой шелухи
Method of producing sorbent based on rice husk

(73) Қазақстан Республикасы Білім және ғылым министрлігінің "әл-Фараби атындағы Қазақ ұлттық университеті" шаруашылық жүргізу құқығындағы республикалық мемлекеттік кәсіпорыны (KZ)
Республиканское государственное предприятие на праве хозяйственного ведения "Казахский национальный университет имени аль-Фараби" Министерства образования и науки Республики Казахстан (KZ)
"Al-Farabi Kazakh National University" Republican State Enterprise on the Right of Economic Management of the Ministry of Education and Science of the Republic of Kazakhstan (KZ)

(72) Жумагалиева Асем Нурбергеновна (KZ)   Zhumagaliyeva Assem Nurbergenovna (KZ)
Досжанов Ерлан Оспанович (KZ)   Doszhanov Yerlan Ospanovich (KZ)

Е. Оспанов
Y. Ospanov

«Ұлттық зияткерлік меншік институты» РМК директоры
Директор РГП «Национальный институт интеллектуальной собственности»
Director of the «National Institute of Intellectual Property» RSE

107

РЕСПУБЛИКА КАЗАХСТАН

(19) **KZ** (13) **U** (11) **4302**
(51) *C01B 32/00* (2017.01)
C02F 1/28 (2006.01)

МИНИСТЕРСТВО ЮСТИЦИИ РЕСПУБЛИКИ КАЗАХСТАН

ОПИСАНИЕ ПОЛЕЗНОЙ МОДЕЛИ
К ПАТЕНТУ

(54) **СПОСОБ ПОЛУЧЕНИЯ СОРБЕНТА НА ОСНОВЕ РИСОВОЙ ШЕЛУХИ**

(57) Полезная модель относится к способам получения композиционных сорбентов на основе остаточного растительного сырья, используемых для очистки смеси газов от диоксида углерода.

Техническим результатом является получение сорбента на основе карбонизованной рисовой шелухи для очистки диоксида углерода из смеси газов в статическом микрореакторе с сорбционной способностью до 33.59 мг CO_2/г.

Технический результат достигается способом получения углеродного сорбента с последующей обработкой УЗ и 28%-ным водным раствором NH_4OH, но в отличие от известного, в качестве исходного углеродного материала используют рисовую шелуху, а карбонизацию проводят при 400-500°С в течение 3 часов.

Полученный нами сорбент характеризуется содержанием углерода до 81,48%, обладает повышенной сорбцией CO_2 из смеси газов в статическом микрореакторе, время насыщения сорбента достигает 25 секунд.

Полезная модель относится к способам получения композиционных сорбентов на основе остаточного растительного сырья, используемых для очистки смеси газов от диоксида углерода.

Получаемый сорбент CRH-NH4OH на основе карбонизованной рисовой шелухи - это композитный материал для очистки диоксида углерода из смеси газов в статическом микрореакторе с сорбционной способностью 33,59 мгCO2/г.

Известны сорбенты (M. Alfe et al. Magnetite loaded carbon fine particles as low-cost CO2 adsorbent in a sound assisted fluidized bed / Proceedings of the Combustion Institute, 35 (2015), 2801-2809), полученные путем модификации углеродной сажи типа N110 с использованием магнетита. Углеродную сажу смешивали с водой, для однородности использовали ультразвуковую обработку (УЗ) в течение 20 минут, добавляли водный раствор FeCl3*6H2O и FeSO4*7H2O и 28% водный раствор NH4OH до достижении pH 10. Далее смешивали в течение 1 часа при температуре 80-90°C, фильтровали, промывали до достижении pH 7 и сушили в муфельной печи.

Основным недостатком данных сорбентов являются:

1. Низкая сорбционная способность сорбентов, достигает максимума в 16,5 мгCO2/г.

2. Использование дополнительных химических веществ, таких как хлорид железа и сульфат железа, вследствие чего время подготовки сорбента увеличивается вдвое.

3. Дополнительный расход на приобретение углеродной сажи типа N110.

Задачей полезной модели является разработка способа получения высокоэффективных сорбентов с повышенной сорбционной емкостью для сорбции диоксида углерода, являющегося вредным парниковым газом.

Достигаемый технический результат - получение композиционного сорбента на основе карбонизованной рисовой шелухи с сорбционной способностью до 33,59 мгCO2/г.

Сущность полезной модели:

1. Рисовую шелуху карбонизовали при температуре 400-500°C в течение 3 часов.

2. Смешивали с дистиллированной водой и для однородности обрабатывали УЗ в течение 20 минут.

3. Добавляли водный раствор NH4OH 28 %-ный до достижения pH 10.

4. На магнитной мешалке при нагревании 80-90°C перемешивали в течение 50-60 минут.

5. Фильтровали и промывали до достижении pH 7.

6. Сушили в муфельной печи.

Карбонизованная рисовая шелуха (CRH) показывает сорбционную способность до 22 мгCO2/г, в то время как проведенные опыты показывают, что сорбент CRH-NH4OH, полученный по заявляемому способу, действительно проявляет высокосорбционные свойства и может быть использован в технологии улавливания CO2.

Сорбционная способность CRH-NH4OH составляет 33,59 мгCO2/г.

Гидроксид аммония способствует уменьшению массы неорганических соединений в составе рисовой шелухи, что ведет к увеличению содержания углерода в сорбенте и способствует высокому улавливания CO2. Элементный анализ сорбента CRH-NH4OH показал увеличение содержание углерода до 81,48%, в то время как содержание неорганических соединений, преимущественно кремния уменьшилось на 9% (Фиг. 1).

Технические показатели полученного сорбента CRH-NH4OH.

Адсорбционная способность сорбента проверена на лабораторном статическом микрореакторе Pyrex microreactor (Фиг. 2).

В статическом микрореакторе смешивают два газа, CO2 1 и N2 2 со скоростью 15 нормолитров в час, с постоянной 3%-ной концентрацией диоксида углерода. Потоки газов, проходящие через контроллеры Bronkhorst 3 и 4, попадают через общий контроллер 5 в адсорбционную трубку диаметром 1 см и длинной 60 см. На подложку 6 устанавливают сорбент 0,5 г CRH-NH4OH. дисперсностью 180-400 микрон. Перед проверкой сорбентов аппарат микрореактора включают на 3 минуты для очистки и после завершения сорбционного процесса оставляют включенным в течение 50 с. Данные сорбционной способности попадают на инфракрасный газовый анализатор, преобразованные данные рассчитываются и предоставляются в качестве графика функции отношения изначальной концентрации диоксида углерода к исходящей и времени насыщения сорбента на подложке. График функции представлен в виде логарифмической шкалы, далее график преобразовали с помощью интеграции изначальной C0 и исходящей C концентраций с массой сорбента mads и временем насыщения сорбента на подложке. Кривая соотношения входящего потока газов и исходящего потока газов и времени насыщения подложки (до фактического равенства входящего и исходящего потока) изображена в логарифмическом масштабе и составила 21,26 мгCO2/г и 33,59 мгCO2/г для CRH и CRHI-NH4OH соответственно (Фиг. 3).

Пример 1 Рисовую шелуху карбонизуют в течение 3 часов при температуре 500°C. 1 г карбонизованной рисовой шелухи (CRH) смешивают с 200 мл дистиллированной воды, обрабатывают в ультразвуковой ванне в течение 20 минут при комнатной температуре с частотой 35 кГц. Добавляют 10 мл 28%-ного водного раствора NH4OH. Полученную суспензию смешивают на магнитной мешалке в течение 1 часа при температуре 90°C, промывают дистиллированной водой до достижения нейтрального pH. Фильтрацию проводят в системе вакуумной фильтрации с мембраной из нитрата целлюлозы с размером пор 2 мкм. Сушат в муфельной печи при 110°C. Полученный сорбент CRH-NH4OH тестируют на сорбционную способность в статическом

2

110

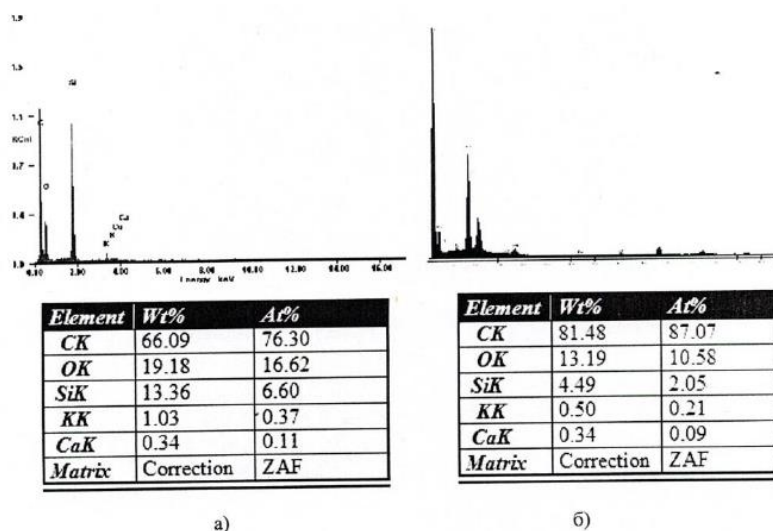микрореакторе, в таблице 1 представлены данные адсорбции CO_2 в зависимости от времени, преобразованные с Фиг. 3.

Таблица 1

Изменение сорбционной способности сорбента CRH-NH4OH в зависимости от его времени насыщения.

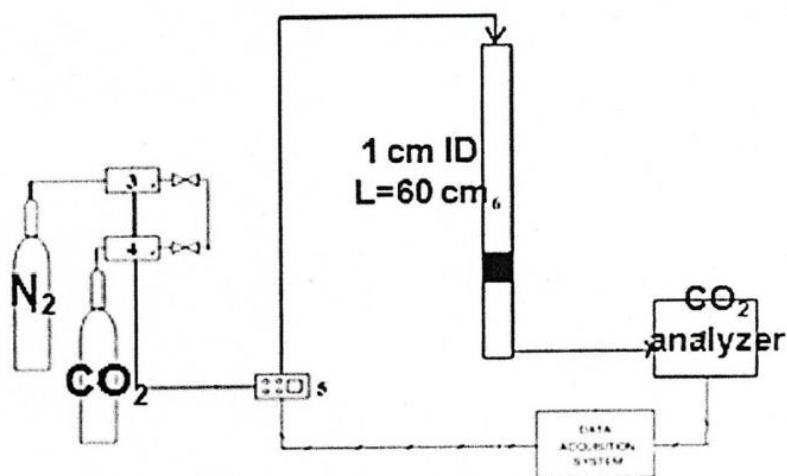| Время насыщения сорбента, сек	Сорбционная способность m_{ads} (мгCO$_2$/г)
3	26,05
8	28,81
10	31,26
19	32,44
25	33,59
27	2,84
34	2,42

Из вышеприведенной таблицы видно, что данным способом получения сорбента на основе рисовой шелухи достигнут желаемый технический результат, т.е. получен сорбент с высокой сорбционной способностью по диоксиду углерода. Максимальные значения сорбии для полученного сорбента составляют 33,59 мгCO$_2$/г. время насыщения сорбента 25 секунд.

ФОРМУЛА ПОЛЕЗНОЙ МОДЕЛИ

Способ получения сорбента на основе рисовой шелухи, включающий карбонизацию исходного материала с последующей обработкой УЗ и 28 %-ным водным раствором NH4OH, *отличающийся* тем, что в качестве исходного материала используют рисовую шелуху, а карбонизацию проводят при 400-500°С в течение 3 часов.

Element	Wt%	At%
CK	66.09	76.30
OK	19.18	16.62
SiK	13.36	6.60
KK	1.03	0.37
CaK	0.34	0.11
Matrix	Correction	ZAF

а)

Element	Wt%	At%
CK	81.48	87.07
OK	13.19	10.58
SiK	4.49	2.05
KK	0.50	0.21
CaK	0.34	0.09
Matrix	Correction	ZAF

б)

Фиг. 1 – Элементный состав сорбентов: а) CRH, б) CRH-NH4OH

3

Фиг. 2 – Статический микрореактор для определения сорбционной способности сорбентов
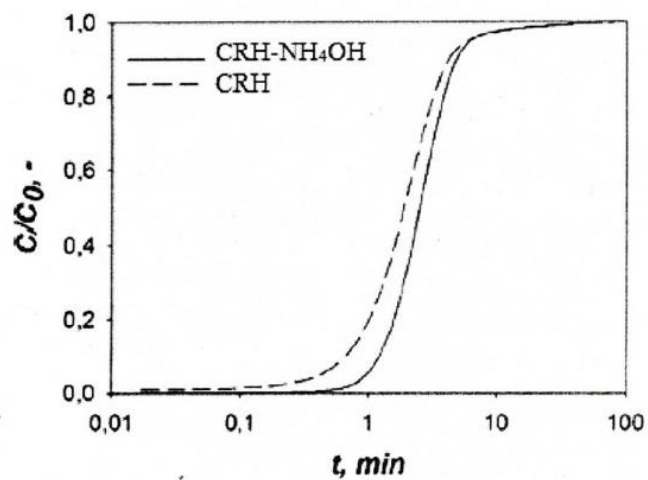
Фиг. 3 – График функции сорбционной способности сорбентов CRH и CRH-NH₄OH

4